University of Naples Federico II

Industrial Engineering Department

Doctoral Dissertation:

Performance Analysis of High Vacuum Flat Plate Collectors, methods and results

Tutor

Prof. Eng. Marilena Musto

Supervisor

Dr. Roberto Russo

Candidate:

Dr. Eliana Gaudino

XXXVI PhD Cycle

0. INTRODUCTION

Climate change is certainly one of the most pressing global challenges of our time, affecting the environment, human societies, and the overall well-being of future generations. As the world experiences rising temperatures, shifting weather patterns, and increasing extreme events, there is an urgent need to transition towards sustainable and clean energy sources [1]. The energy sector plays a crucial role in climate change mitigation and adaptation efforts. The burning of fossil fuels, such as coal, oil, and natural gas, for energy production, releases Green House Gases (GHGs) into the atmosphere, leading to the enhanced greenhouse effect and global warming [2] . To mitigate and control climate change, it is necessary to reduce GHG emissions by transitioning from fossil fuel-based energy systems to low-carbon alternatives. According to the International Energy Agency [3], industrial heat makes up two-thirds of industrial energy demand and almost one-fifth of global energy consumption. Since most of the industrial heat is produced by fossil fuel combustion, it creates a substantial stream of CO_2 emitted every year [4] . Decarbonizing the heat production field requires a significant shift in generating industrial heat, especially in the high and medium-temperature heating sectors [5].

Solar energy, as a clean and abundant source of power, is a viable solution to satisfy population energy needs and the urgent global challenge of climate change. While solar photovoltaic (PV) systems are widely recognized for their ability to convert sunlight directly into electricity [6], solar energy can also be harnessed to produce heat. The benefits of solar thermal energy extend beyond environmental considerations.

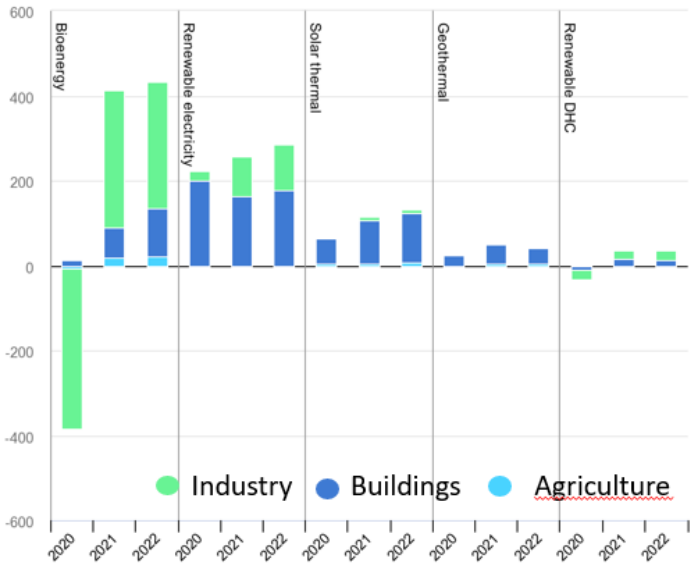

Figure 1 Annual heat consumption by source 2020-2022 [3]

Solar heating systems can provide energy independence and resilience, particularly in areas with limited access to conventional energy sources or vulnerable to disruptions in energy supply. Moreover, solar thermal technologies offer long-term cost savings, as they rely on free and abundant sunlight rather than expensive fossil fuels.

Solar collectors' technology is constantly evolving, enabling the spread of their use to an increasing number of utilizations [7]. The trend of the annual global change in renewable heat consumption by source in 2022 [3] shows that the more significant portion of the 150 PJ of extra energy produced by solar thermal technology in the former year was used to satisfy the building sector energy demand and just a small amount the industrial heat demand (Fig.1).

One of the most common applications of solar thermal technology is water heating [8]. Solar water heaters consist of flat-plate or evacuated tube collectors that absorb sunlight and transfer the captured heat to water, which is then stored in a tank for later use. Solar water heating systems have proven to be highly efficient, cost-effective, and environmentally friendly alternatives to conventional water heating methods that rely on fossil fuels [9].

In addition to water heating, solar thermal energy finds applications in space heating, where it can be used to warm indoor spaces in residential, commercial, and industrial buildings [10]. Solar thermal systems can also be integrated with existing heating systems, such as radiant floor heating [11] or forced air systems, to provide supplementary heat or meet a significant portion of the heating demand. Moreover, solar thermal energy has the potential to cater to a wide range of industrial processes that require heat, such as food processing, chemical production, and drying applications [12].

Within the industrial sector, process heat at the mid-temperature range of 100 °C ÷ 200 °C weighs 21% of the overall industrial demand for heating and cooling.

Solar thermal energy systems can be classified into three categories regarding operating temperature: Low-temperature systems (<150 °C) include Conventional Flat Plate Collectors, Evacuated Tube Collectors, and Compound Parabolic Collectors; Medium-temperature systems (from 150 to 400 °C) are Parabolic Trough Collectors, Linear Fresnel Collectors while as High-Temperature systems (>400 °C) can be classified Large Parabolic Trough Collectors and Linear Fresnel Collectors [13]. Flat Plate (FP) systems are the most fundamental and studied technology for solar-powered domestic hot water systems. The overall idea behind this technology is simple. They can collect diffuse and direct rays without solar tracking, being cheaper than concentrating collectors [14]. However, Conventional Flat Plates are mostly used in applications requiring temperatures lower than 100 °C since they experience high thermal losses caused by conduction, convection, and radiation. The conduction heat losses occur from the sides and the back of the collector plate, the convection heat losses take place from the absorber plate to the glazing cover, and the radiation losses occur from the absorber plate to the

envelop [15]. To minimize conduction loss, it should be used use materials with low thermal conductivity, whereas a drastic reduction of convective losses to a negligible value can be obtained by evacuating the space around the absorber plate [16].

In recent years, a novel architecture has emerged to overcome these limitations: a flat collector hosting an unconcentrated plate absorber operating under vacuum insulation that, in this thesis, will be indicated as High Vacuum Flat Plate Collector (HVFPC). This solution is more appealing than traditional evacuated tube collectors due to its reduced size, larger fill factor, wider acceptance angle for solar light, and lack of need for a tracking system. The concept was originally introduced by Eaton and Blum in 1975 [17], who applied a moderate vacuum pressure of 1 mbar to a flat plate collector. This approach significantly reduced thermal losses by suppressing internal convective motions, limiting heat transfer to residual gases through conduction only. By filling the envelope with Krypton at a pressure of 50 mbar, the efficiency reached an impressive 45% at an absorber temperature of 150 °C [18]. Moss et al. conducted tests on a small-scale prototype of a non-concentrated flat plate thermal collector, further reducing the internal pressure to below $5x10^{-3}$ mbar, thereby minimizing the thermal conduction of residual gases to a negligible level [19]. Their work demonstrated the potential to convert a larger quantity of solar energy annually compared to concentrated evacuated tubes, exceeding 60%, due to a wider acceptance angle that allows for the collection of more diffuse solar light and a higher fill factor of the overall area.

Furthermore, two companies, SRB Energy in 2005 [20] and TVP Solar in 2008 [21], proposed commercial flat panels operating under high-vacuum insulation, although only the latter is currently active. A recent study presents impressive results from a 50 m^2 installation of TVP Solar panels, obtained through four months of testing under normal operating conditions [22]. These panels achieved a global efficiency of 50% at an absorber temperature of 150 °C, surpassing other mid-temperature solar thermal collectors. This performance could potentially be improved with the use of a suitable absorber. The TVP Solar panels were equipped with Mirotherm® from Alanod [23], a selective solar thermal absorber designed for low-temperature applications. The choice of this absorber was necessitated by the absence of commercially available absorbers specifically designed for unconcentrated operation at mid-temperatures up to 200 °C. Moving from traditional non-evacuated to evacuated flat panels shifts the primary thermal loss mechanism from gas convection and conduction surrounding the absorber to the radiative emission from the absorber itself.

In recent years, our research group has focused on optimizing the Selective Solar Absorber (SSA), which is a critical component of HVFPCs. Recent advancements have led to the development of new optimized SSAs with low emissivity, accompanied by dedicated characterization procedures. Building upon previous research, this work aims to investigate the performance analysis of HVFPCs,

with a particular focus on energy forecasting and predictions alongside technological advancements in these collectors.

Chapter 1 provides an in-depth examination of HVFPCs and SSAs technology. The last section of the chapter introduces the experimental set-ups used for the fabrication and optical characterization of absorber coatings realized to investigate the possibility of improving HVFPCs efficiency.

Methods and results adopted by our research group to improve the efficiency of HVFPCs are presented in Chapter 2. The easiest strategy adopted involves the deposition of a thin silver film on the aluminum commercial SSA substrate, to minimize power emission from the back side of the absorber towards the panel bottom case. In the second section of the chapter, a novel optimization strategy with the description of SSA coatings realization optimized to work at 200 °C and 300 °C. The introduction of low-emissive substrates necessitates improved precision in emissivity measurements. The chapter also addresses adjustments on procedure for evaluation of thermal emittance of materials with extremely low emissivity levels and/or small sample dimensions.

Once the SSAs are optimized, there is a need for a model for energy forecasting and performance evaluation of HVFPCs equipped with the optimized absorbers. The formulation of an efficiency model specific to HVFPCs is presented, which is based on the optical properties of the selective absorber. This proposed model explicitly incorporates radiative heat exchange with the ambient environment, which is the primary source of thermal losses for evacuated collectors operating at high temperatures. Furthermore, it separates the radiative losses dependent on the optical properties of the absorber from other thermal losses attributed to the HVFPC architecture. The model's validity is demonstrated by applying it to an MT-Power HVFPC manufactured by TVP-Solar, and it successfully predicts the energy production of HVFPCs equipped with the newly optimized selective solar absorbers.

The specific temperature frequency function f(T) of the HVFPCs is derived in Chapter 3, taking into account their high thermal efficiency and maximum temperature that the collector can achieve (stagnation temperature). This is particularly significant since the current standard procedure for assessing the durability of solar absorber surfaces is only applicable to low-temperature applications such as domestic hot water production (DHW). In the same Chapter are detailed the experimental set-up (“Test-Bench”) and dynamic simulation model employed for f(T) evaluation, useful instruments for energy forecasts and HVFPCs performance analysis.

Lastly, Chapter 4 details the author's period of work at TVP-Solar company, involving performance measurements, dynamic simulation, and regulation of a HVFPCs solar field test facility installed at the Avellino company seat. The performance measurements serve as the foundation for conceiving a

new optimized regulation strategy, while the field test facility will be utilized to evaluate a new stratification tank object for future research endeavors.

1. TECHNOLOGY OF HIGH VACUUM FLAT PLATE COLLECTORS (HVPCS)

This chapter will give an overview of High Vacuum Flat Plate Collectors and their structural characteristics with a particular focus on the technology of selective solar absorbers describing also the specific characteristics required by SSAs adopted for HVFPCs.

1.1 VACUUM INSULATION

The concept of using vacuum insulation to improve the performance of solar collectors was first introduced in the mid-20th century it was recognized that the creation of vacuum between the absorber and the cover of a solar collector would result in a substantial improvement in collector efficiency due to reduction in heat loss through convection and conduction. At pressures lower than 10^4 Pa the conduction losses almost vanish [24] (continuum regime of gas heat conduction being independent of pressure [25]). Gases like argon, xenon, krypton, or sulfur hexafluoride could be introduced into the chamber: [25] demonstrated that they allow for lower conductivity compared to air, as shown in Fig. 1.1.

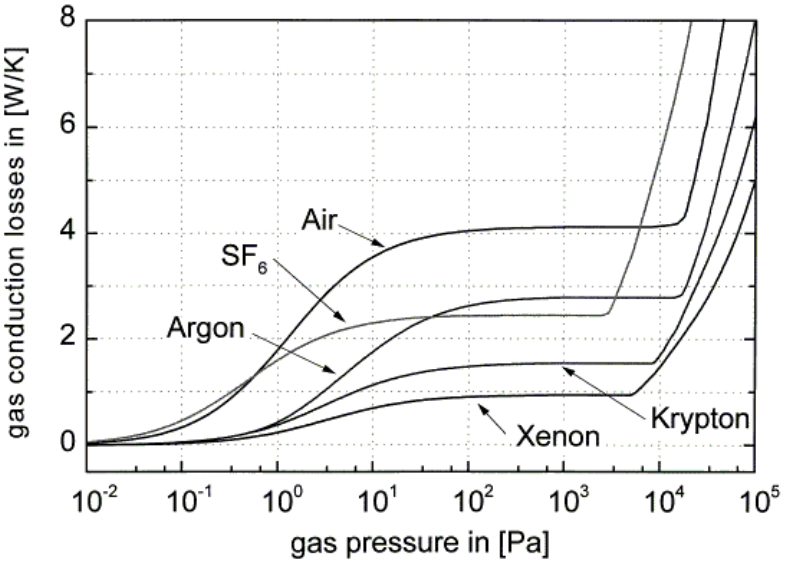

Figure 1.1 Heat losses by gas heat conduction from the hot absorber to the casing in a flat-plate collector in dependency on the gas pressure in the collector casing for different filling gases. The typical operation pressure ranges in the plateau between 100 and 10^4 Pa (adapted from [25]).

Lower conductivity means lower heat losses and the reduction of heat losses allows also for enhanced performance in cold and cloudy conditions the evacuated collector can maintain high operating temperatures, ensuring efficient heat transfer to the working fluid. Even in sub-zero temperatures,

vacuum collectors can still provide useful heat output, making them suitable for heating applications in northern latitudes or during winter months [26].

Vacuum insulation also offers improved durability compared to other collector designs. The vacuum acts as a barrier, preventing the entry of moisture, dust, and other contaminants that could potentially damage the absorber or reduce performance over time. This enhances the lifespan of the collector and reduces maintenance requirements.

The first idea of a vacuum solar thermal collector was proposed in 1909 by Emmett that presented several **evacuated-tube concepts** for solar energy collection, two of which are still sold commercially today [27].

1.1.1 Evacuated Tube Collectors

The introduction of evacuated tube collectors (ETCs) in the late 1970s aimed to address the significant thermal energy losses encountered by traditional flat plate collectors (FPCs) [28].

ETCs commonly consist of parallel rows of twin glass tubes, with each inner tube containing a metal heat pipe attached to an absorber fin (Figure 1.2) [29]. The absorber plate is either a metallic strip with a selective coating attached in the center of each tube or the pipe itself can be 'painted' with a solar coating.

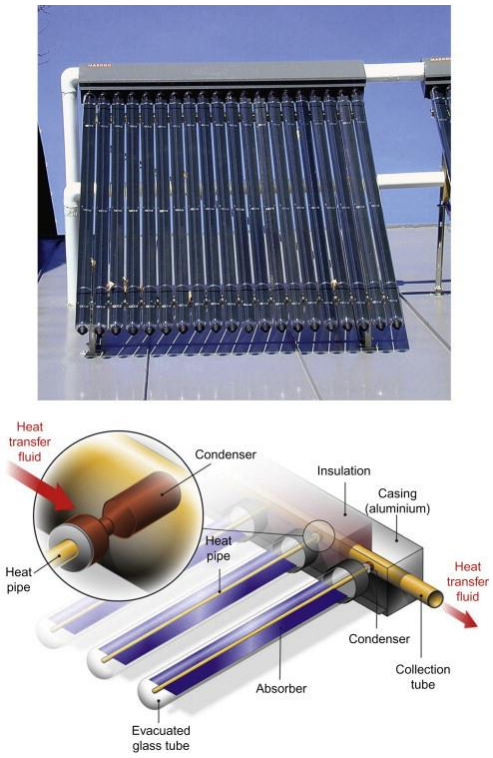

Figure 1.2 Picture (on top) and schematic representation (bottom) of a common type of evacuated-tubes collector [29]

Solar radiation heats the absorber plate, which in turn heats the evaporator section of the heat pipes and evaporates the entire working fluid. The generated vapor moves toward the condenser by natural convection, releasing its heat to operate thermal processes or for storage purposes. It is important to note that ETCs require a certain tilt angle to facilitate the return of the condensed internal fluid to the hot absorber. ETCs offer high heat extraction efficiency above 80°C due to the combined effects of a highly selective surface coating and vacuum insulation of the absorber element [30] (Figure 1.3).

Despite their advantageous performance in the middle-temperature range, ETCs exhibit several disadvantages compared to FPCs, primarily related to their structural characteristics. ETCs tend to be more expensive than traditional FPCs due to the manufacturing process and the materials used, such as high-quality glass tubes and selective coatings [31]. The weight of ETCs is typically higher due to the presence of glass tubes and additional components, necessitating stronger support structures and increasing installation complexity. The load-bearing capacity of the installation surface must be carefully considered to accommodate the weight of the collectors.

Proper connection and sealing of individual tubes in ETCs require skilled labor and precise installation techniques to prevent air leakage or reduced system performance. Additionally, the plumbing and mounting requirements for evacuated tube collectors add complexity and cost to the installation process. ETCs also demand frequent maintenance due to the relative fragility of the glass tubes and potential degradation of the vacuum seal and tube connections, which can lead to air or moisture infiltration [32].

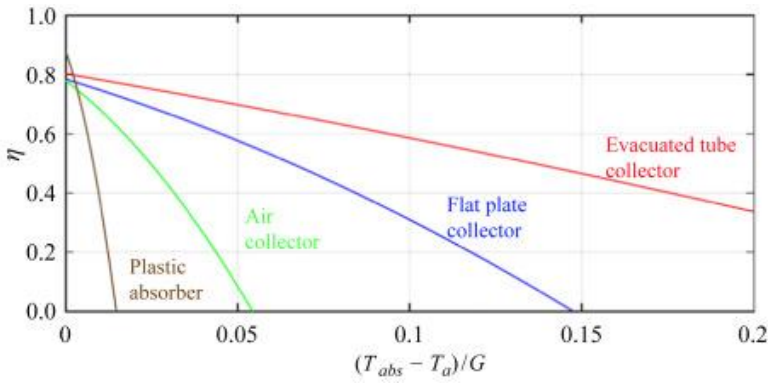

Figure 1.3 Efficiency curves of different types of solar collector as function of the ratio between absorber and ambient temperature difference ($T_{abs} – T_a$) and solar irradiation G [29].

While ETCs excel in cold and cloudy conditions, their efficiency may be reduced at very high temperatures. Exceeding a certain threshold, the heat buildup in the collector can impact the vacuum seal or cause tube expansion, potentially resulting in performance degradation.

Regarding solar capture, it is important to note that regions between individual tubes and gaps between tubes and their absorbers do not contribute to absorption. As per the ISO 9806 standard [33], efficiency must be measured in terms of the device's occupied area (gross area), favoring flat plate collectors. To combine the advantages of evacuated tube collectors and flat plate collectors, there has been growing interest in a new type of collector in recent years: **High Vacuum Flat Plate Collectors**.

1.1.2 High Vacuum Flat Plate Collectors

High Vacuum Flat Plate Collectors (HVFPCs) are a type of high-efficiency solar thermal device capable of meeting heat demand up to 200 °C.

They offer the advantage of a flat structure in addition to the benefits of vacuum insulation. HVFPCs consist of a flat absorber enclosed within a vacuum-sealed structure with a top glass cover.

Vacuum insulation in solar thermal systems was traditionally achieved using evacuated tube collectors (ETCs) due to the challenges associated with creating a vacuum seal in a flat plate design. However, the company TVP Solar has successfully overcome these technical issues and is now a leading producer of evacuated flat plate collectors [21].

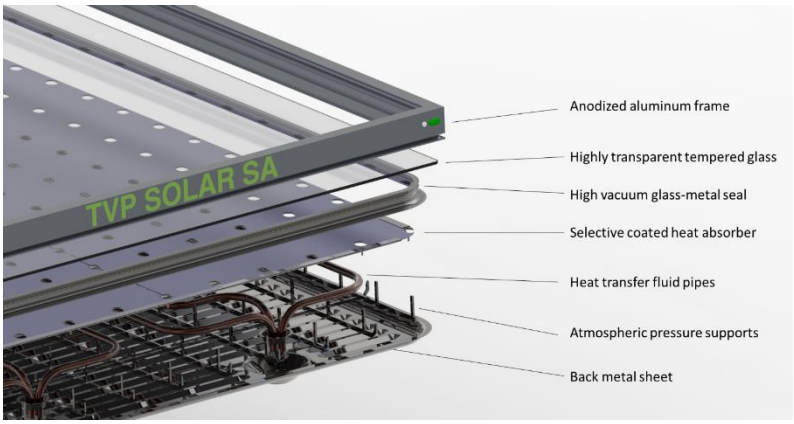

Figure 1.4 Schematic of TVP-Solar HVFPC MT-Power Structure

The design of their MT-Power HVFPCs involves a metallic vessel body closed by the front glass, and the vacuum seal is formed between the glass and a metallic surface [34]. The sealing process involves frit glass bonding, where a glass-based paste is melted at its bonding temperature while in contact with the glass and metal surface. The chemical affinity of the materials enables them to bond without the need for ultrasonic processes [35]. Key requirements for such vacuum seals include vacuum tightness, controlled degassing during operation and low soldering temperatures. Temperatures exceeding 250 °C can compromise the mechanical properties of tempered glass, leading to a weakening and potential implosion risk.

Another important aspect of evacuated flat plate collectors is the need for an active system to remove gases released into the vacuum environment over years of operation. TVP-Solar HVFPCs utilize a chemical getter pump located inside the collector, which is thermally activated at temperatures around 300 °C. This pump actively absorbs residual gases, ensuring a high vacuum level throughout the service life.

The supporting structure of HVFPCs plays a crucial role in enabling the envelope to withstand external ambient pressure. The glass support structure incorporates pins that bear the external glass pressure, creating a more robust structure. The front glass is bonded to the rest of the system using an adhesive paste. Consequently, the absorber has holes to accommodate the pins, leaving 97% of the absorber area available for heat absorption. The structure of TVP-Solar HVFPC MT-Power is depicted in Figure 1.4, with components including the anodized aluminum frame, highly transparent tempered glass, high vacuum glass-metal seal, selective coated heat absorber, heat transfer fluid pipes, atmospheric pressure supports (passing through holes in the absorber), and a back metal sheet. Despite the advantages of vacuum encapsulation, both optical and radiative losses still exist, as shown in Fig. 1.5. The radiative losses increase exponentially with the fourth power of the temperature, limiting the efficiency of the HVFPCs.

Therefore, the adoption of a Selective Solar Absorber (SSA) becomes necessary to ensure high absorptance in the solar irradiation spectrum (λ = 0.3-2.5 μm) and low emissivity in the infrared (IR) region (λ > 2.5 μm). These factors help minimize the drop in absorber efficiency at high temperatures [22], [36].

Further details about selective solar absorbers developed for HVFPCs will be provided in the subsequent section.

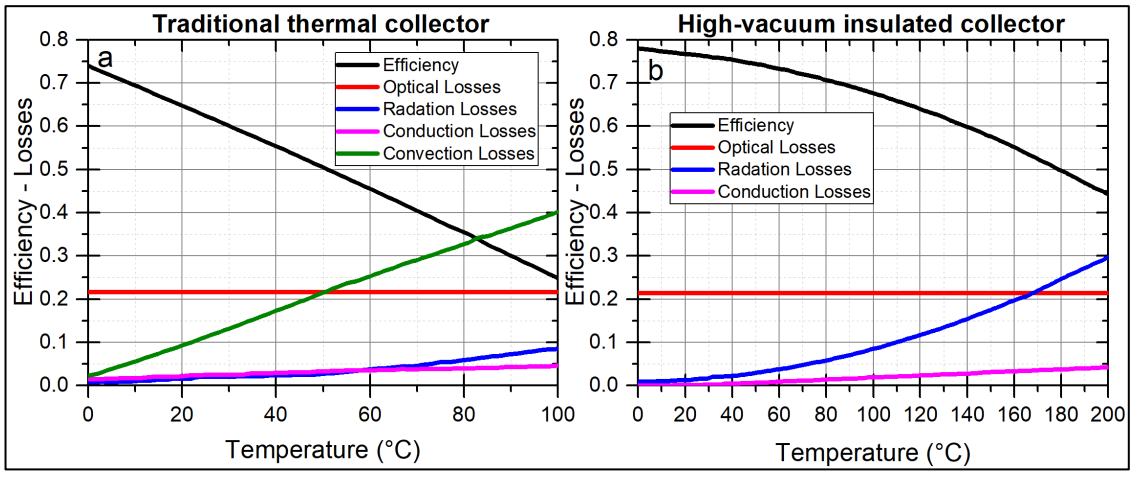

Figure 1.5 Effects of high vacuum insulation on the performance of a flat plate solar collector. (a) Efficiency and losses in a standard flat plate solar collector without vacuum insulation as function of the operating temperature. (b) Efficiency and losses of a high vacuum flat plate collector as function of the operating temperature.

1.2 SELECTIVE SOLAR ABSORBERS

For Flat Plate Solar Thermal Collectors, the Solar Absorber is certainly the key component because is the one that converts the solar irradiation into useful heat by transferring it to the HTF flowing in the pipes that are in thermal contact with the absorber.

The principal characteristic of solar absorbers, for this reason, is the high thermal conductivity [37] guaranteed using a few millimeter thicknesses of high-conductive materials such as copper or aluminum [38]. Besides high thermal conductivity, solar absorbers must have optical characteristics that allow for the maximum conversion of the solar irradiance impacting its surface. To understand what we mean by the optical behavior of a solar absorber, in the following subsection, hints of basic principles of optics will be reported.

1.2.1 Basic principles of optics

The principles of optics in the context of solar irradiation involve the behavior of light as it interacts with various materials and surfaces. Understanding these principles is crucial for designing efficient solar energy systems.

All bodies, including the Sun, radiate energy on the electromagnetic spectrum. As the temperature of a body increases, the wavelength of the radiation it emits shifts to lower values. The Sun's surface temperature is approximately 5,800 °C, and sunlight consists of a broad range of electromagnetic radiation, including infrared, visible, and ultraviolet light [39].

The diagram in Fig 1.6 shows the Sun emission spectrum, that is the energy emitted at each wavelength of radiation. The peak is in the visible spectrum [40]. When sunlight reaches the surface of a solar absorber, the amount of energy converted depends on how the surface interacts with the solar irradiation. Several phenomena can affect the incident light beam:

1. Reflection: When light encounters a surface, a portion of it can be reflected. The angle of incidence (the angle at which light strikes the surface) is equal to the angle of reflection (the angle at which the light is reflected). The reflectivity of a surface depends on its optical properties and can vary with different wavelengths of light.
2. Transmission: Light can pass through certain materials, resulting in transmission. Transparent or translucent materials allow light to transmit through them without significant absorption or reflection. The degree of transmission depends on the material's composition and thickness, as well as the wavelength of the light.
3. Absorption: When light interacts with a material, it can be absorbed, transferring its energy to the material. The extent of absorption depends on the material's properties and the wavelength

of the incident light. Absorption of solar radiation is desirable in solar energy systems, as it leads to the conversion of light energy into heat or electricity.

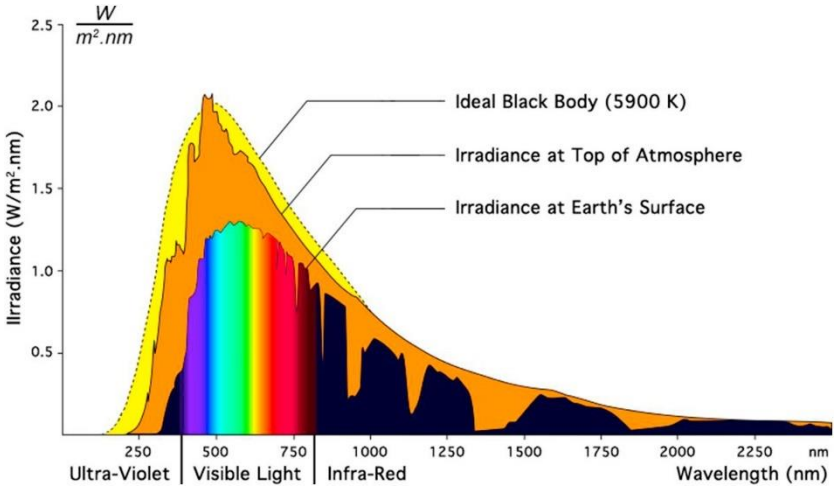

Figura 1.6 Theoretical black body spectrum and full solar spectrum at earth's surface and the top of atmosphere. [40]

These phenomena can be described by the coefficient of reflection (ρ_λ), absorption (α_λ), and transmission (τ_λ), for different wavelengths of light. These coefficients represent the fractions of the total incoming irradiation (G) that are reflected, absorbed, and transmitted, respectively. The sum of these fractions must equal the intensity of the incident beam at each wavelength λ:

$$\rho G + \alpha G + \tau G = G. \quad (1.1)$$

Or equally:

$$\rho_\lambda + \alpha_\lambda + \tau_\lambda = 1 \quad (1.2)$$

If a body is opaque like in the case of metals, the transmission term is equal to zero, and eq (1.2) becomes (1.3):

$$\alpha_\lambda = 1 - \rho_\lambda \quad (1.3)$$

An absorber is efficient when the absorption, in the wavelength of the solar spectrum is maximized. Being metals notoriously reflective, the surface exposed to the glass, dedicated to solar light absorption, is commonly coated by absorbing materials reaching fractions of total absorbed solar light above 90%.

Another important parameter to optimize in solar absorber design is thermal emittance. Thermal emittance refers to the thermal radiation emitted by an object and is defined as the ratio of the power

emitted by the object itself to the power emitted by a blackbody at the same temperature eq. (1.4). The thermal radiation spectrum for most solar thermal applications is generally limited to the infrared range (approximately 1 μm to 50 μm). The surface emissivity (ε_λ) of the absorber material influences both absorption and emission mechanisms.

$$\varepsilon\,(T) = \frac{\int_0^\infty \varepsilon\,(\lambda)\, B_\lambda\,(T)\, d\lambda}{E_{BB}(T)} \tag{1.4}$$

Where ε(λ) is the surface emissivity, $0 \leq \varepsilon \leq 1$, $B_\lambda\,(T)$ is the fraction of energy emitted by a blackbody at temperature T while E_{BB}(Wm^{-2}) is the total emitted power obtained by integrating the blackbody spectral irradiance over all the wavelengths:

$$E_{BB} = \sigma_{SB}\, T^4 \tag{1.5}$$

Being σ_{SB} (Wm^{-2}K^{-4}) the Stefan-Boltzmann constant.

According to Kirchhoff's law of radiation, in a steady-state condition of thermal equilibrium, the spectral emissivity (ε_λ) regulates both absorption and emission mechanisms. The spectral absorptivity (α_λ) is equal to the spectral emissivity (ε_λ) (eq. 1.6).

$$\alpha_\lambda = \varepsilon_\lambda \tag{1.6}$$

Because of this, $\varepsilon\lambda$ regulates the overall radiative performance of the absorber that is enclosed into two parameters: the spectrally averaged solar absorptance α and spectrally averaged thermal emittance ε over the relevant wavelengths λ:

$$\alpha(T) = \frac{\int_0^\infty (1-\rho_\lambda)\, S(\lambda)\, d\lambda}{\int_0^\infty S(\lambda)\, d\lambda} \tag{1.7}$$

$$\varepsilon\,(T) = \frac{\int_0^\infty (1-\rho_\lambda)\, B_\lambda(\mathrm{T})\, d\lambda}{\int_0^\infty B_\lambda(\mathrm{T})\, d\lambda} \tag{1.8}$$

where Sλ(T) indicates the solar spectral irradiance (Wm^{-3}).

Understanding these principles of optics allows us to design solar absorbers that efficiently absorb solar radiation while minimizing reflection and thermal radiation losses. By optimizing the absorber's optical properties, such as its absorption coefficient and thermal emittance, the efficiency and performance of solar energy systems can be significantly enhanced.

1.2.2 Selective Solar Absorbers for HVFPCs

Selectivity refers to the ability of a solar absorber to distinguish between wavelengths in the solar spectrum and those in the infrared range associated with blackbody radiation temperatures.

A solar absorber is considered a Selective Solar Absorber (SSA) when it exhibits high absorptance in the solar spectrum (0.3-2.5 μm) and low emissivity in the infrared region (λ > 2.5 μm). SSAs are designed to efficiently absorb sunlight across a wide range of wavelengths while minimizing the re-emission of absorbed heat as thermal radiation. Ideally, the behavior of an SSA would closely resemble the dash-dotted lines depicted in Figure 1.7, demonstrating an absorptivity curve described by eq. (1.9):

$$\alpha_\lambda = \begin{cases} 1, & if \ \lambda < \lambda_{cut}(T) \\ 0, & if \ \lambda > \lambda_{cut}(T) \end{cases} \qquad (1.9)$$

Here, λ_{cut} (T) represents the cut-off wavelength, which signifies the transition wavelength from high to low absorptivity that maximizes efficiency at a specific operating temperature.

In general, this transition occurs at the wavelength where blackbody emission surpasses incident solar radiation [41], and it decreases with increasing operating temperature, as illustrated in Figure 1.7. When the operating temperature exceeds 200 °C, the blackbody emission starts overlapping the solar spectrum, and λ_{cut} is such that a significant portion of the solar spectrum falls within the range where α_λ = 0. Consequently, a portion of the incoming solar radiation is lost in favor of reduced thermal radiation losses (Figure 1.7).

While achieving the ideal behavior of an SSA may not be feasible, the objective is to obtain a spectrum that closely approximates the ideal curve based on the collector's operating temperature. Temperature plays a crucial role in SSA design, and appropriate consideration must be given to the significance of α and ε. Cao et al. conducted an in-depth analysis of this subject in 2015 [41].

They proposed a formula for quantitatively estimating the relative importance of α and ε in various solar thermal applications, introducing two important concepts in SSA design: absorber efficiency (η_{abs}) and weighting factor (w), expressed by equations (1.10) and (1.11) respectively:

$$\eta_{abs} = \frac{q_h}{G_{Sun}\, C} = \alpha - w\varepsilon \qquad (1.10)$$

$$w = \frac{\sigma_{SB}(T_{abs}^4 - T_{amb}^4)}{G_{Sun}\, C} \qquad (1.11)$$

The absorber efficiency (η_{abs}) represents the ratio of heat directed to the pipes of the collector (q_h) to the total solar irradiance incident on the absorber (G_{Sun}), accounting for the presence of the concentration factor (C) resulting from reflectors. η_{abs} is also expressed as a combination of α and ε through the weighting factor (w), which determines the relative importance between the two parameters. The weighting factor (w) is defined as the ratio of the maximum heat exchangeable via radiation with the ambient temperature (T_{amb}) to the solar light incident on the absorber (G_{Sun}) multiplied by C.

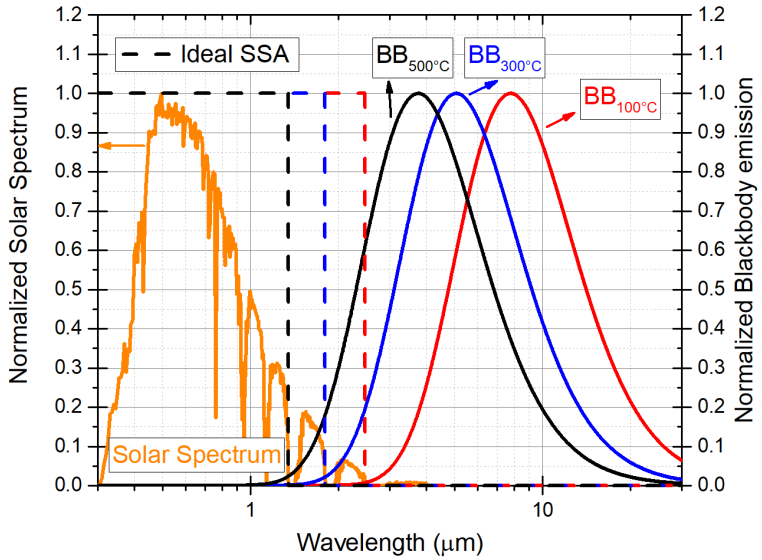

Figure 1.7 Normalized solar spectral irradiance (orange line) and normalized BB emission spectra at different temperatures: 100 °C (solid red line), 300 °C (solid blue line), and 500 °C (solid black line). Ideal absorptivity curves for solar selective absorbers with different cut-off wavelength λ_{cut}, depending on the operating temperature (dashed lines).

In other words, w quantifies the relative significance of the emission mechanism compared to light absorption. Figure 1.8 illustrates the calculated values of w using equation (1.11) as a function of the absorber temperature (T_{abs}) for three different concentration factors (C = 1, 10, and 100) with a fixed ambient temperature (T_{amb}) of 25 °C and solar irradiance (G_{Sun}) of 1 kW/m². The yellow zone highlights regions where w exceeds 1, which is unique to evacuated flat plate panels without concentration. As expected, for a fixed concentration factor (C), increasing the absorber temperature (T_{abs}) leads to an increase in w, while for a fixed T_{abs}, increasing C reduces w. This graph provides insights into the situation regarding plate absorbers for unconcentrated panels. The absence of reflectors limits the applicability of Fig. 1.8 to the curve C = 1. Traditional non-evacuated flat panels typically reach a maximum temperature of around 100 °C, resulting in significantly lower values of w. However, due to the high vacuum insulation, operating temperatures can reach values up to 200 °C, causing w to increase up to 2.

This substantial change in w is not observed in other solar devices utilizing concentration, as the absorption mechanism consistently outweighs emission ($w < 1$).

The realization of an SSA with ideal properties can be highly challenging. Maintaining ultra-low emissivity at high temperatures, especially within a single structure subject to significant temperature variations, proves complex. Additionally, it is important to consider the possibility of a finite slope in the transition range of the absorptance curve, as achieving an abrupt transition from high absorptance to low emissivity is difficult in practice. Various materials and designs have been explored to develop selective solar absorbers, including multilayer coatings, nanostructured surfaces,

and plasmonic materials. These approaches aim to optimize the absorption of sunlight while minimizing thermal radiation losses.

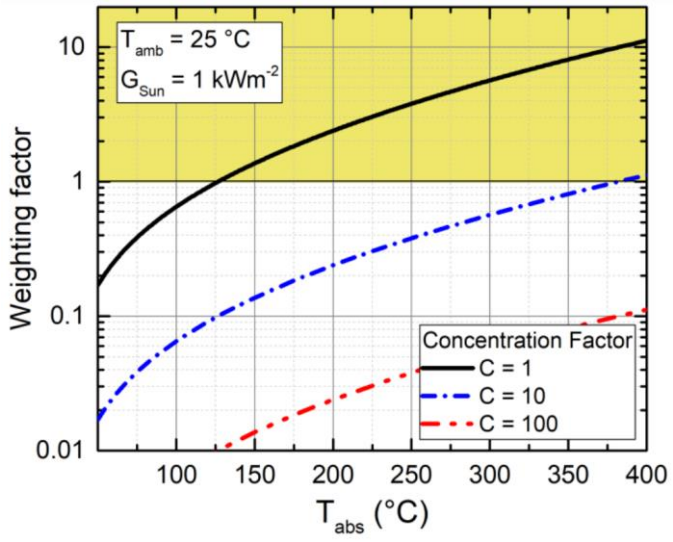

Figure 1.8 The weighting factor w calculated by eq. 1.11 as a function of the absorber temperature T_{abs} for three concentration factors C = 1, 10, and 100 for a fixed ambient temperature T_{amb} = 25 °C and solar irradiance G_{Sun} of 1 kWm^{-2}. The yellow zone highlights the points where w is bigger than 1, which is the unique condition of evacuated flat plate panels without concentration.

Multilayer coatings typically consist of a stack of thin films with different optical properties. By carefully designing the thickness and refractive index of each layer, it is possible to create interference effects that enhance absorption in the solar spectrum and reduce emissivity in the infrared range [42]. For example, a common configuration for a multilayer coating is to alternate layers of a high-refractive-index material (such as tantalum pentoxide) and a low-refractive index material (such as silicon dioxide). This design exploits the interference of light waves reflected at each layer interface to enhance absorption and suppress thermal emission.

The currently employed SSA in the HVFPCs by TVP Solar is the commercial Mirotherm 1300, manufactured by Alanod [23]. This SSA utilizes an aluminum strip combined with an innovative three-layer absorber. Figure 1.9 presents the emissivity spectrum of the absorber and the blackbody (BB) emissions at three distinct temperatures.

The design of the absorber is primarily optimized for operation at low temperatures. It exhibits favorable performance at 100 °C, but as the temperature increases to 200 °C and beyond, thermal losses begin to rise. This increase in thermal losses can be observed in the thermal emittance curves depicted in Figures 1.9 c) and 1.9 d), where they intersect with the emissivity of the commercial absorber in a region where the emissivity is still high. It is important to note that heat losses escalate with the operating temperature, as governed by Planck's law.

Consequently, when operating at temperatures exceeding 250 °C, the cut-off wavelength (λ-cut) shifts towards shorter wavelengths, leading to an amplified proportion of heat loss.

Significant advancements have been made in recent years with the development of an easily fabricated SSA based on a sputter-deposited $Cr_2O_3/Cr/Cr_2O_3$ multilayer design. This design exhibits intriguing optical properties [43] and demonstrates good thermal stability [44]. Further details regarding the design and realization of new optimized SSAs for HVFPCs will be provided in the subsequent chapter.

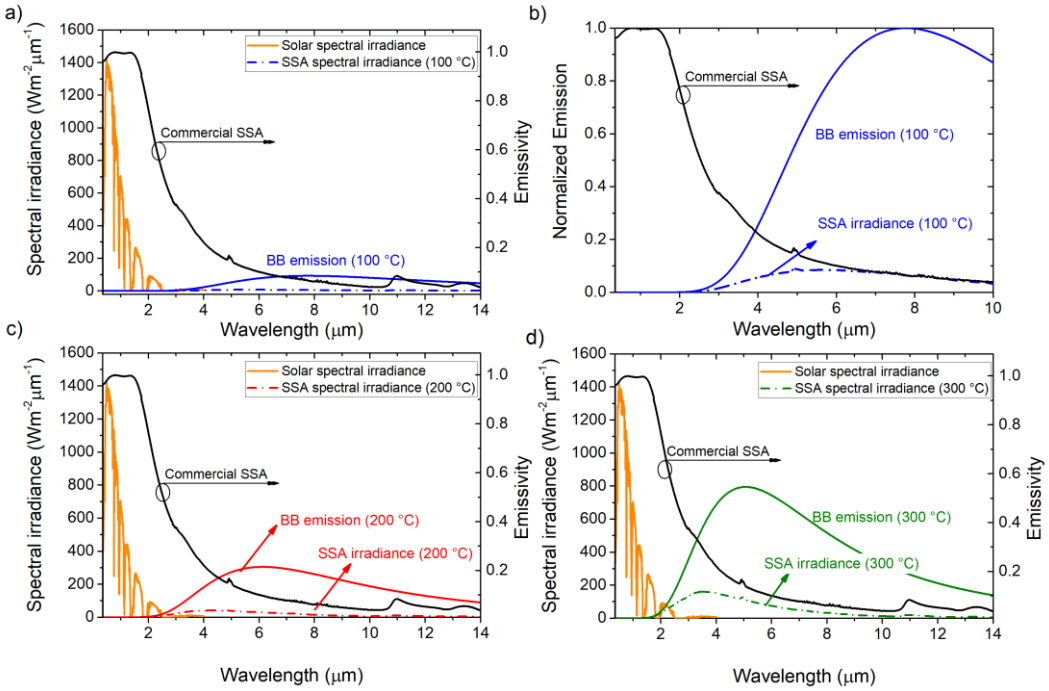

Figure 1.9: Left-hand axis: Solar spectral irradiance (orange line), BB (continuous lines) and SSA (dash-dotted lines) irradiance at different temperatures: (a) 100 ◦C (blue line), (c) 200 ◦C (red line), and (d) 300 ◦C (green line). Right-hand axis: emissivity of a commercial absorber (Mirotherm, black line). (b) Enlarged view of Fig.(a) showing the low emittance of the commercial SSA working at 100 ◦C.

1.3 TVPSOLAR MT-POWER HVFPC STANDARD EFFICIENCY

Thermal efficiency is the most significant parameter for expressing the performance of a thermal solar collector [45]. Its general expression is the ratio between the useful thermal power (Qu) transferred to the heat transfer fluid (HTF) and the incident solar irradiation (G) on the collector aperture surface (Ac) [46]:

$$\eta_{th} = \frac{Q_u}{G * A_c} \qquad (1.12)$$

The "Hottel-Willier-Bliss equation" [47] is commonly utilized for measuring collector energy:

$$Q_u = F_R A_c \ [G(\tau\alpha)_e - UL(T_{f,i} - T_{amb})] \quad (1.13)$$

Here F_R is the collector heat removal factor obtained from a test in which the heat loss term is zero; $(\tau\alpha)_e$ is the effective transmittance absorptance product derived from measurements of cover transmittance and collector reflectance; UL is the overall heat loss coefficient determined from a test in which insolation equals zero, $T_{f,i}$ is the temperature of the entering HTF while T_{amb} is the ambient temperature.

Replacing the expression (1.13) in the (1.12):

$$\eta_{th,HWB} = \frac{F_R A_c \ [G(\tau\alpha)_e - UL(T_{f,i} - T_{amb})]}{G * Ac} \quad (1.14)$$

This expression includes a first-order dependence on temperature difference ($T_{f,i}$-T_{amb}).

Currently, the most common expression (equation (1.15)) used to describe flat plate collector efficiency approximates thermal losses with a second-order dependence on the difference between the average of the working fluid temperatures at the inlet and outlet of the collector (T_m) and the ambient temperature (T_{amb}) [48]. This expression is also widely used in solar key mark certification and will be referred to as the standard efficiency in this manuscript expressed as equation (1.15):

$$\eta_{th,st} = \eta_0 IAM_\theta - \left[\frac{c_1(T_m - T_{amb}) + c_2(T_m - T_{amb})^2}{G}\right] \quad (1.15)$$

where η_0 is the zero-loss efficiency (when the fluid temperature is identical to the ambient temperature T_{amb}). The factors c_1 and c_2 are the first and second-order heat loss coefficients, respectively. The incidence angle modifier (IAM_θ) function describes the optical efficiency for a certain radiation incidence angle θ normalized by optical efficiency evaluated at perpendicular irradiation conditions [49].

The different irradiation components G_{bt}, $G_{st,}$ and G_{rt} are weighted by individual Incidence Angle Modifiers (IAM) $K_{b,}$ $K_{s,\ and}$ K_r to take into account the changes in the conversion factor due to non-perpendicular irradiance of these radiation components [50]. For dynamic collector tests K_s, and K_r are summarized in one single IAM K_d for diffuse irradiance from the overall collector hemisphere. This K_d is a constant collector parameter determined for isotropic diffuse irradiance and it is provided in collector test reports. Therefore, K_b is usually approximated according to [51]:

$$K_b(\theta_L, \theta_T) = K_b(\theta_{L,}0) * K_b(0, \theta_T) \quad (1.16)$$

where θ_L and θ_T are the projection of θ (angle between solar beam and the collector surface normal) into the longitudinal and transversal collector planes. The TVP-Solar MT-Power efficiency coefficients are reported in Tab.1.1 and Tab.1.

2

Tab. 1.1 MT-Power efficiency coefficients

Coefficients	Value
η_0	0.737
c_1	0.5
c_2	0.006
K_d	0.95

Tab. 1.2 MT-Power Incident Angle Modifiers

Incident Angle θ	$K_b(\theta_L,0)$	$K_b(0,\theta_T)$
0	1.0	1.0
20	1.0	1.0
30	0.99	0.99
40	0.98	0.98
50	0.95	0.95
60	0.88	0.88
70	0.72	0.72
90	0.00	0.00

The zero-loss efficiency η_0, the first-order heat loss coefficient c_1, the second-order heat loss coefficient c_2, and the Incident Angle Modifier coefficients are obtained through a standard test effected according to EN ISO:9806 2013 & ICC 901/SRCC 100-2015 carried out by Solar and Heat Technology Stuttgart (SWT), and are available online in the Solar Keymark database [52]. During the simulation, the medium fluid temperature is evaluated at every time step. Expressing the IAM coefficients, the standard efficiency expression (1.15) becomes (1.17):

$$\eta_{th,st} = \left[\eta_0 * \frac{K_b(\theta)G_B + K_d G_d}{G}\right] - \left[\frac{c_1(T_m - T_{amb}) + c_2(T_m - T_{amb})^2}{G}\right] \qquad (1.17)$$

In Fig. 1.10 (a) is represented the standard efficiency curve of TVP-Solar MT-Power HVFPC obtained from a standard test performed indoors at controlled conditions and normal irradiation (G= 950 Wm^{-2}, IAM_θ = 1 and T_{amb}= 20 °C) where the maximum operating average temperature T_m was equal to 200 °C.

If we look at Figure 1.10 (b) in which the HVFPC standard efficiency (black stars) is compared with the efficiencies of various types of non-concentrated collectors, it is evident that in the case of middle-temperature (150÷200 °C) applications, they represent the best solution [53].

As mentioned in Section 1.2, commercially available solar selective coatings such as Mirotherm® and Sunselect® from Alanod [23], as well as various types of TiNOx® coatings from Almeco [54], have demonstrated excellent performance up to temperatures of 150 °C. However, there is currently a lack of marketed solutions and research studies proposing optimized SSA coatings specifically designed for HVFPCs operating at higher temperatures. HVFPC technology operates in a unique range where high working temperatures without concentration necessitate careful consideration of both solar absorptance and thermal emittance in the design of selective coatings.

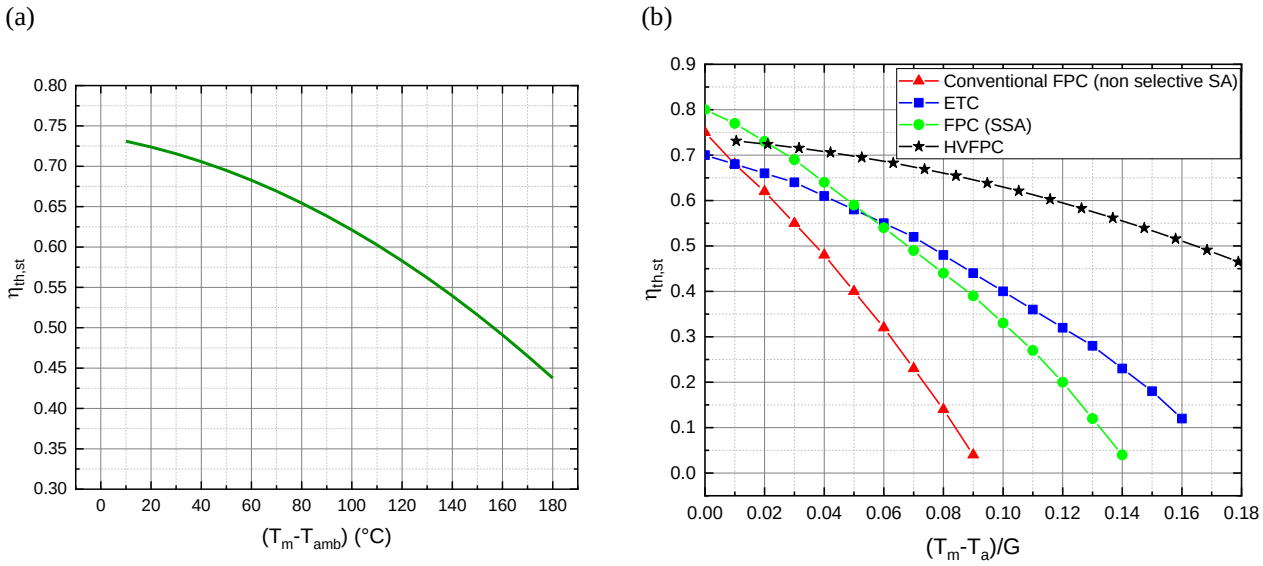

Fig. 1.10 Efficiency of HVFPCs: (a) Standard efficiency curve of TVPSolar MT-power; (b) Comparison of thermal standard efficiencies among various types of non-concentrated thermal collectors, represented in function of the variation of the dimensionless difference between the absorber and ambient temperature relative to the incident solar irradiation (W/m²)

In the following chapter, we will discuss two solutions that have been studied by our research group in recent years to enhance the efficiency of High Vacuum Flat Plate Collectors (HVFPCs) through the optimization of the optical properties of the selective solar absorber (SSA) used. Before delving into the details of these cases, the final section of this chapter will provide information regarding the experimental setups employed for the fabrication of these optimized coatings, as well as their optical characterization.

1.4 EXPERIMENTAL SET-UPS FOR COATINGS FABRICATION AND OPTICAL CHARACTERIZATION

This section provides an overview of the fabrication methods and characterization techniques used for thin films and coatings in absorber designs. The most commonly employed technique is Physical Vapor Deposition (PVD), which encompasses various vacuum-based deposition methods. PVD involves evaporating the target material from a solid or liquid source and condensing it in a solid phase onto the substrate [55] . Sputtering and evaporation are the widely used PVD techniques.
To characterize the properties of the fabricated coatings, several techniques are utilized, including scanning probe methods, photon, electron, and ion methods [56]. These techniques enable the investigation of surface composition, depth distribution, film thickness, structure, and roughness.
In the following will be introduced the PVD fabrication methods and thin film characterization instrumentation employed in this study. Additionally, it describes a custom-made calorimetric instrument developed in collaboration with TVP Solar [57] and CNR-ISASI [58] of Naples.

1.4.1 Physical Vapor Deposition (PVD) via Sputtering

Sputtering deposition is a physical vapor deposition technique based on the sputtering phenomenon. When a solid surface is bombarded with energetic ions, the surface atoms of the solid are scattered backward due to collisions between the surface atoms and the energetic particles [59]. Sputtering allows for the deposition of film coatings with thicknesses ranging from a few Angstroms to micrometers. Various types of sputtering systems are available, including Direct Current (DC) diode, Radio Frequency (RF) diode, DC Magnetron Sputtering (DCMS), RF Magnetron Sputtering (RFMS), DC Reactive Magnetron Sputtering (DCRMS), and RF Reactive Magnetron Sputtering (RFRMS). The simplest system is the DC diode (fig. 1.11 (a)), where two planar electrodes (cathode and anode) are used. The cathode surface consists of the material to be sputter-deposited, while the substrates are placed on the anode. By applying a DC voltage between the electrodes and filling the vacuum chamber with an inert gas (usually Argon), a glow discharge (plasma) is generated. The generated Ar+ ions are accelerated towards the cathode, causing the sputtering of the target material onto the substrates. RF sputtering is used for insulating materials, where the electrical potential between the electrodes is alternated to prevent charge buildup on the target (fig. 1.11 (b)) [59]. Reactive sputtering occurs when atoms sputtered from a target (usually a metal target) and reactive molecules introduced during the deposition chemically react to form and deposit a compound thin film on the substrate. Reactive gases, such as pure reactive gases or mixtures of inert gas and reactive gas, are commonly used [59].

Reactive sputtering processes require control over parameters like the partial pressure of the reactive gas or the pumping speed to ensure the desired film quality. To increase the deposition rates and prevent process gas molecules from being included in the growing film, the chamber pressure is lowered. Magnetron sputtering is employed for this purpose (fig. 1.12).

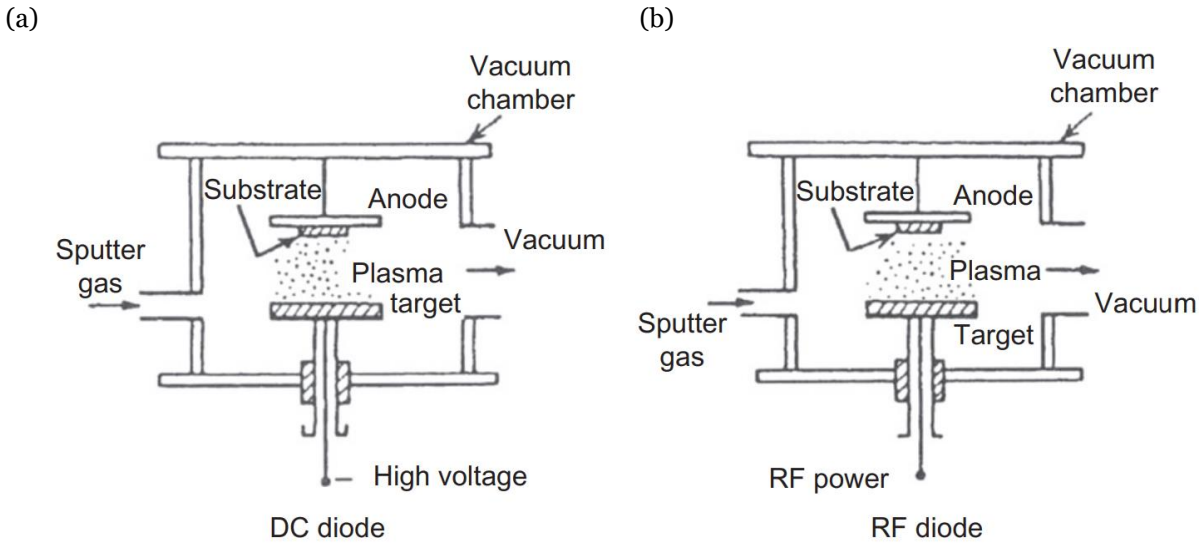

Figure 1.11 Sputter deposition systems: (a) DC and RF(b) diode. [59])

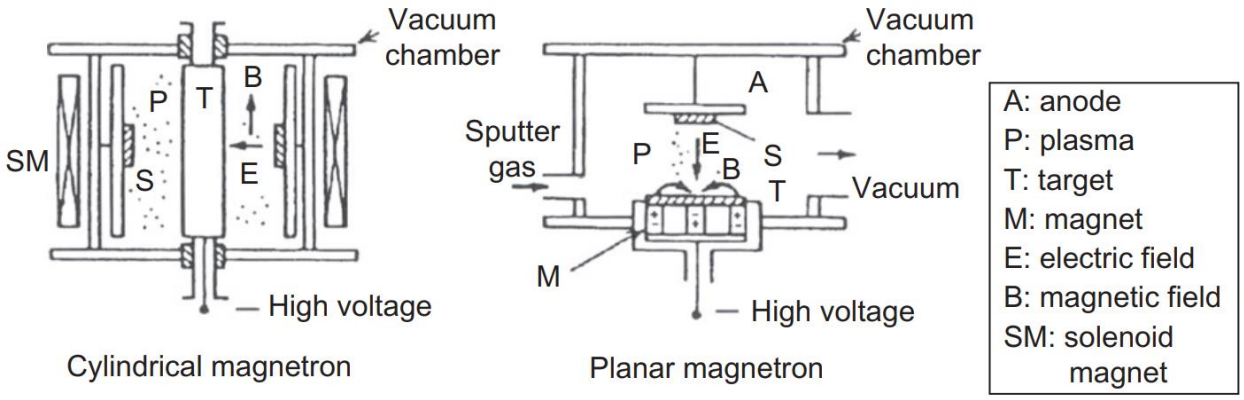

Figure 1.12 Sputter deposition systems: magnetron sputtering [59].

In magnetron sputtering systems, a magnetic field is utilized to trap electrons in the glow discharge, increasing the collision rate between electrons and process gas molecules and sustaining the plasma. The higher plasma density in the presence of a magnetic field enhances the sputtering rate at the target [59]. The sputtering system used for depositing the multi-layer coating samples in this study is depicted in Figure 1.13. The system consists of a cylindrical vacuum chamber equipped with four sputtering targets of 10 cm diameter positioned at 90 degrees from each other. A rotating supporting disc with four sample holders allows for the placement of substrates under the desired cathode,

enabling the deposition of up to four different materials without breaking the vacuum. The distance between the cathodes and the substrate is set to 10 cm, and the substrate remains static during deposition. Pressure in the chamber is measured using a capacitance gauge, and the samples are loaded the day before and pumped down overnight to achieve a base pressure of approximately $2x10^{-5}$ Pa. A rotating shutter located near the cathodes controls the deposition time and layer thickness.

Figure 1.13 Sputtering deposition system. The sputtering apparatus (a). Sputtering targets (b). Rotating supporting disc with four sample holders (c).

1.4.2 Physical Vapour Deposition (PVD) via Electron Beam

Another commonly employed technique for thin film deposition is Electron Beam Deposition (EBD). EBD is a type of Physical Vapor Deposition (PVD) method that utilizes an electron beam to evaporate the target material and deposit it onto a substrate. This technique offers precise control over film thickness and composition, making it suitable for various applications ranging from microelectronics to optical coatings.

In EBD, a high-energy electron beam is generated and focused onto the target material in a vacuum chamber. The beam is typically produced by an electron gun, which consists of a heated filament that emits electrons and an accelerating anode that accelerates the emitted electrons toward the target. The electron beam impinges on the target surface, causing the target material to vaporize and form a plume of evaporated atoms or molecules. Vapors of the target material will deposit on the substrates properly arranged in the upper part of the vacuum chamber. To prevent unwanted reactions with ambient gases, the deposition process is carried out under high vacuum conditions. By controlling the beam energy and the target-substrate distance, the deposition rate and film thickness can be precisely regulated. Additionally, the use of electromagnetic coils allows for the manipulation of the beam's position and shape, enabling uniform deposition across large substrate areas.

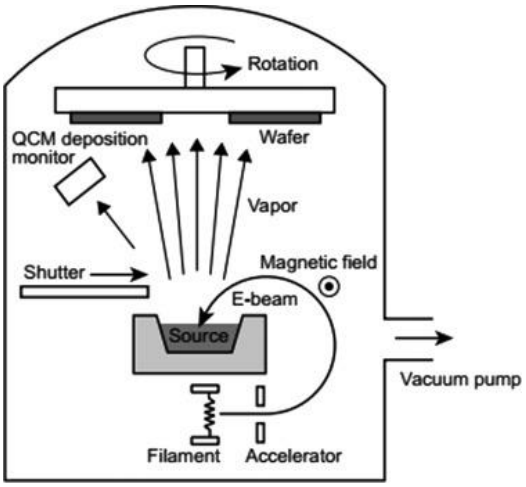

Figure 1.14 Electron beam physical vapor deposition technique, scheme of concept ([60])

In an EBD system (Fig. 1.14), a vacuum chamber houses the electron gun, target material, substrate, and other necessary components. The chamber is evacuated to a high vacuum level to eliminate gas molecules that could interfere with the deposition process.

The electron gun emits a focused electron beam, which is directed towards the target surface. The target material, typically in the form of a solid rod, pellet, or crucible, is positioned in the beam's path. As the electron beam strikes the target, the material evaporates and forms a vapor plume that travels towards the substrate.

The substrate, on which the thin film is to be deposited, is placed at a specific distance from the target. Rotating sample holders are often used to guarantee the thickness uniformity of the deposited film on the substrate. Precise control of the substrate temperature and positioning allows for additional control over film properties, such as crystallinity and adhesion.

Various in-situ monitoring techniques, such as quartz crystal microbalances or optical sensors, can be employed to measure the deposition rate and monitor film thickness during the process. These measurements help ensure the desired film properties are achieved.

Figure 1.15 illustrates the electron beam apparatus utilized for depositing the multilayer absorbers described in this study. The deposition chamber features an electron beam evaporation source and four routable crucibles (Figure 1.15 (d)), enabling the deposition of multiple layers without breaking the vacuum. The e-beam system incorporates a rotating planetary (Figure 1.15 (c)), ensuring uniform thickness across the samples and allowing for simultaneous deposition on multiple substrates. To monitor the temperature, a thermocouple is employed, and the samples are maintained below 80 °C throughout the process. Before deposition, the vacuum chamber is pumped down to a base pressure of 10^{-5} Pa, and the materials undergo a slow outgassing phase to remove impurities. The deposition process is controlled using a thickness monitor (Inficon model XTC/3).

The thickness monitor's tooling factor is calibrated by depositing a thicker layer (approximately 500 nm) and measuring it with a profilometer (KLA Tencor P-15). The desired step thickness is obtained through a lift-off procedure in acetone using standard photolithography. The thickness monitor automatically adjusts the e-beam current to maintain a constant evaporation rate and utilizes a shutter to halt deposition once the desired thickness is achieved. Through careful calibration, a thickness control accuracy of approximately 1 nm is achieved. All depositions in this study were performed on smooth, unheated glass substrates with a roughness of 1 nm.

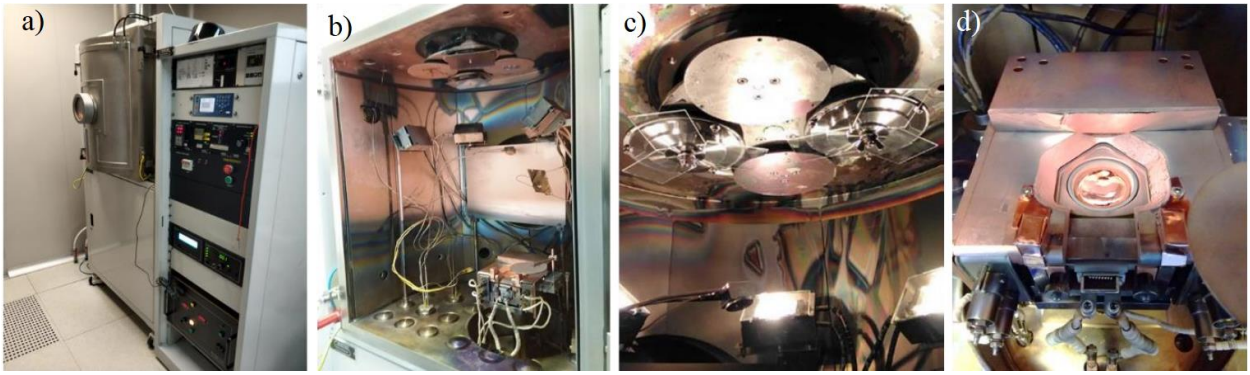

Figure 1.15 E-beam deposition system. The electron beam apparatus (a). Vacuum chamber (b). Glass substrates mounted on the rotating planetary (thickness monitor sensor is also visible) (c). Multiple crucible e-gun and copper crucible (d).

1.4.3 Absorptance and thermal emittance measurements apparatus: Mini Test Box

The Mini-Test-Box (MTB) is a custom experimental apparatus designed for measuring the absorptance and thermal emittance of selective solar absorbers (SSA) under operating conditions of high vacuum and high temperatures [61]. The MTB, as shown in Figure 1.16, consists of a stainless-steel high-vacuum chamber with an extra-clear float glass cover. The absorber is suspended by four thermally insulating springs (visible in Figure 1.16 (c)). The chamber maintains an internal pressure below 10^{-3} Pa using a turbomolecular pump to eliminate convection and reduce thermal conduction from residual gases.

Temperature measurements are taken using a thermocouple attached to the sample, as well as additional thermocouples monitoring the vessel and the glass temperature. Indoor measurements are performed using an array of calibrated LED lights to ensure uniform light irradiance (Figure 1.16 (b),(c)) [62]. The MTB is also equipped with tilting support and a pyranometer for conducting outdoor measurements under direct solar illumination [63] (Figure 1.16 (a)). The MTB employs a calorimetric approach to measure the absorptance and thermal emittance.

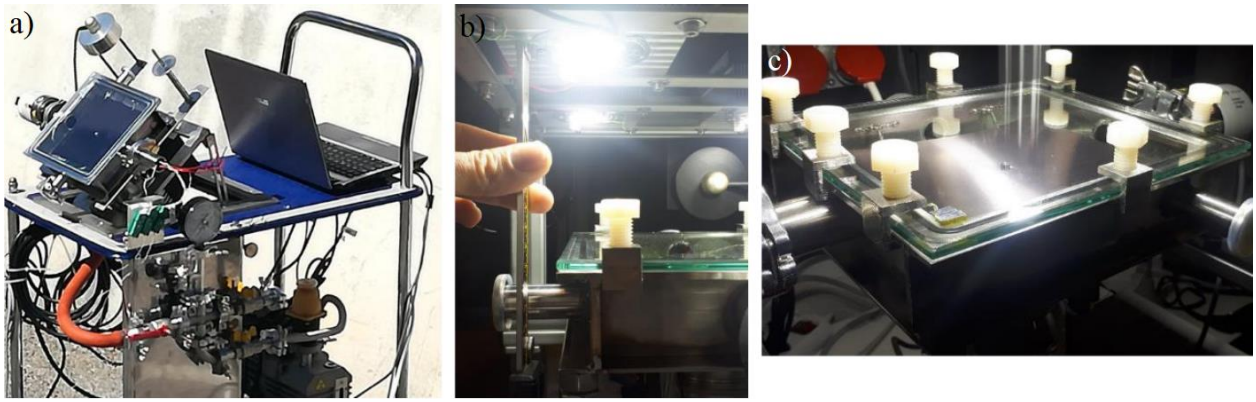

Figure 1.16 Mini Test Box apparatus under direct solar illumination (a) and under LED light illumination (b and c).

The temperature variations of the sample are directly related to the absorbed power and the radiative power losses according to the power balance equation:

$$m_a\, c_p(T_m)\frac{d\,T_m}{dt} = \alpha_L\, A\, \tau\, P_{in} - \bar{\varepsilon}_a(T_m)\,\sigma_{SB}\,A\left(T_m^4 - T_{amb}^4\right) - \bar{\varepsilon}_{sub}(T_{sub})\,\sigma\,A\left(T_m^4 - T_{amb}^4\right) \quad (1.18)$$

Here, m_a represents the sample mass, c_p is the specific heat, α is the absorptance, A is the sample area, P_{in} is the incident power per unit area, $\bar{\varepsilon}_a(T_m)$ is the absorber emittance and $\bar{\varepsilon}_{sub}(T_{sub})$ is the equivalent substrate emittance.

During the cooling down phase, when illumination is stopped and $P_{in} = 0$, Equation 1.18 can be used to evaluate the thermal emittance of the sample = $\bar{\varepsilon}_a(T_m) + \bar{\varepsilon}_{sub}(T_{sub})$ being the only unknown term. Once $\varepsilon_{sample}(T_m)$ has been calculated, Equation 1.18 can be solved during the heating-up phase to evaluate α. More details about the measurement procedure can be found in references [64] and [65]. The behavior of the absorber in the MTB has also been simulated using COMSOL Multiphysics [66].

The MTB also enables experimental measurements of the efficiency of a solar coating at different temperatures through stagnation measurements (until maximum achievable absorber temperature). The absorber is illuminated with varying light powers using a calibrated LED illumination system [62], and the absorber stagnation temperature is recorded. In this configuration, the power losses are equal to the absorbed power:

$$\varepsilon(T_S)\;\sigma_{SB}(T_s^4 - T_{amb}^4) + \varepsilon_{sub}\,\sigma_{SB}(T_s^4 - T_{amb}^4) = \tau_{glass}\,\alpha_L\,P_{LED}(T_S) \quad (1.19)$$

where the solar spectrum is replaced by the spectrum of the LED lump used to illuminate the absorber [62], $P_{LED}(T_S)$ is the light power provided by the calibrated LED system and T_S is the absorber stagnation temperature at the given LED power. As consequence, at $T = T_S$ the efficiency can be calculated, as reported below:

$$\eta(T) = \tau_{glass}\,\alpha_s - \frac{\tau_{glass}\,\alpha_L\,P_{LED}(T_S)}{H} \quad (1.20)$$

Where H is the irradiated power (the reference H set power is equal to 1000 Wm^{-2}).

1.4.4 Materials refractive indices measurements via Ellipsometry

Refractive index measurements using ellipsometry are a powerful technique for characterizing the optical properties of materials.

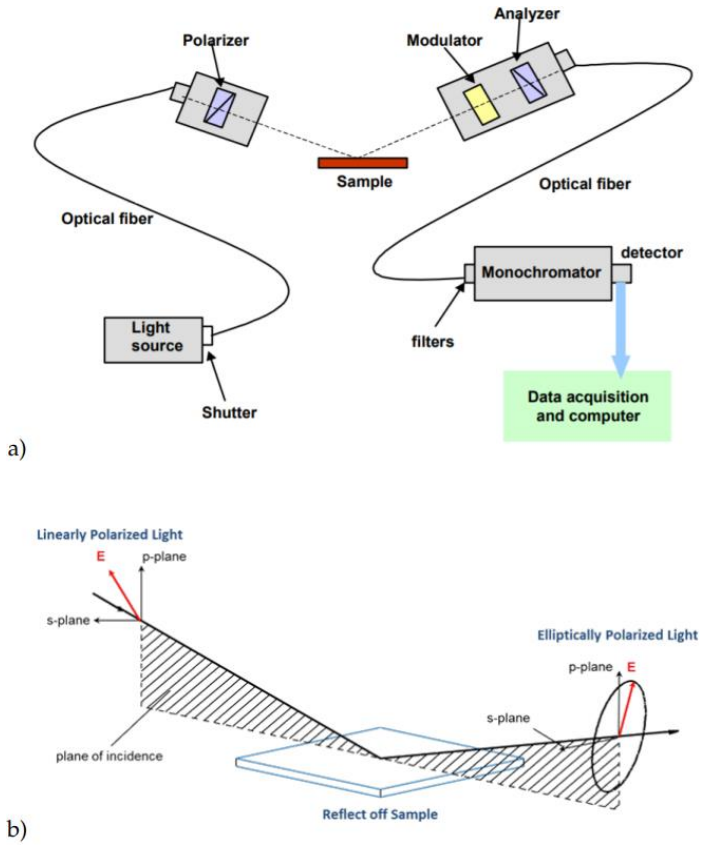

Figure 1.17 (a) Layout and (b) working principle of a classical ellipsometer.

Ellipsometry is based on the principle of measuring changes in the polarization state of light reflected from a sample surface. By analyzing the changes in the phase and amplitude of the reflected light, ellipsometry can determine the complex refractive index of a material, which consists of both the refractive index and the extinction coefficient. This non-destructive and contactless method is particularly useful for thin film characterization, as it can provide information about layer thickness, surface roughness, and optical constants. By varying the incident angle or wavelength of light, ellipsometry can be utilized for spectroscopic measurements, allowing for the determination of refractive index as a function of energy or wavelength. Overall, ellipsometry is a valuable tool for investigating the optical properties of materials and is widely employed in fields such as semiconductor technology, thin film coatings, and surface science research.The structure of an ellipsometer typically consists of several key components (Figure 1.17). It includes a light source, which can be a laser or a broadband light source, that emits polarized light.

This light is then directed towards a polarizer, which further controls the polarization of the incident light. The polarized light is then focused onto the sample surface using a beam splitter or mirrors.
After interaction with the sample, the reflected light is collected by an analyzer, which is another polarizer that can be rotated to analyze the change in polarization state induced by the sample. The analyzer is typically followed by a detector, such as a photodetector or a charge-coupled device (CCD), that measures the intensity of the reflected light.
To accurately measure the change in polarization, the ellipsometer also includes a rotating compensator, which introduces a controlled phase shift between the p-polarized and s-polarized components of the light. This phase shift enables the determination of the complex ratio of the reflection coefficients, known as the ellipsometric parameters.
The ellipsometer structure is complemented by a control unit or computer, which is responsible for controlling the instrument components, acquiring and analyzing data, and providing the final measurement results. The control unit also includes software for data processing and fitting algorithms to extract the optical parameters, such as the refractive index and thickness of thin films, from the measured ellipsometric data.
The change in polarization of light is quantified by the amplitude ratio and phase difference:

$$\rho = \frac{r_p}{r_s} = \tan(\psi)e^{i\Delta},$$

$$\tan(\psi) = \frac{|r_p|}{|r_s|} \in [0, 90°], \qquad (1.21)$$

$$\Delta = \delta_p - \delta_s \in [0, 360°].$$

The quantities r_p and r_s are the Fresnel reflection coefficient for s- and p-polarization, respectively, while ψ and Δ are the ellipsometric angles: from them, it is possible to obtain the optical properties of the sample. Unfortunately, they cannot be directly converted into the optical constants of the material but are used to validate a material structure model that allows to prediction of the material optical properties, i.e. the complex refractive index, employing mathematical relations, and dispersion formulae. There are several degrees of freedom in this analysis: incident angle, as well as thickness, roughness, and refractive index of each layer included in the sample. Any of these properties is varied to improve the match between experiment and calculation. Therefore, it is important to carefully choose the model and control the χ^2 value returned by the fit, which defines its quality. Figure 1.18 shows an example of the measured quantities Ic and Is, which are functions of ψ and Δ according to:

$$I_s = \sin(2\psi) \cdot \sin(\Delta), \qquad (1.22)$$

$$I_c = \sin(2\psi) \cdot \cos(\Delta).$$

and the relative fit lines, which agree with the measurement. In our analysis, the model used to fit the ellipsometric data faithfully reproduces the experimental samples. Also, two additional thin layers were included to simulate the roughness at the interface between the substrate and the film and on the film surface, as shown in Fig. 1.19. Measurements must be conducted at the Brewster angle (θ_B) of the substrate, where the highest sensitivity is observed. It corresponds to an angle of incidence at which the p-polarized light is perfectly transmitted through a transparent dielectric surface, with no reflection. It can be calculated from the indices of the two media:

$$\tan(\theta_B) = \frac{n_1}{n_0} \qquad (1.23)$$

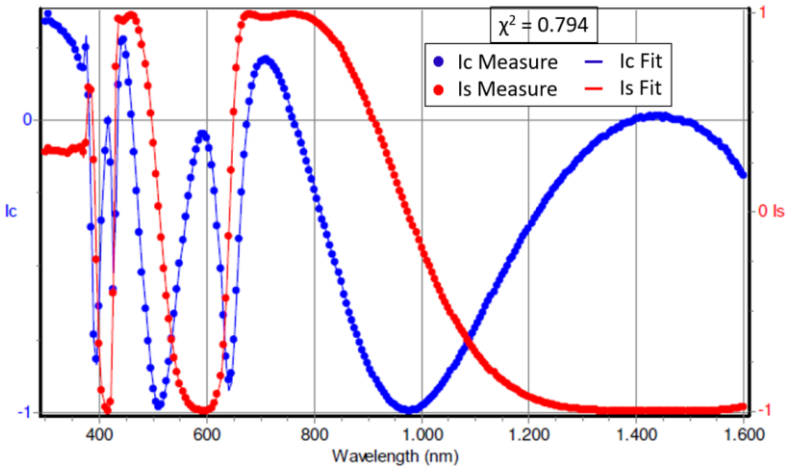

Figure 1.18 Example of a good fit ($\chi^2 < 1$): the ellipsometric measured quantities I_c and I_s (blue and red dots, respectively) and the fitted quantities (I_c as a blue line and I_s as a red line) are compared.

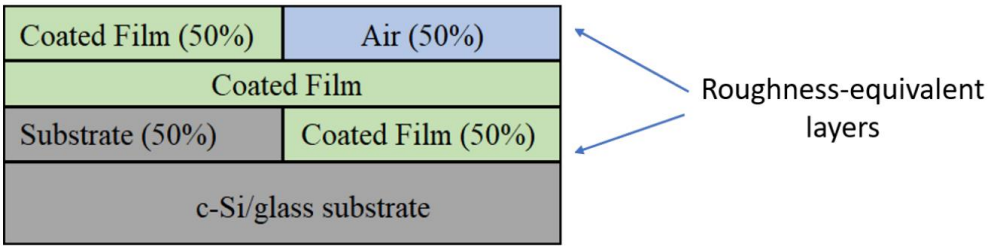

Figure 1.19 Diagram of samples (not to scale), including roughness-equivalent layers.

The samples in this study were measured using a Horiba Jobin Yvon - UVISEL spectroscopic ellipsometer (Fig.1.20) [67]. This ellipsometer is equipped with a xenon lamp and two detectors, allowing for analysis of the optical response in the wavelength range from 190 nm to 2100 nm. To ensure reproducible and reliable results, all films analyzed were deposited on a thick aluminum film, which can be considered optically infinite, and grown on a glass support to maintain optical flatness.

The use of an optically flat substrate allows for neglecting the impact of surface roughness in the thin film models. The incidence angle of the polarized light can be adjusted, and for the aluminum substrates, it was set to 70°.

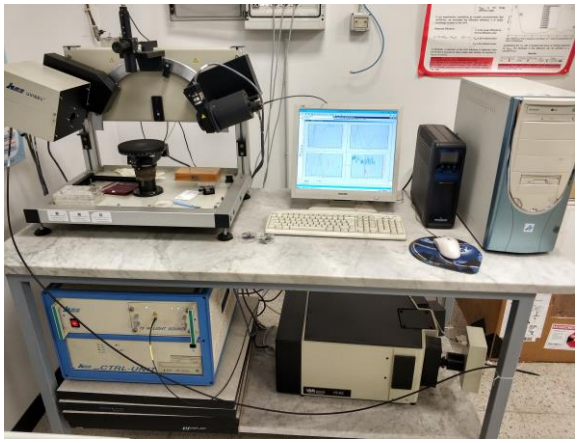

Figure 1.20 Spectroscopic ellipsometer Horiba Jobin Yvon – UVISEL, used for ellipsometric measurements

1.4.5 Materials reflectivity measurements (short wavelengths) with Integrating sphere and OSA

Hemispherical reflectance measurements in the short wavelength range of 350 to 1750 nm were conducted using an integrating sphere coupled with an Optical Spectrum Analyzer (OSA). The inner surface of the integrating sphere is coated with a diffusive material, ensuring a highly reflective surface and providing uniform radiation distribution through multiple Lambertian reflections. A light source illuminates the sample, and the spectrometer, connected to the integrating sphere, reads the fraction of light reflected by the sample. The OSA measures the spectral power (Wnm^{-1}) across the investigated wavelengths. By comparing the measurements with a reference sample of known reflectivity (ρref), the reflected power (ρ) can be estimated using eq. (1.24):

$$\rho = \frac{R_{sample}}{P_i} = \frac{R_{sample} \cdot R_{ref}}{P_i \cdot R_{ref}} = \frac{R_{sample}}{R_{ref}} \cdot \rho_{ref} \qquad (1.24)$$

where P_i is the power intensity incident on the sample, and R_{sample} and $R_{ref\ are}$ the spectral power reflected by the sample and by the reference sample, respectively. In this study, the reference sample used was the Spectralon WS-1-SL diffuse reflectance standard from Labsphere, known for its high reflectivity of 99% in the range of 400 to 1500 nm and > 96% reflectivity in the range of 250 to 2000 nm.Alternatively, for optical transmittance spectra in the range of 200 nm to 2500 nm, a spectrophotometer can be employed. The working principle, as shown in Fig. 1.21, involves a lamp as the light source, a diffraction grating acting as a prism to separate the light into different

wavelengths, and a rotating grating to select a specific wavelength of light that reaches the exit slit. At this point, the light interacts with the sample, and the detector measures the transmittance, representing the amount of light that passes through the sample and reaches the detector.

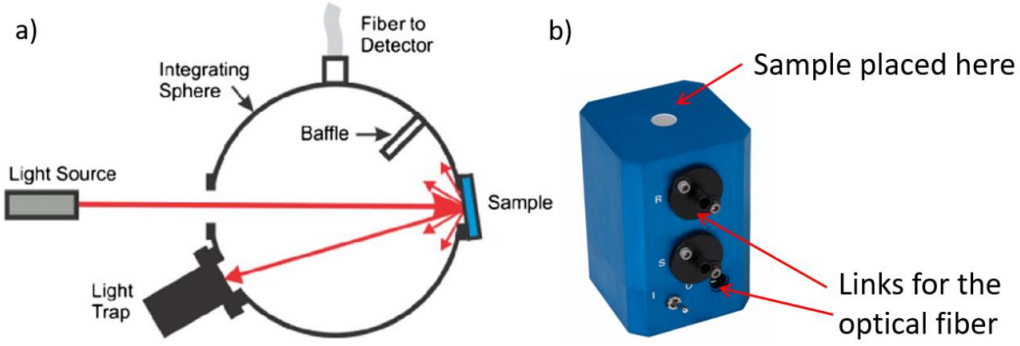

Figure 1.21 Working principle (a) and design (b) of the integrating sphere.

1.4.6 Materials reflectivity measurements (long wavelengths) with Fourier Transform Infrared Spectroscopy (FTIR)

Reflectance measurements in the range of 1.5 µm to 30 µm were performed using a Fourier-transform Infrared Spectrometer (FTIR). The working principle of the FTIR is illustrated in Figure 1.22. A broadband infrared light beam is directed to an interferometer, which generates an optical signal containing all the infrared frequencies. The light beam then interacts with the sample, which absorbs a portion of the light at specific wavelengths. By applying a Fourier Transform (FT) to the encoded signal, the intensity-time spectrum is converted into an intensity-frequency spectrum, enabling the estimation of spectral reflectance by comparing it with a reference sample.For near-infrared to far-infrared (NIR to FIR) measurements spanning 1.4 µm to 20.0 µm, a Jasco FT/IR 6300 Fourier Transform Infrared Spectrometer was utilized, with an aluminum film serving as the reference reflectance standard.

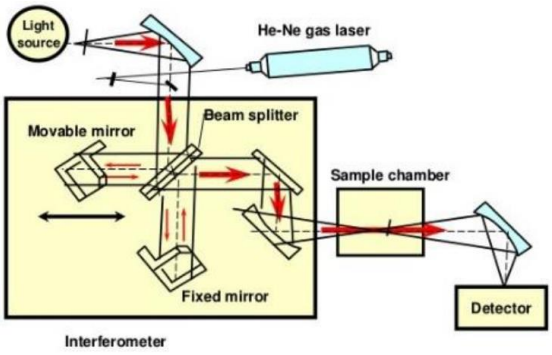

Figure 1.22 Fourier Transform Infrared Spectroscopy (FTIR), working principle.

1.4.7 Thin films thickness measurements via Profilometer

A profilometer is an instrument used for measurements of surface properties, i.e. roughness, step height, etc. Its working principle is shown in Fig. 1.23 (a) probe tip, in direct contact with the surface to measure, moves linearly along it record the vertical change (z-direction), which is useful to reconstruct the surface profile. Measurements of step height are usually obtained using standard photolithography, i.e. by applying a mask on the substrate before deposition and chemically removing it after deposition of the thin film and are useful to estimate the deposition rate. An example of this kind of measurement is shown in Fig. 1.23 (b)

(a) (b)

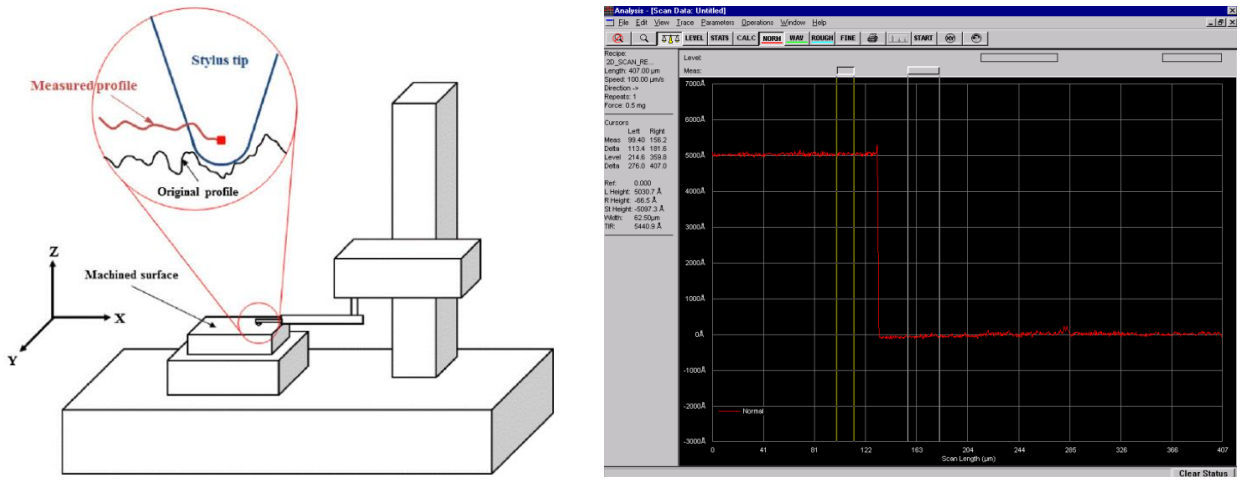

Figure 1.23 (a) Working principle of a stylus type profilometer [68], (b) Step height measurement measured with KLA Tencor P-15 profilometer.

In summary, in this chapter, we have provided detailed information on HVFPC technology. Before delving into the optimization of the SSAs developed over the years, the latter part of the chapter described the experimental setups used in the fabrication and optical characterization of these SSAs, which have been instrumental in supporting the research efforts.

2. IMPROVEMENT OF ENERGY CONVERSION EFFICIENCY IN HVFPCS

The aim of our research group project in recent years has been to develop methods to enhance the efficiency of High Vacuum Flat Plate Collectors (HVFPCs). We focused on optimizing coatings suitable for this emerging technology.

The efficiency of a solar absorber is determined by various factors, including thermal emittance, which represents the radiative losses. To improve the performance of a solar absorber for HVFPCs, it is beneficial to reduce the thermal emittance of the substrate. This can be achieved through better finishing of the back side of the substrate or by using a substrate with low thermal emittance, such as copper or silver.

One cost-effective way to significantly reduce the emissivity of both the selective coating and the substrate of a solar absorber is by using a low-emissive thin film coating. For example, Mirotherm® from Alanod [69] , which is currently used in TVP-Solar MT-Power, utilizes aluminum as the substrate. Russo et al. [70], [71] demonstrated that an aluminum thermal emittance value of ε_{Sub} = 0.045 best matches the experimental results for the Mirotherm® commercial coating. To further enhance the performance of this solar absorber, we explored the possibility of depositing a low emissivity coating, such as copper or silver (thermal emittance ≈ 0.02), on the back side of the absorber, specifically on the aluminum surface. The results of this study will be presented in the first paragraph of this chapter.

Another approach to improve the efficiency of HVFPCs at higher operating temperatures is to use selective solar absorbers (SSAs) with improved optical properties designed specifically for high-temperature applications. Among the various SSA designs, multilayer selective absorbers offer the advantage of controlling thermal emission while ensuring high solar absorption and excellent thermal stability [72]. The multilayer architecture allows for flexible design and optimization, as the thickness of the layers can be adjusted to accommodate different operating temperatures while keeping the overall architecture unchanged [73]. Multilayer absorbers consist of alternating thin dielectric layers (with high absorptance in the visible range and transparency in the infrared region) and metal layers that are partially transparent. An anti-reflective layer is often included to reduce reflections caused by the high refractive index of the dielectric materials, further enhancing the coating's performance. Similar to other selective solar absorber designs, a metallic IR reflector substrate is used. Chromium Oxide and Chromium have been identified as suitable materials for the dielectric and metal layers, respectively. These materials have been extensively studied, especially as ceramic-metal composites in commercial absorbers such as Mirotherm® or Sunselect® by Alanod [69]. Additionally, a

$Cr_2O_3/Cr/Cr_2O_3$ multilayer deposited by e-beam has also been investigated. Furthermore, these materials are relatively inexpensive and easy to handle. An additional SiO_2 layer is employed as an anti-reflective coating to enhance absorptance, while aluminum and copper serve as the metallic IR reflector substrate.

2.1 SUBSTRATE THERMAL RADIATIVE LOSSES REDUCTION (LOW EMISSIVE COATINGS)

In this paragraph, we will discuss the easiest strategy for enhancing the efficiency of HVFPCs, which involves reducing the power emitted from the back side of the absorber towards the panel's bottom case. Aluminum is generally considered the most suitable substrate material for most selective solar absorbers (SSAs) due to its low emittance (around 0.05), favorable workability, low cost, and high thermal conductivity. Moreover, after undergoing a proper baking procedure in a vacuum, aluminum is also one of the best materials for constructing ultra-high vacuum chambers. SSAs deposited on aluminum substrates have been successfully used in the commercial HVFPCs manufactured by TVPSolar.

The use of other low-emissive materials such as copper (emittance $\varepsilon = 0.02$) or silver (emittance $\varepsilon = 0.01$) as substrates is limited by their high cost [74]. However, if utilizing them as bulk substrates is not economically feasible, there is an affordable and convenient alternative: applying a thin film to reduce the substrate emissivity, as illustrated in Figure 2.1.

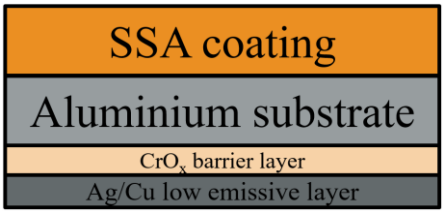

Figure 2.1 Solar absorber with a low emissivity coating on the back side of the aluminum substrate. A titanium bonding layer is used to guarantee the adhesion of the coating.

2.1.1 Materials and architectures of samples with Low Emissivity Coatings (LEC)

To investigate the impact of a Low Emissivity Coating (LEC), we implemented various architectures as shown in Figure 2.2 (the bonding layer of titanium, with a thickness of 10 nm, is not depicted in the figure). For the LEC, we selected silver (Ag) and copper (Cu) as low emissive materials, which were deposited using e-beam vapor deposition onto an aluminum bulk substrate. The LEC was applied on either one side (architectures 1 and 2) or both sides (architectures 3, 4, and 5) of the aluminum substrate, with a thickness of 200 nm for each LEC.

Coatings can be affected by diffusion processes by which atoms or molecules from the coating material migrate or diffuse into the substrate or surrounding environment. The rate of diffusion in coatings is influenced by time and temperature. Higher temperatures generally accelerate diffusion due to increased atomic mobility, while longer exposure times allow for more significant diffusion [75]. Materials like Cr_2O_3 are often chosen as diffusion barriers due to their specific properties and characteristics: Cr_2O_3 exhibits excellent thermal and chemical stability, even at high temperatures; has a high melting point, which allows it to maintain its structural integrity and prevent diffusion even at elevated temperatures; has a low diffusion coefficient; is compatible with many substrate materials commonly used in various industries; it is chemically inert and is relatively abundant and cost-effective compared to some other materials used as diffusion barriers [76].
In Architecture 5, a Cr_2O_3 layer was also introduced between the substrate and the LEC, serving as a diffusion barrier (DB) layer to prevent degradation at high temperatures.

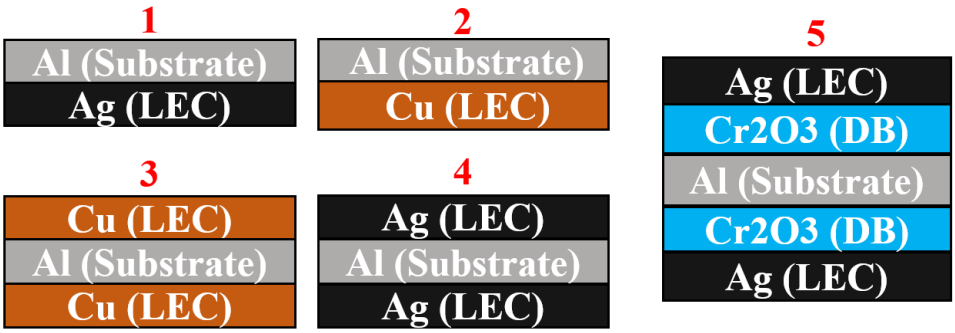

Figure 2.2 Low emissive coating architectures: 1-2) one side LEC Ag and Cu respectively, 3-4) both sides LEC Cu and Ag respectively, 5) both sides Ag LEC with Cr_2O_3 diffusion barrier.

Furthermore, to assess the thermal stability of the LEC, a 200 nm-thick layer of Ag was electron-beam deposited on the backside of a 15x15 cm^2 commercial selective solar absorber (Mirotherm®). This experiment was conducted with and without the presence of a Cr_2O_3 diffusion barrier layer (Figure 2.3). Both samples underwent thermal stress at 360 °C for 24 hours in the MTB apparatus, and measurements of thermal emittance were performed before and after the treatment.

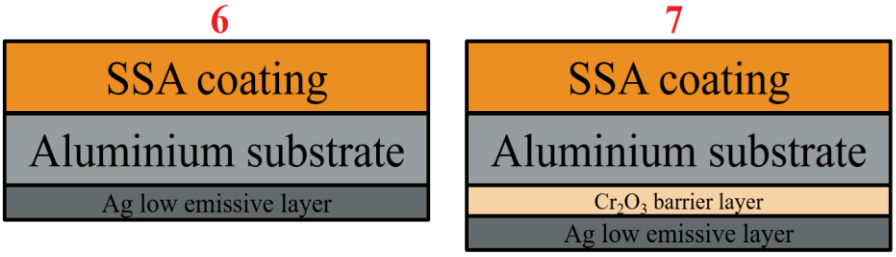

Figure 2.3. Silver LEC on the back side of a commercial Selective Solar Absorber without (6) and with (7) a Cr_2O_3 diffusion barrier layer.

The LECs were deposited on the substrates (samples from Figure 2.2) using the electron-beam vapor deposition technique. The evaporation of Ag, Cu, and Cr_2O_3 was carried out under a vacuum pressure of $4 \cdot 10^{-5}$ Pa, with a deposition rate of 1.5 $Å s^{-1}$, onto aluminum substrates that were cleaned with acetone and isopropyl alcohol. The deposition rate was monitored and controlled using a Quartz Crystal Microbalance (QCM) [77], which was accurately calibrated with the density and Z-ratio values of Ag, Cu, and Cr_2O_3. The QCM deposition rate reading was adjusted to match the deposition rate on the samples through careful calibration of the tooling factor. The tooling factor was determined experimentally by depositing single layers of Ag, Cu, and Cr_2O_3 on reference samples and measuring their thicknesses using a profilometer (KLA Tencor P-15).

Figure 2.4 depicts two samples of aluminum bulk before (a) and after (b) the copper coating.

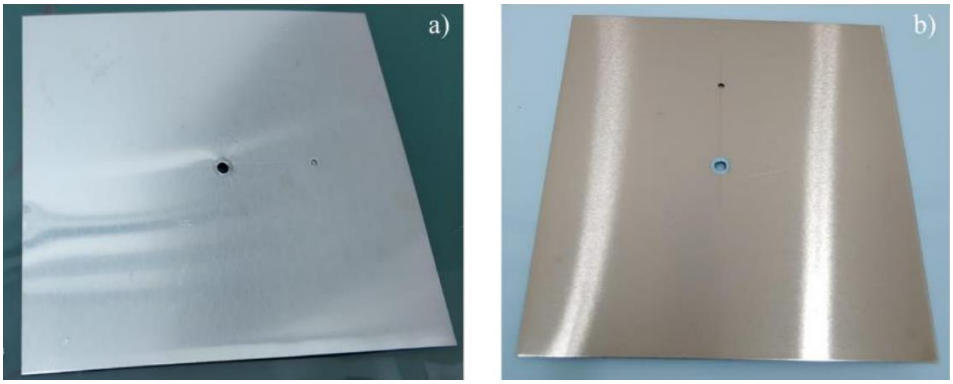

Figure 2.4 Aluminum bulk substrate before (a) and after (b) copper coating via e-beam PVD.

2.1.2 Experimental results: Thermal emittance reduction with LECs and thermal stability

The thermal emittance of the fabricated LEC samples was measured using the MTB apparatus, following the well-described measurement procedure outlined in section 1.4.3. Figure 2.5 presents a comparison of the thermal emittances obtained through calorimetric measurements for a bulk aluminum substrate and the five different architectures depicted in Figure 2.2.

The curves represented refer to the total thermal emittance of both sides of the measured samples. In the case of the bulk aluminum substrate (grey line), the thermal emittance remains almost constant (0.10) across the entire measured temperature range. Notably, this value is exactly double the literature data for aluminum thermal emittance [78]. For the one-side coated samples (architectures 1 and 2), a 25% reduction in thermal emittance is observed, while the double-side Cu coated sample (architecture 3) exhibits a 50% reduction.

The most significant reduction in thermal emittance is achieved with the double-side Ag-coated samples (architectures 4 and 5), displaying a reduction of 60-65%.

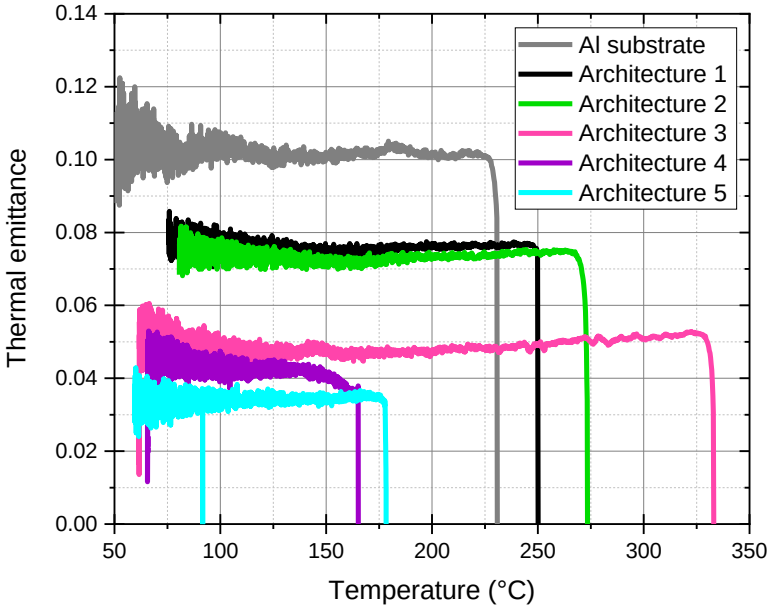

Figure 2.5 Thermal emittances results of calorimetric measurements of the aluminum bulk substrate (grey line) and architectures 1 - 2 - 3 - 4 – 5 (black, green, pink, violet, and cyan respectively).

Figure 2.6 highlights the impact of Ag LEC deposition on the backside of a commercial selective solar absorber (SSA) and the role played by the Cr_2O_3 diffusion barrier (DB) layer in ensuring the thermal stability of the LECs. The thermal emittance of the commercial SSA in its original state, architecture 6 (from Figure 2.3), and architecture 7 (also from Figure 2.3) is depicted by the black, blue, and green lines, respectively. Both samples with the silver LEC exhibit an 11% reduction in thermal emittance at 200 °C compared to the commercial SSA in its original state.

To demonstrate the thermal stability of the LECs, these samples were subjected to thermal stress for 24 hours at 360 °C in a vacuum environment. The thermal emittance after the annealing process is shown in Figure 2.6. The commercial SSA in its original state demonstrates thermal stability, as the thermal emittance after the thermal treatment (red line) remains the same as that of the untested commercial SSA. Architecture 6, on the other hand, exhibits an increase in thermal emittance after the thermal stress compared to the untested one. The emittance reaches the same value as the commercial SSA, thereby losing all the advantages conferred by the LEC. In contrast, architecture 7, after the thermal treatment, maintains the same thermal emittance as the untested architecture 7. This demonstrates the necessity of having a diffusion barrier to preserve the benefits of the LECs.

The reduction of the substrate thermal emittance $\varepsilon_{sub}(T)$ has a significant impact on the overall efficiency of a selective coating for HVFPCs, as defined by Equation 2.1 The equation incorporates various factors, including the substrate thermal emittance, in calculating the SSA efficiency:

$$\eta_{abs} = \alpha_s - \frac{\varepsilon_{abs}(T)\,\sigma_{SB}(T_{abs}^4 - T_{amb}^4)}{C \cdot G_{Sun}} - \frac{\varepsilon_{sub}(T)\,\sigma_{SB}(T_{abs}^4 - T_{amb}^4)}{C \cdot G_{Sun}} \quad (2.1)$$

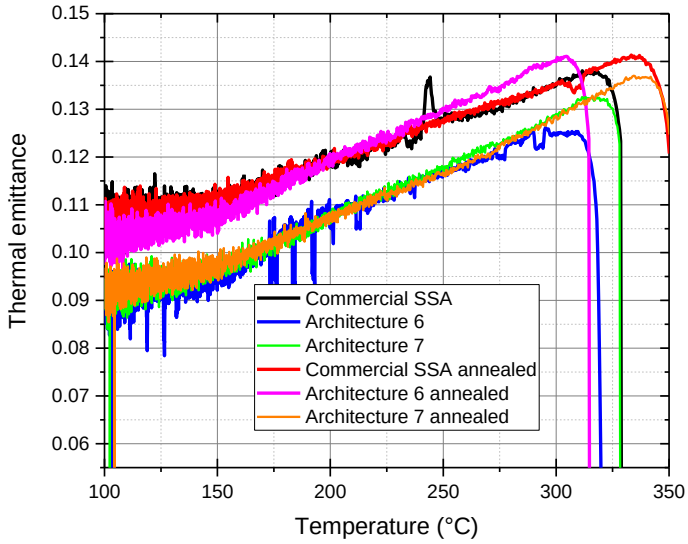

Figure 2.6 Thermal emittance calorimetric measurements of commercial SSA, architecture 6 and 7 before (black, blue, and green line respectively) and after (red, magenta, and orange respectively) thermal treatment.

Where α_s is the spectrally averaged absorptivity of the selective absorber-side coating $\varepsilon_{abs}\ (T)$ is the absorber- side thermal emittance, σ_{SB} ($Wm^{-2}K^{-4}$) is the Stefan-Boltzmann constant, T_{abs} and T_{amb} (k) are the absorbers and ambient temperature respectively, G_{sun} is the Solar irradiation(Wm^{-2}) while C is the collector concentration factor.

The effects of an LEC on the absorber efficiency are depicted in Figure 2.7. The figure compares the overall efficiency of an optimized selective coating on an aluminum substrate without a diffusion barrier and LEC (black line) and with a diffusion barrier and LEC (red line).

At 200 °C, the efficiency of the absorber increases from 0.64 to 0.72 with the presence of the LEC, resulting in a 13% enhancement in performance. Additionally, the stagnation temperature increases by approximately 30 °C. Notably, the advantages of the LEC become more pronounced as the temperature rises. At 300 °C, the overall efficiency increases from 0.19 to 0.37, representing an almost doubling of the performance enhancement. Employing a low emissive coating on the coating side of the absorber as well is an approach that allows for the use of cost-effective materials such as aluminum for the substrate while ensuring excellent optical properties of the absorber through the incorporation of low emissive but relatively expensive coatings.

However, at high temperatures, interdiffusion between the low emissive thin film and the aluminum substrate can lead to adhesion issues and a deterioration of the optical properties. To mitigate these diffusion phenomena, an interdiffusion barrier should be employed to limit the diffusion process.

In summary, the use of a low emissive coating, along with a diffusion barrier, can significantly enhance the overall efficiency and optical properties of a selective coating for HVFPCs.

By employing low emissive coatings on both sides of the absorber, the benefits can be maximized while using cost-effective substrate materials such as aluminum. The employment of an interdiffusion barrier becomes crucial at high temperatures to prevent diffusion-related issues and maintain the performance of the coating.

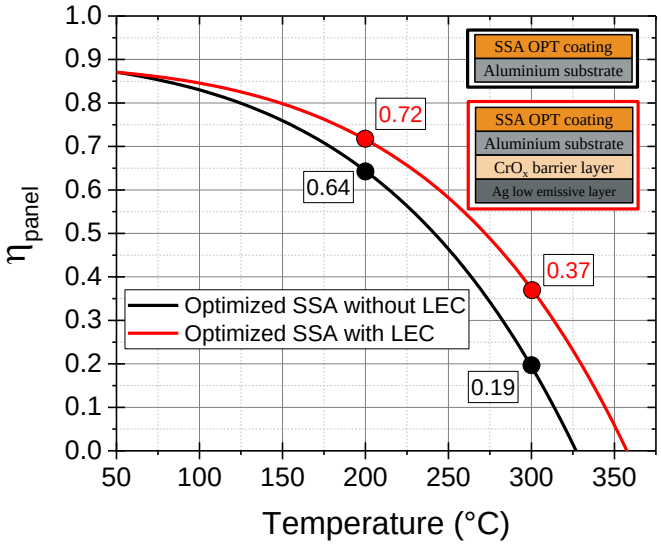

Figure 2.7 Overall efficiency of an optimized selective coating on aluminum substrate without (black line) and with diffusion barrier and low emissive coating (red line).

2.2 MULTILAYER SSA Cr_2O_3/Cr BASED: OPTIMIZATION VIA CUSTOM ALGORITHM.

The development of optimized selective solar absorber (SSA) coatings suitable for HVFPCs began with the formulation of a novel optimization method. This method is based on the efficiency of the actual coating, which serves as the fitness function for the optimization algorithm. By utilizing this approach, the optimization algorithm can identify the optimal balance between solar absorptance and thermal emittance, which is closely tied to the reflectivity spectrum $\rho(\lambda)$ of the coating. This method is particularly well-suited for the emerging technology of HVFPCs, as they can achieve high operating temperatures without the need for concentration, making thermal emittance increasingly important in addition to solar absorptance [36].

One limitation of multilayer selective coatings is that their performance heavily relies on the multiple reflections occurring at the interfaces between the layers in the stack. Consequently, the performance of these solar absorbers is significantly influenced by the thickness of the individual layers. Considering the goal of industrial mass production of these SSAs, it is crucial to acknowledge that perfect control over the deposition parameters may not be achievable, leading to errors in layer

thickness and subsequently affecting the coating's performance. Therefore, it becomes pertinent to introduce a new parameter, namely, the robustness of the coating's performance in the presence of unforeseen errors in layer thickness, during the design stage.

Incorporating this new factor into the optimization process of a selective coating provides the opportunity to select not only the absolute maximum solution, which represents the coating with the highest performance among the range of potential solutions but also the coating that exhibits the highest performance while ensuring adequate robustness against deviations in layer thickness.

2.2.1 Materials and structure of Cr_20_3 optimized SSAs.

The optimized multilayer selective solar absorber (SSA) structure was composed of specific materials to achieve the desired performance. Cr_2O_3 and Cr were chosen as the dielectric and high-absorption metallic layers, respectively. Copper was selected as the low-emissive metallic substrate, and a thin film of SiO_2 served as the antireflective coating.

To ensure that the radiative properties of the solar absorber were not influenced by surface roughness, a low-emissive substrate was deposited onto a smooth glass substrate. This involved the deposition of an optically thick copper layer (250 nm) using e-beam vapor deposition [60] followed by exposure to atmospheric air.

Figure 2.8 illustrates the architecture of the multilayer coating. The five-layer structure consisted of a chromium layer directly deposited on the copper substrate, serving as a bonding layer and preventing the formation of emissive copper oxides during reactive sputtering deposition. This chromium layer was also incorporated into the optimization process, allowing it to be considered as part of the absorbing package.

Once the architecture of the optimized absorber is determined, the materials composing the multilayer structure need to be optically characterized and then the optimization algorithm comes into play to determine the optimal thickness of the various layers that make up the multilayer selective solar absorber.

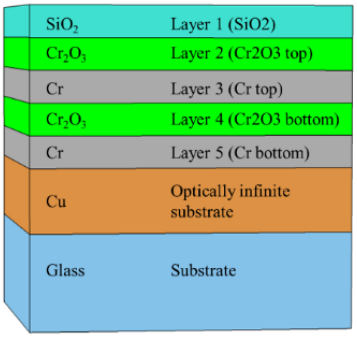

Fig. 2.8 Architecture used for the multilayer coating.

2.2.2 Optical characterization of the multilayer SSA structure

The refractive indices of the materials used in the multilayer absorber are essential inputs for the optimization algorithm. These indices were determined experimentally through ellipsometric measurements. The thin films of Cr and Cr_2O_3 were deposited using DC Magnetron Sputtering (DCMS) and DC Reactive Magnetron Sputtering (DCRMS) processes, respectively, with a 99.99% pure Cr cathode. The multilayer structure of Cr_2O_3/Cr/Cr_2O_3 was completed with a SiO_2 thin film serving as an Anti-Reflective Coating (ARC), which was deposited using RF magnetron sputtering (RFMS) in an argon atmosphere. The deposition conditions for each layer can be found in [79].

To ensure consistent and reliable results, the analyzed layers were deposited on a distinct substrate consisting of an aluminum film grown on a glass support, providing an optically flat surface. The film's thickness and complex refractive index (ñ) were determined by fitting the experimental data to numerical data generated by an optical model that describes the material dispersions using appropriate dispersion formulas. The Forouhi-Bloomer formula was employed for chromium oxide [80],[81], while the Drude-Lorentz dispersion relation was used for chromium [82].

Figure 2.9 (a) and (b) depict the refractive index dispersion for both chromium and chromium oxide, which best fit the experimental data obtained through ellipsometric measurements and were subsequently employed for the optical simulations.

The refractive index of the pure Cr layer (Figure 2.9 (a)) exhibits typical metallic characteristics, with the real (n) and imaginary (k) indices increasing with wavelength. The positive value of k across the entire wavelength range indicates that the Cr layer primarily absorbs light. Conversely, the real and imaginary parts of the refractive index for Cr_2O_3 (Figure 2.9 (b)) decrease with increasing wavelength, signifying a dielectric behavior. The k index approaches zero in the visible region, indicating the film's transparency at longer wavelengths. These refractive indices were determined by fitting experimental data from multiple samples and were found to be valid for Cr_2O_3 film thicknesses ranging from 15 nm to 100 nm and Cr layer thicknesses ranging from 5 nm to 30 nm. Surface roughness effects were mitigated by employing optically smooth surfaces in the models.

Since ellipsometric analysis is limited to the range between 300 nm and 1600 nm, the refractive indices of both chromium and chromium oxide were extended beyond the measured wavelength range using the corresponding dispersion relations. The results demonstrate good agreement with the literature data [83],[84],[85]. The effectiveness of the obtained refractive indices was further validated through reflection measurements. Figure 2.9 (c) presents a comparison between the measured and simulated reflection of a Cr_2O_3/Cr bilayer on an aluminum substrate, with the model and layer thicknesses displayed in the inset. Reflectance was measured using an integrating sphere coupled with an Optical Spectrum Analyzer (OSA) in the visible and near-infrared range (0.35-1.75 μm),

while Fourier Transform Infrared Spectroscopy (FTIR) was employed for reflectance measurements in the range of 1.00-4.00 µm. The two measurement techniques overlapped in the 1.00-1.75 µm range, indicating good agreement between them. The optical simulation of the sample utilized the refractive indices presented in Figure 2.2, along with literature data for Al_2O_3 and the aluminum substrate [43],[83],[86]. The agreement between the optical simulation and the reflectance measurements confirms the reliability of the investigated refractive indices for both chromium and chromium oxide across the entire wavelength range.

2.2.3 Genetic Algorithm for SSAs Coating Optimization

The optimization of the selective solar absorber (SSA) coatings was performed using a Genetic Algorithm (GA) to maximize the absorber efficiency. The fitness function used in the optimization process was the absorber efficiency, defined by equation (2.2)

$$\eta_{coat}(T_m) = \frac{q_h}{G} = \alpha_S - \frac{\varepsilon(T_h)\sigma_{SB}\left(T_m^4 - T_{amb}^4\right)}{G} \qquad (2.2)$$

where q_h (Wm^{-2}) is the heat flux to the thermal system, T_m (K) is the absorber temperature, T_{amb} (K) is the environmental temperature, G (Wm^{-2}) is the sun-irradiated power, and σ_{SB} ($Wm^{-2}K^{-4}$) is the Stefan-Boltzmann constant.

To optimize the SSA, the algorithm calculates the reflectance ρ(λ) of the stack at each wavelength, which allows the evaluation of the solar absorptance α_S and thermal emittance ε(T) using eqs. (1.7) and (1.8) respectively.

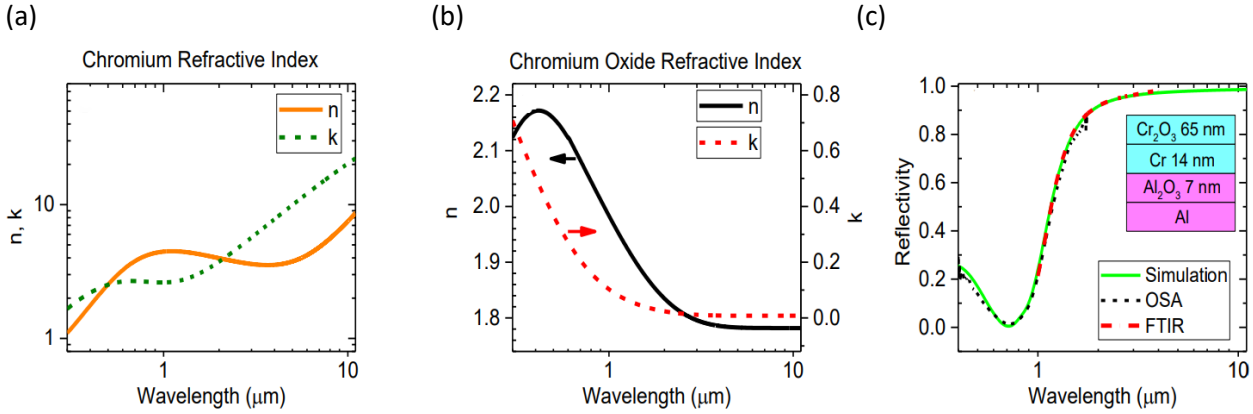

Figure 2.9 Refractive index and extinction coefficient obtained by fitting ellipsometric measurements for Chromium (a) and Chromium Oxide (b). (c) The agreement between experimental data and simulation obtained using the reported refractive indices is shown in simulation (green, solid line), Optical Spectrum Analyzer (OSA) (black, dash line), Fourier Transform Infrared Spectroscopy (FTIR) (red, dash-dot line).

The algorithm automatically adjusts the thickness of each layer and calculates the emissivity ε(λ) of the coating at each wavelength using the transfer matrix method [87] and the refractive indices of the materials described in section 2.2.2.

The GA is a search-based method commonly used for solving optimization problems, especially when classical optimization algorithms are not well suited due to discontinuous, nondifferentiable, stochastic, or highly nonlinear objective functions. In this application, the GA is advantageous because it can explore a large number of potential solutions (thickness combinations) and search the solution space efficiently. It is a global random search algorithm, which makes it less likely to get stuck in local minima. Additionally, the GA is independent of the initial conditions, although the search space needs to be defined.

To ensure robustness in the optimization process, a constraint was introduced to limit the loss in efficiency due to errors in layer thickness. Specifically, the maximum acceptable loss in efficiency was set to 2 percentage points for errors within a 20% range of the layer thicknesses. Any solutions that did not meet this constraint were rejected, and the algorithm only returned thickness combinations that satisfied the constraints. This range was chosen to account for potential variations due to factors such as manufacturing tolerances and thermal expansion effects.

By analyzing the efficiency of the multilayer stack for the optimized solution, considering these thickness variations, the maximum change in efficiency remained within 2%. This indicates that even with small deviations in layer thicknesses, the overall performance of the selective solar absorber is largely preserved. Furthermore, it is important to note that the consideration of thermal expansion effects is crucial in ensuring the long-term stability and performance of the multilayer stack. As temperature increases, the layers may undergo expansion, potentially deviating from their optimized thickness values. By incorporating a ±20% thickness variation range, which accounts for thermal expansion, the optimized solution effectively addresses this issue and minimizes any adverse effects on the reflectivity curve and overall efficiency.

2.2.4 Optimization results

The Genetic Algorithm (GA) was employed to design two optimized selective solar absorber (SSA) coatings for operating temperatures of 200 °C and 300 °C, referred to as OPT_{200} and OPT_{300}, respectively. The simulation yielded the optimal thickness combinations of layers for each optimized absorber, and the optical properties of the optimized absorbers were compared with those of the commercial absorber (Mirotherm ©) listed in Table 2.1. The table includes the thickness combinations, solar absorptance values, and thermal emittance values.

Tab. 2.1. Optimal thickness combinations, solar absorptance α_S values, and thermal emittance ε (T) for commercial coatings and OPT_200 and OPT_300.

Sample	T opt. (°C)	Layer thick. (Layer 1 to 5) (nm)	α_S	ε (100 °C)	ε (200 °C)	ε (300 °C)
Commercial	-	-	0.945	0.062	0.070	0.081
OPT_{200}	200	72-55-10-27-15	0.936	0.026	0.031	0.040
OPT_{300}	300	65-45-8-14-10	0.889	0.017	0.020	0.025

Figure 2.10 (a) presents the spectral reflectivity of the three coatings along with the normalized solar spectrum. As the target working temperature increases, the cut-off wavelength ($\lambda_{Cut\text{-}Off}$) shifts towards shorter wavelengths. This behavior is attributed to the blackbody emission peak shifting towards shorter wavelengths, which is a well-known characteristic of an ideal selective solar absorber. Figure 2.10 (b) displays the thermal emittance of the three coatings as a function of absorber temperature. The coating optimized for a higher working temperature (300 °C) exhibits a reduction in thermal emittance of approximately 70% compared to the commercial coating. This reduction in thermal emittance, which minimizes radiative losses, comes at the expense of a 6% reduction in solar absorptance (see Table 2.1).

(a) (b)

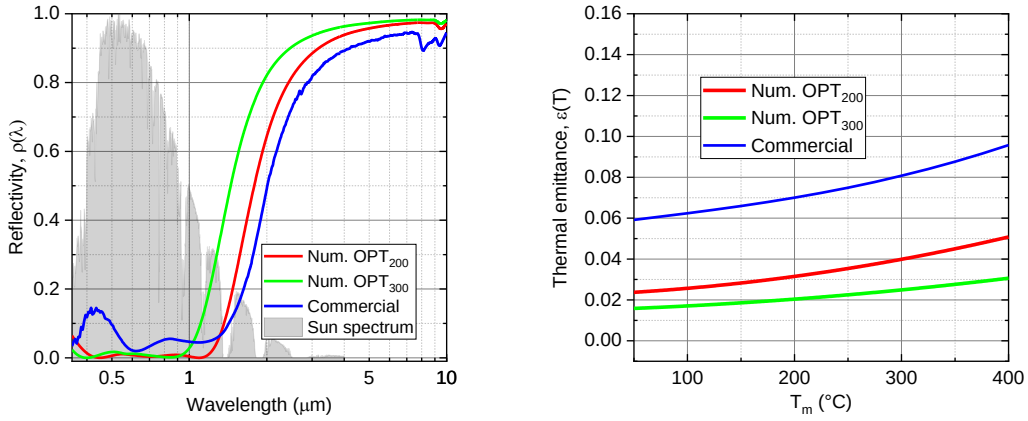

Fig. 2.10 Optical simulations. (a) Spectral reflectivity of two coatings optimized for a target temperature of 200, and 300 °C (red, and green curve, respectively) and of the commercial coating (blue line). Normalized sun spectrum, grey-filled area. (b) Temperature-dependent thermal emittance of two coatings optimized for a target temperature of 200, and 300 °C (red, and green curve, respectively) and of the commercial coating (blue line).

Figure 2.11 illustrates the coating efficiency (Eq. (2.2)) of the simulated multilayer for an incident power of 1000 Wm^{-2}. The optimization process ensures the highest efficiency at the specified temperature for each case. The efficiency curve clearly demonstrates how the trade-off between absorptance reduction and low thermal emittance leads to lower radiation losses. Consequently, this results in lower efficiency at low temperatures but facilitates the maintenance of higher efficiencies at higher working temperatures.

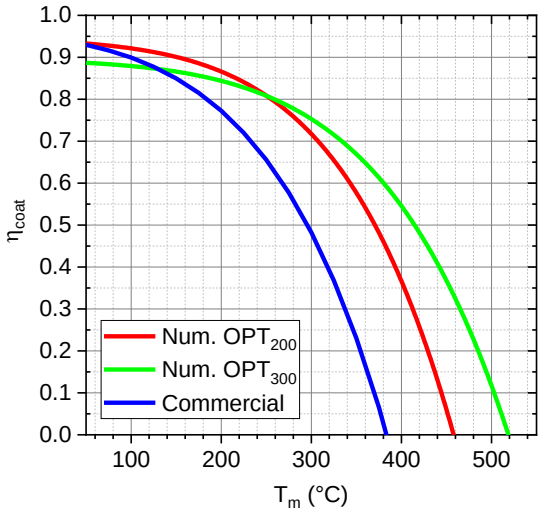

Figure 2.11 Optical simulations of coating efficiency η_{coat} of two coatings optimised for a target temperature of 200, 300 °C (OPT_{200}, OPT_{300}; red, green curve, respectively) and of the commercial coating (blue line).

To assess the robustness of the solution concerning thickness variations, the efficiencies of the multilayer stack for different thickness combinations were considered. Each layer's thickness was varied around its optimal value, with a maximum percentage error of ±20%. The figure only displays the extreme values (+20% and -20%) along with the optimal thickness values to simplify the representation. This results in three possible thickness values for each layer, leading to a total of 243 combinations or multilayer stacks.

Figure 2.12(a) provides an overview of the relationship between thickness variation and its effect on coating efficiency at the target optimization temperature. The coatings show remarkable stability, with the efficiency difference remaining below or equal to 2 percentage points for all possible combinations. The graph demonstrates that the OPT_{200} coating exhibits smoother efficiency variation with thickness combinations compared to the OPT_{300} coating. This can be attributed to the chromium bottom layer, which reaches a thickness of 70 nm in the coating optimized at 200 °C.

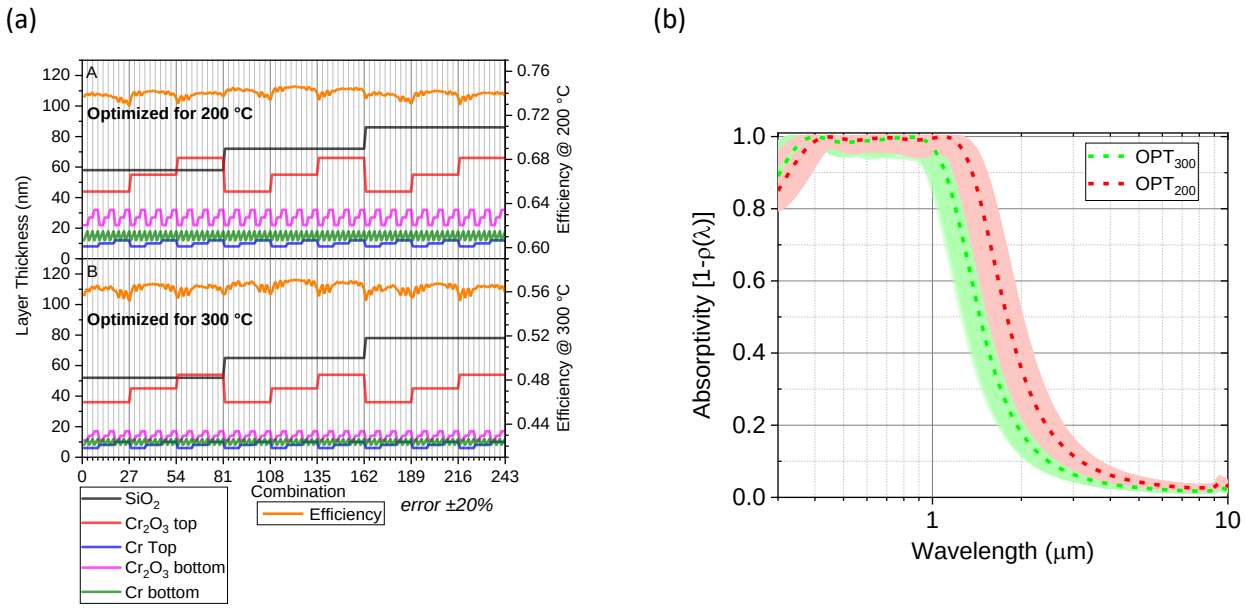

Fig. 2.12 (a): Coatings OPT_{200}, OPT_{300} (panel A, B respectively). x-axis: each with combination identifies a different stack in terms of thickness, obtained by varying the thickness of each layer around its optimal value, in the case of three possible values for each layer and error=±20%. Left y-axis: thickness value of each layer in nanometres for the i^{th} combination. Right y-axis: efficiency evaluated at the target optimization temperature related to the i^{th} combination.

(b): Spectral emissivity 1- ρ(λ) for the coatings OPT_{200} and OPT_{300}. Dash curves: optimal thickness stack. Solid line curves light color: emissivity curves obtained by varying the thickness of each layer around its optimal value, in the case of three possible values for each layer and error = ± 20%.

In Figure 2.13, the solar absorptance α_S (purple, left y-axis) and the efficiency and thermal emittance ε(T) at the target optimization temperature are shown for each combination of the two optimized coatings (panels A and B). The data is derived from the spectral emissivity curves 1-ρ(λ) in Figure 2.12 (b). The figure highlights the relative importance of solar absorptance α_S and thermal emittance ε(T) in determining the efficiency at different working temperatures. For the coatings optimized at 200 and 300 °C, both the solar absorptance and thermal emittance decrease overall, with an increased variation in α_S and a decrease in ε(T). The variation in α_S has a limited impact on solar absorber efficiency, whereas variations in thermal emittance are more influential. The analysis of the OPT_{200} and OPT_{300} coatings emphasizes the importance of thermal emittance in determining solar absorptance with increasing temperature, underscoring the need to consider the relative significance of α_S and ε(T) at different working temperatures. The optimization algorithm automatically adjusts the layer thickness to control α_S and ε(T) based on the target working temperature, ensuring optimal performance and robustness in the face of thickness errors during the deposition stage.

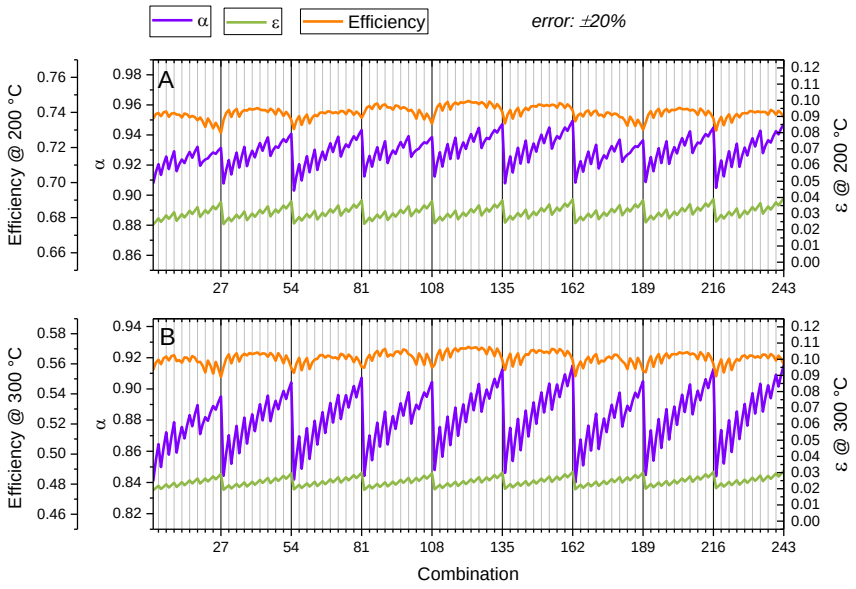

Fig. 2.13 Axis x: each with combination identifies a different multilayer stack in terms of thickness, obtained by varying the thickness of each layer around its optimal value, in the case of three possible values for each layer and error = ± 20%. Axis y: solar absorptance α_S (left y-axis, purple), efficiency (left y-axis, orange), and thermal emittance $\varepsilon(T)$ (right y-axis) for the ith combination at the target optimization temperature, for the coatings OPT_{200} and OPT_{300} (panel A and B respectively).

2.2.5 Experimental validation of simulation results

To validate the numerical simulations and the optimization process, coatings OPT_{200} and OPT_{300} were experimentally fabricated using sputtering deposition. The thickness of the multilayer was measured using a profilometer (KLA Tencor P-15), and the measured thickness agreed with the sum of the expected thicknesses of the individual layers.

Figures 2.14 (a) and (b) display the measured reflectance spectrum and the corresponding thermal emittance of the deposited samples, compared with the simulated reflection spectra.

The solar absorptance values (α) and thermal emittance at different temperatures, along with their numerical counterparts for the two coatings, are listed in Tab. 2.2. The measured samples closely match the simulated results, confirming the accurate evaluation of the experimental refractive indices used in the optimization process. The presented data were calculated for normal incident radiation, and when considering angular dependence, the absorptance and emittance may differ. However, the absorptance reported in Tab. 2.2 was measured using an integrating sphere and exhibits only a slight deviation from the normal incident value, indicating a small angular dependence. The emittance values were measured using an FTIR specular reflectance accessory, and the hemispherical emittance may be slightly higher than the reported value, which requires further investigation.

(a) (b)

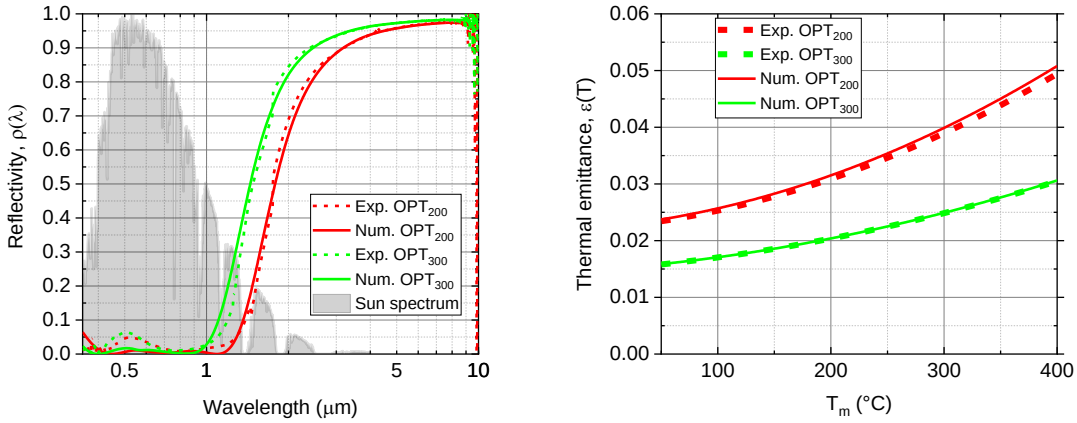

Fig. 2.14 (a) Measured reflectance spectrum of the deposited samples OPT_{200}, and OPT_{300} (red, green dash lines) in comparison with the simulated reflection spectra (red, green solid lines). Normalized sun spectrum, grey-filled area. (b) Thermal emittance of the deposited samples OPT_{200}, and OPT_{300} (red, green dash lines) in comparison with the simulated thermal emittance (red, green solid lines).

Table 2.2. Solar absorptance values α and thermal emittance at different temperatures in comparison with the numerical counterparts for the two coatings

Sample	**T opt. (°C)**	**$\alpha_{Num.}$**	**$\alpha_{Exp.}$**	**$\varepsilon_{Num.}$ (100 °C)**	**$\varepsilon_{Exp.}$ (100°C)**	**$\varepsilon_{Num.}$ (200°C)**	**$\varepsilon_{Exp.}$ (200°C)**	**$\varepsilon_{Num.}$ (300°C)**	**$\varepsilon_{Exp.}$ (300°C)**
OPT_{200}	200	0.936	0.925	0.026	0.025	0.031	0.031	0.040	0.039
OPT_{300}	300	0.889	0.890	0.017	0.017	0.020	0.020	0.025	0.025

Table 2.3 provides the coating efficiency (Eq. (2.2)) at the target optimization temperature for the three proposed selective absorbers, along with the corresponding percentage deviation and the difference $\Delta\eta$coat. Despite the variations in α_S and $\varepsilon(T)$, $|\Delta\eta coat| \leq 0.02$ is still ensured, by the constraints imposed during the optimization process.

Table 2.3. Coating efficiency η_{coat} at the target optimization temperature for the two proposed selective absorbers, related percentage deviation, and the difference $\Delta\eta_{coat}$

Sample	**T opt. (°C)**	**$\eta_{coat\ Num.}$**	**$\eta_{coat\ Exp.}$**	**Deviation %**	**$\Delta\eta_{coat.}$**
OPT_{200}	**200**	0.866	0.847	2.2	0.02
OPT_{300}	**300**	0.753	0.746	1.0	0.01

The estimation of the coating efficiency for the experimental coating was conducted.

Fig. 2.15 presents the coating efficiency calculated at 1000 W/m^2 using the experimental emissivity curves, which are then compared with the efficiency calculated under the same conditions using the emissivity curve obtained from the optical simulations.

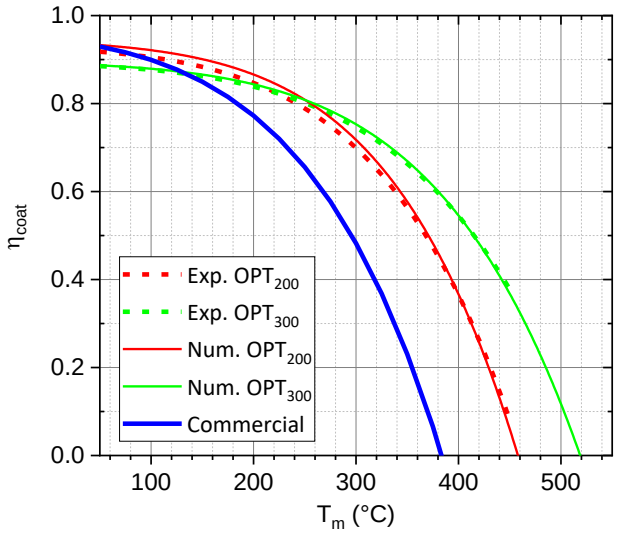

Figure 2.15 Coating efficiency of the experimental samples OPT$_{200}$, OPT$_{300}$ (red, green dash lines) in comparison with the optical simulations (red, green solid lines) and of the commercial coating (blue line).

The figure demonstrates a remarkable agreement between the experimentally realized coatings and their simulated counterparts, confirming the feasibility of the coatings and their suitability for application in the medium-temperature range.

Furthermore, when comparing the efficiency of the optimized coatings with that of the commercial coating, an improvement of 7.4% is observed at 200 °C for both coatings. At 300 °C, the improvement is even more significant, with OPT$_{200}$ showing an increase of 21.6% and OPT$_{300}$ demonstrating a remarkable improvement of 26.3%.

2.3 TOTAL EMISSIVITY MEASUREMENTS PROCEDURE FOR CHARACTERIZATION OF LOW-EMISSIVE MATERIALS FOR SOLAR THERMAL CONVERSION APPLICATIONS

To develop SSAs with excellent optical properties, reliable and precise measurements of emissivity are necessary. However, accurately determining the emissivity of coatings can be challenging due to the influence on the measurements of optical properties, surface roughness [88],[89],[90] and composition [91],[92]. Additionally, environmental conditions, such as temperature and humidity, may also affect the accuracy of emissivity measurements [93],[94],[95].

Several methods are commonly used to measure the emissivity of coatings, including spectroscopic methods, such as infrared reflectometry and Fourier-transform infrared spectroscopy (FTIR) [96], as

well as calorimetric methods [97], such as the heat flux meter [98] or radiometric measurements [99]. Each method has its advantages and limitations, and the choice of technique depends on the specific requirements of the measurement and the properties of the coating being evaluated.

The calorimetric technique provides valuable insights into the coating's radiative properties, measuring the heat flux emitted by the coating under controlled conditions. These measurements involve subjecting the coating to varying temperatures and analyzing the resulting heat transfer.

In the context of Selective Solar Absorbers (SSAs) used in High Vacuum Flat Plate Collectors (HVFPCs) [79], the total hemispherical emissivity [100], [101], measurement method using a calorimetric technique is described in [61].

This method utilizes the specialized test equipment Mini Test Box (MTB), described in section 1.4.3. The Previous work has successfully applied the MTB apparatus to measure the total hemispherical emissivity of selective absorbers with an Aluminum substrate and a surface area of 210 cm^2 (maximum sample dimension containable in the MTB chamber) [61]. However, when dealing with SSAs having substrates with lower emissivity or smaller dimensions, the emissivity measurement procedure needs improvement to minimize measurement errors.

This paragraph addresses the correction of the emissivity measurement procedure using the MTB apparatus specifically for measuring the emissivity of SSAs with low-emissive substrates and different dimensions. The following sections will provide a detailed account of the improved measurement procedure and its implications for accurate emissivity characterization.

2.3.1 Influence of sample dimensions on thermal emittance measurements of low-emissivity Cu-Bulk samples using the MTB Apparatus.

Going back to section 1.4.3, we explained that the principle of the calorimetric MTB measurements procedure involves obtaining a calorimetric measurement of thermal emittance by monitoring the instantaneous temperature variation of an absorber sample, during the cooling phase after being heated until stagnation temperature by the LED system's irradiated power. The temperatures of the cover glass and chamber walls are measured using K-type thermocouples. An additional thermocouple is crimped to a lug and screwed to the central hole of the sample using an M3 stainless steel bolt.

We can rewrite the calorimetric balance equation during the cooling phase by considering the contribution of the thermocouple bolt:

$$\left[m_{abs}c_{pabs}(T_{abs}) + m_{th}c_{pth}(T_{abs})\right]\frac{dT_{abs}}{dt} = -A_{abs}\left[\varepsilon_{abs}(T_{abs})\sigma_{SB}\left(T_{abs}^4 - T_g^4\right) + \varepsilon_{sub}(T_{abs})\sigma_{SB}(T_{abs}^4 - T_{vess}^4)\right] \quad (2.3)$$

where m_{abs}, A_{abs} and $c_{pabs}(T_{abs})$ are the mass, the surface and the temperature-dependent heat capacity of the absorber sample, m_{th} and $c_{pth}(T_{abs})$ are the mass and the temperature-dependent capacity of the absorber thermocouple fastening bolt and nut, T_{abs}, T_g, and T_{vess} (K) are the absorber, glass, and bottom of the MTB vacuum chamber temperatures, respectively.

A simplification is possible by considering the emission towards an ideal surface with an average temperature between the glass and the base of the vacuum chamber (T_{box}). This simplification is possible because it was observed that during the measurements the difference between T_g and T_{vess} never exceeds 10 K. The equation (2.3) becomes equation (2.4):

$$\left[m_{abs}c_{pabs}(T_{abs}) + m_{th}c_{pth}(T_{abs})\right]\frac{dT_{abs}}{dt} = -\varepsilon_{sample}(T_{abs})A_{abs}\sigma_{SB}(T_{abs}^4 - T_{box}^4) \qquad (2.4)$$

where ε_{sample} represents the sum of ε_{abs} and ε_{sub}.

When formulating the balance equation (2.4), only the sample emitted radiation is considered during the cooling phase, and other heat exchange mechanisms occurring during the cooling phase of the sample are disregarded. This is justified by the findings presented in [61], which demonstrate that these mechanisms can be considered effectively negligible for samples with a surface area of 210 cm^2 and emissivity values exceeding 0.08.

Emissivity measurements conducted on Cu-bulk samples of various dimensions using the MTB apparatus, demonstrated that for low-emissive and small samples, it is necessary to consider other thermal loss mechanisms during the cooling phase of the samples.

During the measurements, the sample is positioned within the vacuum chamber and supported by two steel supports. These supports are in direct thermal contact with the sample, introducing an additional conductive factor that influences the cooling process. Furthermore, the thermocouple used to measure the sample's temperature variations is attached to a lug and secured to the central hole of the sample using an M3 stainless steel bolt. Although the exposed surface area of the bolt was much smaller than that of the larger samples (210 cm^2), it played a significant role in conductive heat transfer and irradiation for low-emissive or smaller samples.

These additional mechanisms of heat exchange, often overlooked in the calorimetric balance equation, become increasingly significant in the computation of cooling power $\left(\left[m_{abs}c_{pabs}(T_{abs}) + m_{th}c_{pth}(T_{abs})\right]\frac{dT_{abs}}{dt}\right)$ and, consequently, in the measurement of emissivity. This is particularly true as the measured sample's area and emissivity decrease, such in the case of Copper (Cu) samples. Figure 2.16 presents the results of the calorimetric thermal emittance measurements (emittance of both sample faces) conducted on bulk copper (Cu) samples of various dimensions (210 cm^2, 100 cm^2, 64 cm^2, and 49 cm^2), obtained by solving the calorimetric balance equation (2.4).

(a) (b)

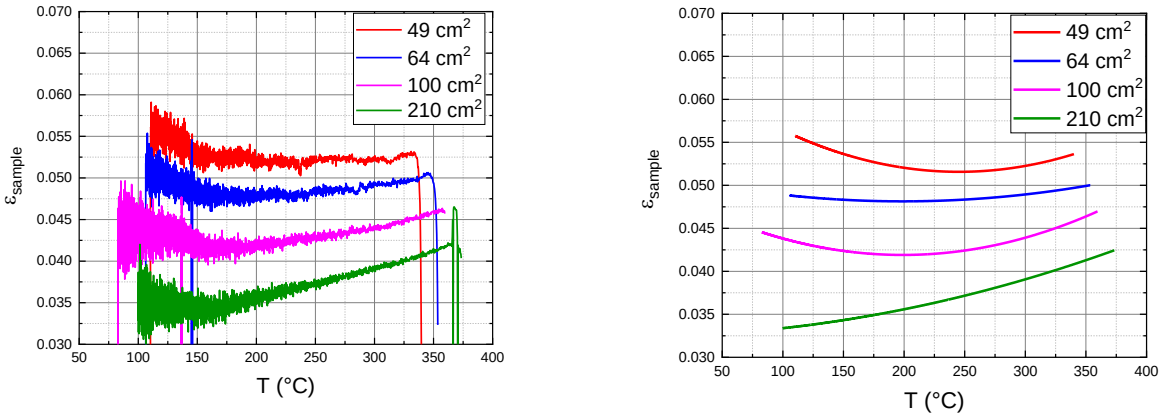

Figure 2.16 (a): Measured thermal emittance of different dimensions copper samples as a function of the absorber temperature; (b): Moving average of the measured thermal emittance of different dimensions copper samples as a function of the absorber temperature.

It is evident that as the sample dimensions decrease, the influence of the previously mentioned additional heat exchange mechanisms becomes more significant, leading to an overestimation of the emissivity of the copper samples. Even though all the analyzed samples are made of the same materials, there is a difference of at least 40% in the measured emittances between the smaller and larger samples (as shown in Figure 2.16).

2.3.2 Calorimetric balance equation for low-emissive SSAs and evaluation of the additional heat losses term (Other Thermal Losses function)

To measure the thermal emittance of low-emissive and/or small samples, the calorimetric equation (2.4) must be rewritten as follows:

$$\left[m_{abs}c_{pabs}(T_{abs}) + m_{th}c_{pth}(T_{abs})\right]\frac{dT_{abs}}{dt} = -\varepsilon_{sample}(T_{abs})\sigma_{SB}A_{abs}(T_{abs}^4 - T_{box}^4) - \mathbf{OTL}\ (T_{abs}, T_{box}) \quad (2.5)$$

The term OTL (T_{abs}, T_{box}) stands for Other Thermal Losses and represents the fraction of the cooling power exchanged due to the additional heat transfer mechanisms mentioned above.

Considering that parameters m_{abs}, m_{th} and A_{abs} can be easily measured, and that σ_{SB} is a constant, along with the knowledge of the sample material and the $c_{pabs}(T)$ and $c_{pth}(T)$ known function, the sensors installed in the experimental apparatus MTB enable the resolution of the calorimetric equation (2.4) with a single measurement because the only unknown term in the equation is the total effective emittance of the sample: $\varepsilon_{sample}(T_{abs})$.

With the insertion of the OTL term in the thermal balance, is necessary to obtain the additional thermal losses function to solve the calorimetric equation (2.5) with a single measurement.
To obtain the sample emissivity the methodology adopted involves the resolution of a system of two equations with two unknowns:

$$\begin{cases} \left[m_{abs1}c_{pabs}(T_{abs}) + m_{th}c_{pth}(T_{abs})\right]\frac{dT_{abs}}{dt} = -\varepsilon_{sample}(T_{abs})\sigma_{SB}A_{abs\_1}(T_{abs}^4 - T_{box}^4) - \mathbf{OTL}\,(T_{abs}, T_{box}) \\ \left[m_{abs2}c_{pabs}(T_{abs}) + m_{th}c_{pth}(T_{abs})\right]\frac{dT_{abs}}{dt} = -\varepsilon_{sample}(T_{abs})\sigma_{SB}A_{abs_2}(T_{abs}^4 - T_{box}^4) - \mathbf{OTL}\,(T_{abs}, T_{box}) \end{cases} \quad (2.6)$$

The term OTL(T_{abs}), depends not only on the elements present in the experimental setup (such as steel supports, thermocouple lug, and bolt) but also on the material properties of the sample under analysis, specifically its conductivity.
Section 2.3.1 shows the results of calorimetric measurements conducted on four bulk copper samples of different dimensions (210 cm^2,100 cm^2, 64 $cm^{2,}$ and 49 cm^2) using the MTB apparatus. For each pair of samples made of the same material, in correspondence with the same absorber sample and box temperatures (T_{abs}, T_{box}), the equality of the terms $\varepsilon_{\mathbf{sample}}$ and OTL ($T_{abs,}$ T_{box}) was enforced during the resolution of the equation system (2.6). For the 4 samples of different dimensions (n=4) to analyze we have 6 simple combinations with 2 elements (k=2):

$$C_{n,k} = \frac{n!}{k!(n-k)!} \quad (2.7)$$

Solving for the 6 different combinations of the system (2.7), 6 different OTL ($T_{abs,}$ T_{box}) curves were obtained, and the mean curve was considered to design the function that must be added in the new calorimetric balance equation (2.5) to correct the emissivity values of absorber with copper (Cu) substrate.
In Figure 2.17, the six curves of the Other Thermal Losses (OTL) are displayed as a function of absorber sample temperature. For each observed case the trend of temperature T_{box} concerning the absorber sample temperature T_{abs} experience negligible variations during the measurements of samples of different dimensions. In the legend of the graph, each curve is indicated with the dimensions (in cm^2) of the pair of samples whose balance equation is coupled in the system (2.6). The average of the six curves represents the result of the OTL function for the copper samples. By extrapolating the average OTL curve, we can extend the temperature range of applicability for the obtained OTL function. From the experimental data obtained, is possible to write a mathematical expression of the OTL term.
In general, the OTL function to consider in the calorimetric balance equation, consists of a radiative term, proportional, according to the Stefan-Boltzmann law, to the difference of the fourth power of the absorber and box temperatures, and a conductive term, proportional to the difference of the absorber and box temperatures.

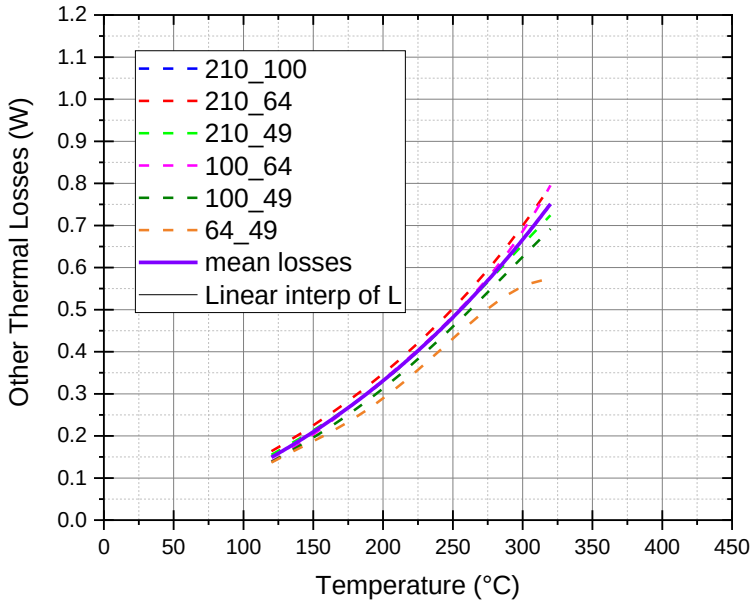

Figure 2.17 Representation of OTL curves in function of the sample temperature obtained for each pair of different dimensions copper samples analyzed (201, 100,64, and 49 cm^2). The graph also represents the mean losses curve and its linear extrapolation.

The expression of OTL ($T_{abs,}$ T_{box}) assumes the following form:

$$OTL(T_{abs,}T_{box}) = z_1 * (T_{abs}^4 - T_{box}^4) + z_2 * (T_{abs} - T_{box}) \quad (2.8)$$

For Copper (Cu) samples or SSA samples with the copper substrate, the coefficients z_1 and z_2 are obtained by fitting the experimental average OTL ($T_{abs,}$ T_{box}) curve in Fig. 2.17 with equation (2.8). Equation (2.8) particularized for copper becomes equation (2.9):

$$OTL(T_{abs,}T_{box}) = 3.36E-12 * (T_{abs}^4 - T_{box}^4) + 0.0012 * (T_{abs} - T_{box}) \quad (2.9)$$

2.3.3 Results of bulk-copper samples thermal emittance measurements correction

By expanding OTL ($T_{abs,}$ T_{box}) in equation (2.5), are obtained the corrected total emissivity curves of the copper samples that are depicted in Figure 2.18 (a). It can be observed that after the correction, the distances between the curves corresponding to samples with different areas are significantly reduced. This indicates that it is acceptable to consider the average value as the corrected value for the bulk copper emissivity. Dividing the corrected emissivity values by two yields the emissivity of a single side of the copper sample (figure 2.18 (b)). These curves overlap with the Copper hemispherical emissivity curve found in the literature [102], confirming the success of the calorimetric equation correction.

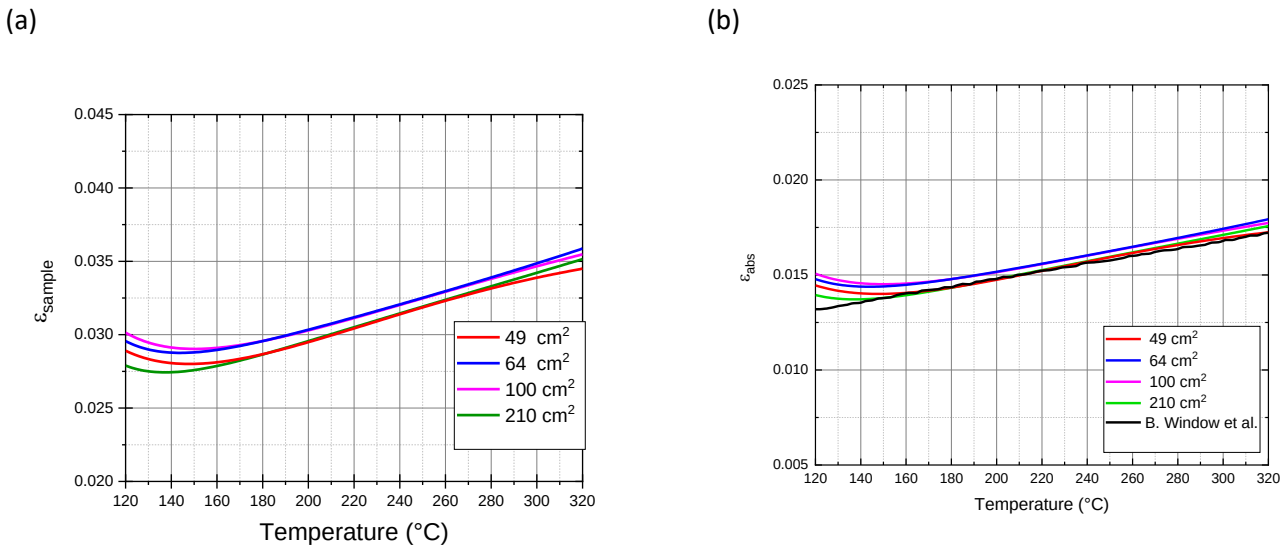

Figure 2.18 (a): Corrected total spectrally averaged emissivity of different dimensions Copper samples (210, 100, 64, 49 cm^2); (b): Corrected single side spectrally averaged emissivity of different dimensions Copper samples (210, 100, 64, 49 cm^2) compared to literature data (black line)

Once the expression for the other thermal losses function OTL ($T_{abs,}$ T_{box}) is obtained for copper samples, it becomes possible to compare the magnitude of these losses introduced by the experimental setup with the power emitted by the measured copper samples of different dimensions.

Figure 2.19 represents the ratio between OTL (in watts), and the sample emitted power (also in watts) as a function of the absorber temperature for samples of varying dimensions.

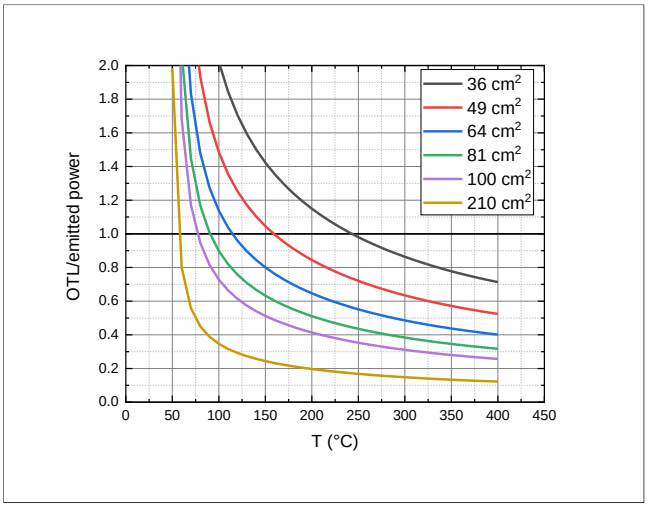

Figure 2.19 ratio between OTL and sample emitted power as a function of the absorber temperature for copper samples of varying dimensions

When the ratio OTL/emitted power is equal to 1, it indicates that the losses induced by the experimental setup are of the same order of magnitude as the power emitted by the sample during the cooling phase of the measurement. This introduces a limitation in the emissivity measurement because the losses and the emitted power become comparable. With the current configuration, considering the OTL term in the calorimetric balance equation, it is possible to assess the thermal emittance of copper samples in a temperature range of (150÷400) °C and with dimensions ranging from 64 cm² to 210 cm². However, the presence of the OTL term sets a limit on the accuracy of the emissivity measurement.

In future developments of the mini test box experimental apparatus, it is expected that advancements will be made to extend the range of samples' emittance measurability. This can be achieved by miniaturizing the thermocouple elements, which would help reduce the magnitude of the OTL term, thereby improving the accuracy and expanding the range of emissivity measurements for different sample dimensions.

2.4 FORMULATION OF A NEW EFFICIENCY MODEL VALID FOR HVFPCS AND CALCULATION OF EFFICIENCY OF HVFPCS WITH OPTIMIZED SSAS.

The improvements of HVFPC technology, like the development of new optimized SSA coatings and glass covers [103], will bring in the short term to cover applications up to 250 °C [104]. A reliable method for evaluating the annual energy production of an HVFPC equipped with a new SSA would allow for estimations regarding the potential economic advantages of adopting the new absorber. Such a method is missing in the literature, and it would be essential to provide insights into how much to invest in adopting this innovation. As explained in section 1.3, the standard efficiency coefficients (η_0, IAM_θ, c_1, c_2) are provided by the Solar Keymark certification body that obtains them through a standard test, and efficiency values for operating temperatures higher than the maximum tested temperature cannot be evaluated with standard efficiency curve extrapolation, since the radiative losses are not taken explicitly into account by eq. (1.15).

Figure 2.20 shows the MT-Power efficiency curve certified by the solar Keymark up to T_m= 200 °C (solid line) and its extrapolation until the zero-efficiency point (dashed line). Additionally, the figure includes a black arrow indicating the specific point that is the certified stagnation temperature of the MT-Power (T_m = 302 °C). The stagnation temperature of a collector refers to the highest temperature reached by the absorber surface when the collector is exposed to solar radiation without any heat transfer or fluid flow occurring. The stagnation temperature is typically measured or estimated to assess the thermal performance and potential heat gain of a solar collector system.

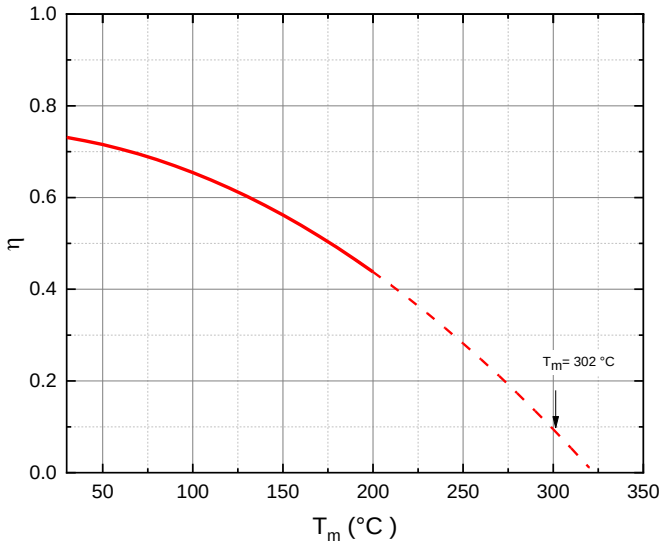

Figure 2.20 Standard thermal efficiency curve of the TVP-Solar HVFPC MT-Power and its mathematical extrapolation (dashed line) as a function of the collector temperature. The figure also indicates the certified collector stagnation temperature (T_m=302° C).

It can be noticed that in correspondence with the certified stagnation temperature, the mathematical extrapolation of the standard curve overestimates the thermal efficiency to a value of 0.1, indicating that the extrapolation overestimates the efficiency and cannot be used to predict the collector behavior at higher temperatures.

In this paragraph will be presented a novel efficiency model for the performance characterization of HVFPCs. It overcomes the limits of the standard efficiency formula, allowing the efficiency calculation up to the stagnation temperature.

The proposed formula [105] decouples the losses that depend on collector architecture from the optical and radiative losses of the SSA. It will allow us to predict the HVFPC performances at temperatures higher than the certified temperature and to accurately estimate the efficiency of HVFPCs equipped with new optimized SSAs.

2.4.1 Mathematical expression of the Efficiency Model for HVFPCs

In an HVFPC, the energy transfer from solar radiation to the HTF will occur through different heat exchange mechanisms, as shown in Figure 2.21.

The main losses in HVFPCs are the radiative losses, which depend on the absorber radiative properties (absorptance and emittance) and the glass cover transmittance, and additional thermal losses, mostly conductive, due to the thermal contact with the supporting structure; therefore, P_u can be expressed as:

$$P_u = [P_{abs} - (P_{em} + P_{add-loss})] \quad (2.10)$$

Where P_{abs} represents the amount of power transmitted by the glass, absorbed by the SSA plate, and converted into HTF internal energy increment.

It can be expressed as the product of the collector zero-loss efficiency η_0 and the Incident Angle Modifier IAM_θ :

$$P_{abs} = \eta_0 * IAM_\theta \quad (2.11)$$

P_{em} is the absorber emitted power due to the radiative heat exchange between the absorber and the surrounding elements:

$$P_{em} = \varepsilon_e(T_m)\sigma_{SB}\, A_{abs}[(T_m + 273.15)^4 - (T_{amb} + 273.15)^4] \quad (2.12)$$

In eq. (2.12), A_{abs} is the absorber surface (m^2) and T_m is the average absorber temperature, which will be considered equal to the average HTF temperature while ε_e is the total effective emittance of the absorber. In the term $P_{add\text{-}loss}$ of eq. (2.10) included all the HVFPC losses due to the panel architecture.

$$P_{add-loss} = k(T_m - T_{amb})^z \quad (2.13)$$

Where $k\ is$ the conductive heat losses coefficient while the exponent z determines the type of the additional heat losses, and it is expected to be equal to one (mostly conductive heat losses).
Explicating all the terms, eq. (2.10) becomes eq. (2.14):

$$\eta_{th,new} = \eta_0 * IAM_\theta - \left\{\frac{\varepsilon_e(T_m)*\sigma_{SB}[(T_m+273.15)^4-(T_{amb}+273.15)^4]}{G} * \frac{A_{abs}}{A_c} + \frac{k(T_m-T_{amb})^z}{G}\right\} \quad (2.14)$$

Equation (2.14) is the mathematical expression of the proposed efficiency model valid for HVFPCs.

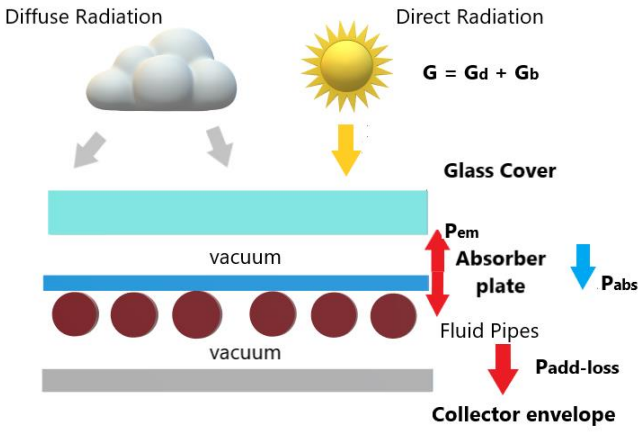

Figure 2.21 Simplified scheme of basic components of an HVFPC and thermal fluxes at interfaces.

2.4.2 Application of proposed HVFPCs efficiency model to MT-Power TVP-Solar collector

The proposed efficiency model devised for HVFPCs will be validated by its application to the TVPSolar MT-Power. When deriving the thermal efficiency formula of MT-Power, the optical properties of the SSA, such as absorptance α and effective emittance $\varepsilon_e(T)$, were obtained experimentally, in particular, the effective emittance through calorimetric measurements following the procedure described in [61].

The spectrally averaged absorptivity (α) of the commercial absorber is reported in the tab. 2.1 while $\varepsilon_e(T_m)$ is shown in Fig. 2.22.

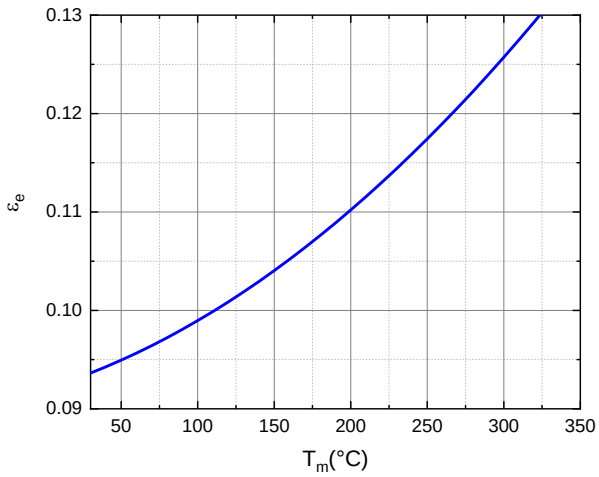

Figure 2.22 Effective thermal emittance as function of temperature for the commercial SSA mounted on MT-Power.

Given the known SSA optical properties, the unknown terms in equation (2.14) are the additional losses coefficient (k) and the exponent (z). To determine the value of k and z, equation (2.14) is fitted to the certified efficiency data obtained using the standard efficiency formula of the collector.

The standard efficiency curve is certified in the range between the minimum and the maximum tested temperature. The proposed efficiency model equation (eq. (2.14)) should accurately replicate the standard formula (1.15) until T_m = 200°C.

Through the fitting procedure, it was determined that the exponent (z) of the additional losses function that reproduces the certified efficiency is 0.93 (+/- 0.08) with a χ^2 value of 2.8E-05. This value confirms that dissipative effects other than radiation losses have a linear dependence on (T_m-T_{amb}), suggesting that they are due to thermal conduction. Since the fit result is compatible with the exponent 1 of the conductive loss, we fix the value of z at 1 to compute the coefficient of additional losses, k. The best fit was obtained for a k value equal to 0.258, and it returned a χ^2 value of 2.8E-05, and $R^2 = 0.999$ identical to the previous ones.

.

The low value of the additional losses' coefficient is not surprising due to the presence of a high vacuum in the panel and to the advanced architecture of MT-Power, specially designed to minimize conductive losses.

The efficiency formula of the MT-power collector obtained from the best fit of the solar key mark data is reported here:

$$\eta_{th} = \eta_0 * IAM_\theta - \left[\frac{\varepsilon_e(T_m)*\sigma_{SB}(T_m^4 - T_{amb}^4)}{G} * \frac{A_{abs}}{A_c} + \frac{0.258\,(T_m - T_{amb})}{G}\right] \quad (2.15)$$

Figure 2.23 shows the standard efficiency curve (red line) extended up to the stagnation temperature (red dashed line) and the curve generated by Eq. (2.15) (blue line with dots). The curves are plotted for normal irradiance at an angle of incidence of θ=0. The x-axis of Fig. 2.23 represents the average temperature T_m because Eq. (2.15) depends on the fourth power of the ambient temperature T_{amb} and the absorber temperature T_m separately.

To plot a single efficiency curve, T_{amb} must be fixed. In this case, Fig. 2.23 uses the value at which the standard test was performed (indoor measurements), i.e., T_{amb} = 20 °C. Unlike the standard curve extrapolation (Figure 2,20), Eq. (2.15) reaches zero efficiency at T_m = 302°C, which corresponds to the collector's stagnation temperature stated in the Solar Keymark certification.

Our proposed efficiency formula, Eq. (2.15), corrects the absence of the quartic temperature dependence in the standard thermal efficiency formula.

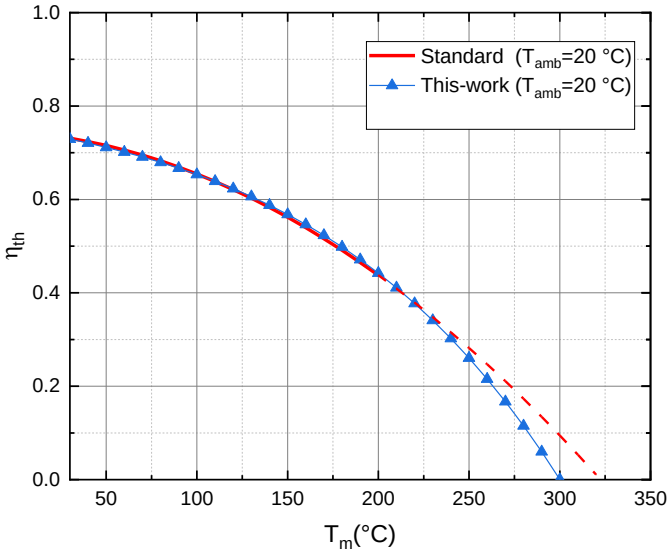

Figure 2.23 TVP-Solar MT-Power HVFPC Efficiency Curves: certified (red line) and its extrapolation up to zero efficiency (red dashed line), optical (green), and the curve obtained in this work (blue line with triangles).

Using the standard formula, the power available at 250°C amounts to 525 W, while employing our proposed efficiency formula yields 464 W, resulting in a difference of 61 W. This discrepancy increases notably with higher operating temperature T_m.

Furthermore, the same fitting procedure for Eq. (2.14) can be applied to HVFPCs with different architectures, given that we know the absorber optical properties and the standard efficiency coefficients from the Solar Keymark certification. The fitting process will provide the additional loss coefficient 'k' and the efficiency equation that can be used to extrapolate the collector performance up to stagnation. The stagnation temperature in the certification is vital information to obtain the new efficiency equation. The fact that the obtained equation passes through this specific point serves as a significant validation of the efficiency extrapolation outside the temperature range explored by the certification.

2.4.3 Application of proposed HVFPCs efficiency model to HVFPC equipped with new optimized solar absorbers.

The proposed model allows us to predict the efficiency of an HVFPC equipped with a new SSA with different optical properties. This section shows the application of the newly developed efficiency model to an MT-Power HVFPC architecture equipped with multi-layered SSA optimized for operating temperatures of 200 °C and 300 °C [28]. In Figure 2.24 (a) the thermal emittance of the commercial absorber mounted on TVP-Solar HVFPCs is represented by the blue dashed line.

Additionally, the thermal emittances of selectively coated solar absorbers (SSAs) optimized to operate at different temperatures are shown. The green dashed line corresponds to optimization for 200 °C operating temperature, while the red dashed line represents optimization for 300 °C operating temperature.

The optimization led to a significant reduction in thermal emittance, which is the primary source of heat loss for HVFPCs at elevated temperatures [41]. However, this reduction came with a slight trade-off in absorptance, with values of α_{comm}=0.95, α_{opt200} =0.925, α_{opt300} =0.890.

In Figure 2.24 (b), the curves labeled "this work" depict the MT-Power with commercial absorber (black continuous line) and the HVFPCs with the same structural characteristics as the MT-Power but equipped with SSAs optimized for 200 °C (green continuous line) and 300 °C (red continuous line).

The Figure also reports the optical efficiencies of the optimized absorbers that consider radiative losses only to underscore the importance of accounting for conductive losses, especially at elevated temperatures. Due to the different values of α, HVFPCs equipped with the optimized SSAs exhibit zero-loss efficiencies (η_0) different from those of the HVFPCs equipped with commercial absorbers.

The efficiency of the optimized SSA is consistently higher than that of the commercial absorber at temperatures higher than 120 °C since the last was not optimized to work in high vacuum.

(a) (b)

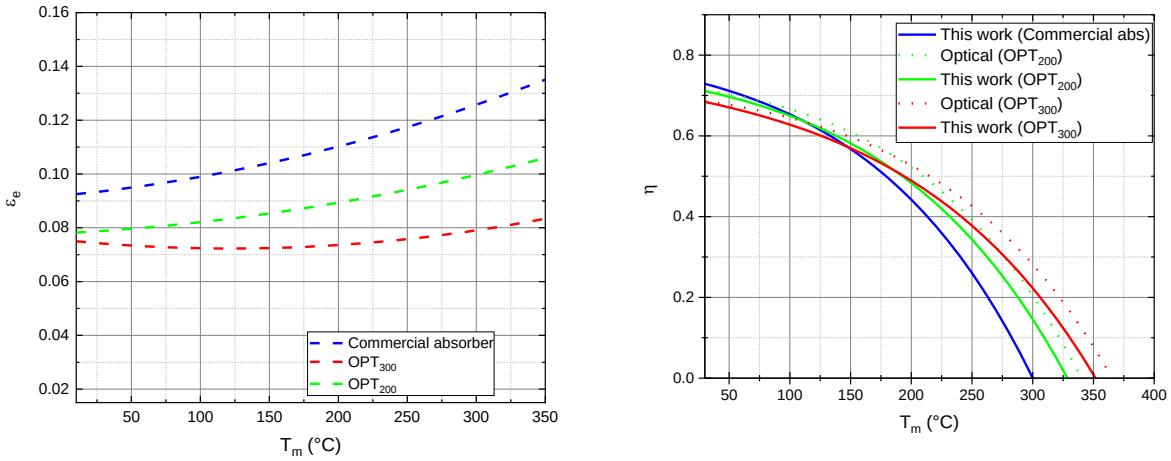

Figure 2.24 (a) Thermal emittance as function of the operating temperature for the following SSA: commercial SSA mounted on TVP-solar HVFPCs (blue dashed line), SSAs optimized to work at 200 °C (green dashed line) and 300 °C (red dashed line); (b) Thermal efficiency curves versus operating temperature for a TVP-solar HVFPC equipped with Commercial (blue line) and SSAs optimized to work at 200 °C (green line) and 300 °C (red line) obtained with the proposed efficiency model. For the optimized SSAs the optical efficiency curves, which consider the radiative losses only, are also reported (dot lines)

2.4.4 HVFPCs Annual energy producibility calculation

Thermal efficiency is the crucial parameter for energy predictions and estimating the collector's production under specific climatic conditions. Failing to account for radiative losses in the efficiency equation can lead to inaccuracies in estimating the collector's performance, especially at high operating temperatures.

Figure 2.25 presents the monthly energy production of the MT-Power at T_m=250 °C, using 2019 hourly irradiation and ambient temperature data from the specific location (Cairo). The calculation considers the energy converted by a collector that is oriented to the south and tilted at 35 °. In Figure 2.25 (a) three distinct efficiency formulas were employed: Optical (illustrated by green line squares), This-Work (represented by blue line squares), and Standard (depicted by red line squares). It's apparent that relying on the Standard efficiency formula results in an overestimation of energy production. For the year 2019, an annual energy production of 438 $kWhm^{-2}$ would be projected in contrast, using the This-Work efficiency formula indicates a more conservative estimate of 383 $kWhm^{-2}$, leading to a difference of roughly 13%.

(a) (b)

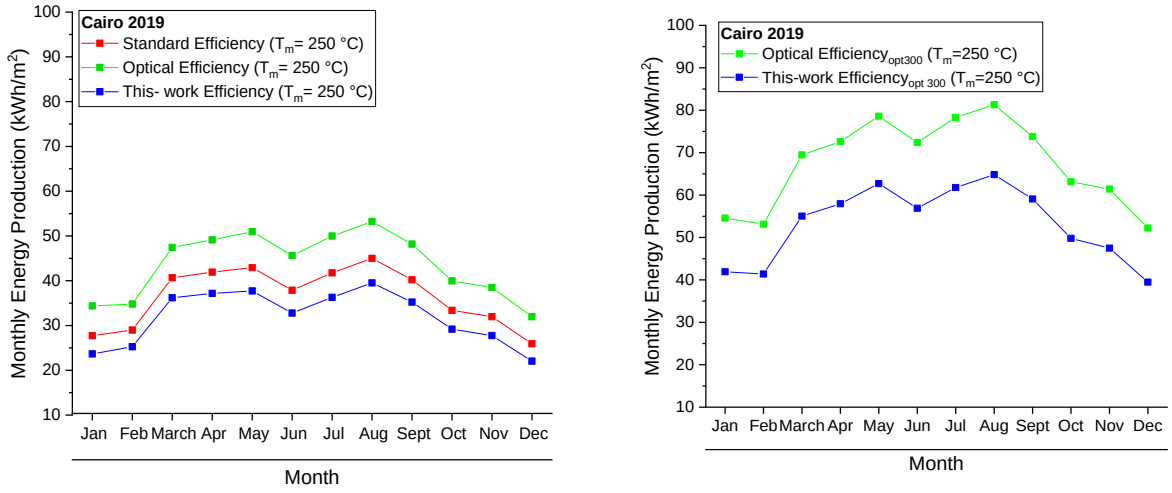

Figure 2.25 Monthly energy production (a) for MT-power collector computed using optical (green), standard (red), and this-work (blue) efficiencies; (b) for HVFPC with SSA optimized at T_m=300 °C computed using optical (green), and this-work (blue) efficiencies.

Figure 2.25 (b) underscores the importance of accounting for additional conductive losses in the efficiency calculations of HVFPCs. The figure highlights the variance in monthly energy production of an HVFPC fitted with a new absorber (optimized at 300 °C) set at an operating temperature of 250 °C.

The comparisons are drawn between results obtained using the optical efficiency (green dots and line) and those derived from the proposed This-Work efficiency model (blue dots and line).

The estimated annual energy production, as per the optical efficiency formula, stands at 811 $kWhm^{-2}$. In contrast, the This-Work efficiency formula suggests a value of 638 $kWhm^{-2}$.

Following the comprehensive overview and optimization of HVFPC technology, the third chapter will delve into the calculation of the MT-Power HFVPC absorber temperature frequency function thanks to the implementation of a dynamic simulation model using Simulink. This model represents a simple solar plant comprising a series of two evacuated flat-plate solar collectors (“Test-Bench”). The model has proven valuable for energy forecasting and various applications related to these panels, as will be elucidated in this thesis.

3. NEW PROCEDURE FOR HVFPCS TEMPERATURE FREQUENCY FUNCTION EVALUATION.

Despite the high performance exhibited by vacuum insulated flat plate collectors (HVFPCs), there is currently a lack of precise characterization regarding the behavior of this type of panel. A comprehensive and accurate characterization is essential to establish the reliability and solidity of the technology and to identify areas for improvement. The current standard for characterizing flat plate collectors in terms of aging and performance analysis does not align well with HVFPCs. In order to compete with more established solar thermal collectors in the market, it is necessary to provide information on the lifetime, energy production potential, and thermal efficiency of HVFPCs. Additionally, the development of dedicated performance analysis methods and control strategies is crucial. In the first chapter of this thesis, the efficiency expression of a solar absorber was introduced using equation 1.12. The optical properties of the absorber may undergo changes during the service life of the solar collectors due to high temperatures, resulting in a decrease in absorber thermal efficiency and energy production [105]. The standard procedure for qualifying the surface durability of solar absorbers defines the absorber temperature frequency function as an essential parameter for estimating the failure time of collectors, although evaluates it primarily for low-temperature applications such as domestic hot water production.

Due to the lack of a standard specifically for HVFPCs, a novel approach was employed to predict aging for selective solar absorbers mounted on HVFPCs and was applied to TVPSolar MT-Power HVFPC. A dynamic simulation model to investigate the behavior of HVFPCs under different conditions was implemented in this study and was used to reconstruct the temperature frequency function of HVFPCs, considering their high thermal efficiency and stagnation temperature. The simulation model provided the yearly absorber temperature history under operating conditions, while experimental data were collected to obtain the temperature trend of the HVFPCs during stagnation periods with a dedicated experimental apparatus which we refer to as Test-Bench. The resulting absorber temperature frequency function, applicable to HVFPCs, was derived for different operating temperatures, assuming a 30-day stagnation period per year, as prescribed by the standard. It should be noted that the assumption of 30 days of stagnation per year is unrealistic for thermal collectors used in industrial applications. To address this, the variation of aging parameters for different stagnation periods (fallowing periods) is also presented to provide an indication in this regard.

Before delving into the details of the new procedure for evaluating the temperature frequency function for HVFPCs, we will provide information on the tools that will be instrumental in our investigations,

such as the experimental apparatus “Test-Bench” and the implemented simulation model that replicates it.

3.1 TEST-BENCH EXPERIMENTAL APPARATUS AND ITS DYNAMIC SIMULATION MODEL.

The “Test-Bench” is a dedicated test facility designed to evaluate the performance of new versions of TVP-Solar HVFPCs through outdoor measurements. This experimental set- up is installed at the TRESOL SRL seat in Avellino.

3.1.1 Description of the experimental apparatus

Figure 3.1 depicts the considered system that comprises a series-connected array of two MT-Power HVFPCs and one collector to monitor the conditions under stagnation (with no HTF circulation, when irradiated the collector absorber reaches the maximum temperature). It includes a tank for storing the heat transfer fluid (HTF) under constant pressurization (1 MPa). A centrifugal circulation pump regulates the flow rate of the HTF circulating within the HVFPCs. Additionally, a three-way valve is incorporated to redirect the fluid through a dry cooler when the tank temperature exceeds a predetermined limit.

(a) (b) (c)

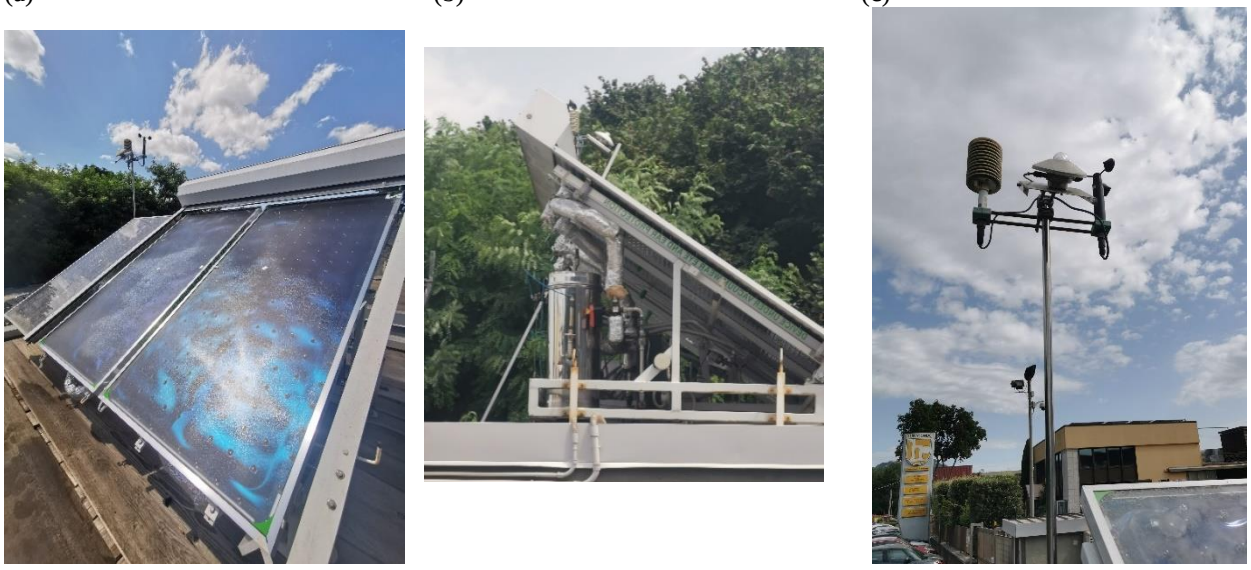

Figure 3.1 TVP Solar MT-Power HVFPCs Test-bench: the Test- Bench is composed of 2 panels connected in series that allow for HTF circulation (on the right) and one panel in stagnant conditions that allow for stagnation temperature measurements (performance parameter of the SSA). On the top of the collectors in series there is a rolling shutter that can be lowered as needed

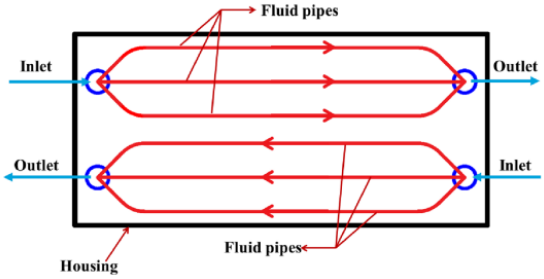

Figure 3.2 Vertical view of the MT-Power fluid pipes arrangement

(a)

(b)

(c)

(d)

Figure 3.3 Pictures of Test-Bench components : (a) fan cooler; (b) HTF storage tank; (c) frontal section of an insulated connection pipe (d) HTF circulation circuit

The collectors with fluid circulation have two inlets and two outlets (Fig. 3.2) due to the HTF flowing through the heat collector array twice, thereby minimizing heat loss from interactions with the environment.

Figure 3.3 illustrates some of the key components mentioned earlier, including the dry cooler (Figure 3.3 (a)), the storage tank (Figure 3.3 (b)), and the complete HTF circuit (Figure 3.3 (d)).

The optimal orientation of solar collectors is determined by the specific application requirements and geographical location [106]. It is characterized by two angles [107]: the Angle of Tilt (β), which is the angle between the collector plane (or aperture) and the horizontal plane, and the Azimuth angle (γ), which is the horizontal angle between true south and the direction in which the collector's surface faces. In the Test-Bench, the collectors are south-oriented (Azimuth = 0°) and tilted at 30° to maximize the capture of average annual solar irradiation (Figure 3.1 (b)). All connection pipes are insulated with a rockwool layer (Figure 3.3 (c)).

In addition to the primary components, the Test-Bench is equipped with a series of sensors that allow for the monitoring of panel and fluid operating conditions, as well as the reconstruction of environmental conditions during operation. Temperature control of the stored and flowing HTF is crucial for performance evaluation, as well as maintaining the pressure within the collector to ensure vacuum insulation. Pressure control can be observed directly through the oxidized getter pump, which leaves a white cast on the collector glass. The list of sensors installed in the experimental set-up and the corresponding controlled physical quantities is presented in Tab. 3.1.

The activation and control of the experimental set-up are carried out using a computer connected to it through LabVIEW software specifically developed for this purpose. The Test-Bench can operate in manual mode, allowing users to adjust the pump and fan cooler frequency, set the temperature, activate the tank heater, and more. Alternatively, pre-programmed modes can be used after defining the power objective of the measurements. Various parameters can be obtained, such as the panel's temperature variation over time, pressure drop over temperature increment, and, indirectly, the panel's thermal efficiency under specific conditions.

The temperature difference between the temperature sensor installed at the panel inlet and the one installed at the panel outlet provides the panel delta T. By knowing the mass flow rate (measured by the Coriolis mass flow meter), delta T, and the properties of the circulating heat transfer fluid, the power transferred from the panel to the fluid can be calculated using the principles of calorimetry:

$$Q_{to\ fluid,meas} = \dot{m} c_p(T_{f,m}) \Delta T \quad (3.1)$$

Here, $\dot{m}$ represents the mass flow rate (kgs^{-1}) circulating within the solar panel ducts, $c_p(T_{f,m})$ is the specific heat of the heat transfer fluid (kJ/kg·K) (obtained from the fluid properties chart) at the

average temperature between the panel's inlet and outlet $(T_{f,m})$, and ΔT is the temperature increment of the fluid crossing the panel $(T_{f,o} - T_{f,i})$.

Tab. 3.1 List of the controlled physical quantities of the Test Bench components and respective sensors

Component	Measured physical property	Sensor	Model
Tank	Temperature Down	Piezoresistive pressure transmitter	KELLER 21Y
	Inlet HTF Temperature	type K Thermocouple	Endress+ Hauser TSC 310
	Outlet HTF Temperature	type K Thermocouple	Endress+ Hauser TSC 310
Panel 1	Glass Temperature	type K Thermocouple	Endress+ Hauser TSC 310
	Case Temperature	type K Thermocouple	Endress+ Hauser TSC 310
	HTF Inlet Temperature	PT100	Endress+Hauser Easytemp TMR31
	HTF Outlet Temperature	PT100	Endress+Hauser Easytemp TMR31
	Pressure	Vacuum Gauge	
Panel 2	Glass Temperature	type K Thermocouple	Endress+ Hauser TSC 310
	Case Temperature	type K Thermocouple	Endress+ Hauser TSC 310
	HTF Inlet Temperature	PT100	Endress+Hauser Easytemp TMR31
	HTF Outlet Temperature	PT100	Endress+Hauser Easytemp TMR31
Circulation Circuit	Mass Flow Rate	Coriolis Mass Flow Rate sensor+ converter	YOKOGAWA Rotamass MCCF31
Weather Station	Ambient Temperature	Thermometer	COMET F8000
	Solar irradiation	Pyranometer	CMP 10 KEEP & ZONEN
	Wind Speed	Anemometer	

The thermal efficiency of the solar collector, denoted as η_{exp}, is defined as the ratio of the heat obtained by the average temperature of the heat transfer fluid at the inlet and outlet to the incident solar radiation multiplied for the collector area:

$$\eta_{exp} = \frac{Q_{to\ fluid,meas}}{G * A_c} \qquad (3.2)$$

3.1.2 "Test- Bench" dynamic simulation model description.

A dynamic simulation model of the system explained in the previous section have been implemented in Simulink [108]. By importing weather data from an online database, the model can simulate the functioning of the panels in a wide range of climate conditions.

Daily, monthly, and annual simulations can be performed to compute the instantaneous and cumulative power output as well as the thermal history of the panels. In Simulink, the primary interface consists of a graphical block diagramming tool and a customizable set of block libraries. This interface is utilized to develop a dynamic simulation model that replicates an existing Test-Bench

The simulation model is constructed using blocks from the Simscape Simulink library, which contains all the necessary components for the implementation. Figure 3.4 provides a schematic representation of the considered system.

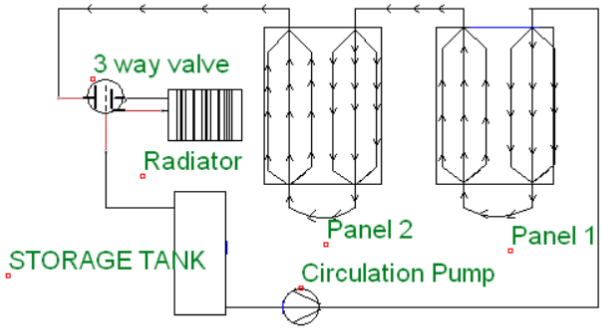

Figure 3.4 Simplified scheme of the Test-Bench

In Simulink, the system can be divided into several subsystems that are interconnected as shown in Figure 3.5.

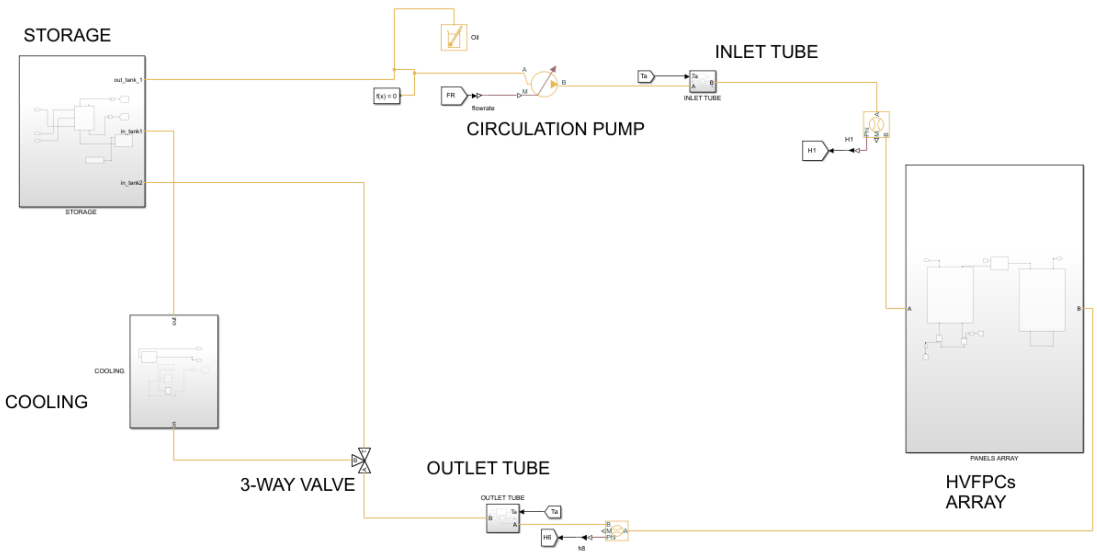

Figura 3.5 Simulink Test Bench model

The first subsystem, called STORAGE (Figure 3.6 (a)), represents the tank where the HTF is stored. The central block of this subsystem is the tank (TL), which models a thermal liquid network storage tank with constant pressurization and a configurable number of inlets (up to three). The tank parameters, such as volume and liquid level, are selected to match the real tank structure and material of the Test-Bench. When the circulation pump is activated, the HTF exits the tank through the tank outlet C. After circulating through the two panels, the fluid returns to the tank through inlet A if no cooling is required. However, if cooling is necessary, the fluid flows into the radiator circuit and returns through inlet B. The interaction between the tank and the external ambient is modeled through the ambient subsystem (Figure 3.6 (b)).

(a)

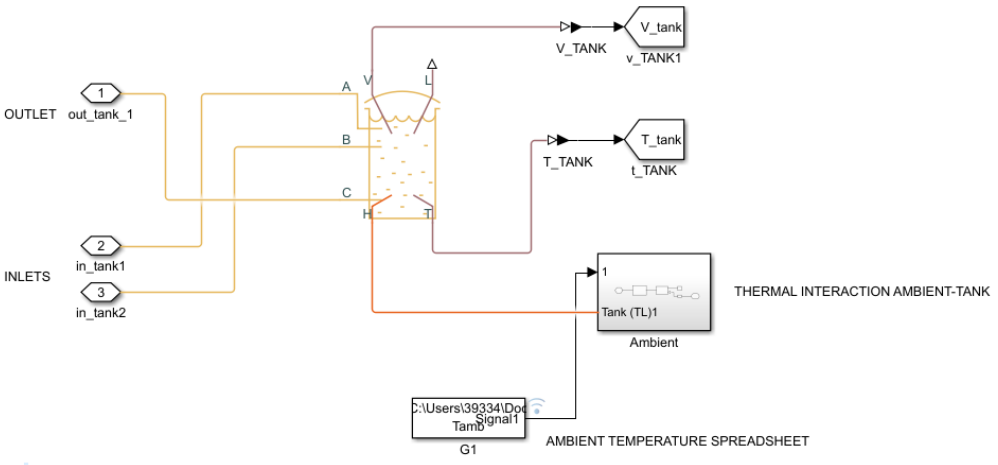

(b)

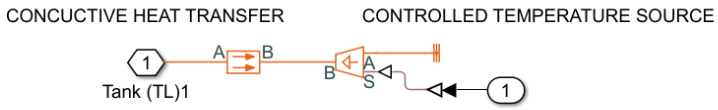

Figure 3.6 HTF Storage Subsystem: (a) Elements that composes the subsystems; (b) Ambient subsystem structure

The HVFPCs ARRAY subsystem (Figure 3.7 (a)) is composed by other 5 subsystems: PANEL 1, PANEL 2, PANELS CONNECTIONS, END PANEL 1, and END PANEL 2.

PANEL 1 and PANEL2 represent the HVPFCs of the Test-Bench that allow HTF circulation. When the HTF flows through the HVFPCs, its temperature increases due to interaction with the absorber plate. As there is vacuum between the absorber and the glass cover, there are no convective or conductive heat losses within the panels, only radiative losses.

However, when the HTF flows through the connections between the first and second halves of the panels and between consecutive panels, conductive and convective heat losses must be considered. The END PANEL 1, END PANEL 2, and PANELS CONNECTION subsystems (Figure 3.7 (b)) have identical structures. The first two represent the circuit between the outlet of the first half of the panel and the inlet of the second half. The PANELS CONNECTION subsystem represents the circuit between two consecutive panels.

Even PANEL 1 and PANEL 2 share the same structure, each containing two subsystems called HALF PANEL (Figure 3.7 (c)), which models the HTF circuit between each panel's inlet and outlet. Having the MT-Power two inlets and two outlets, necessitates the presence of two half panels in the panel subsystem.

The HALF PANEL subsystem is the most important component of the simulation model. The controlled heat flow rate source block provides the solar power transferred to the HTF while passing through the first half of the solar panel. This heat flow rate is calculated using the formula:

$$Q_{to_{fluid}} = \eta_{th,st} * G * A_{hp} \quad (3.3)$$

Here, $\eta_{th,st}$ is the MT-Power standard efficiency expressed by relation (1.15), G (Wm^{-2}) is the global Solar Irradiation (normal and diffuse) incident on Panels surface and A_{hp} is the Half Panel surface.

The simulation model also includes the presence of a subsystem called COOLING (Figure 3.8) which contain a block of Simscape library that models a Radiator. The working temperature of the HTF must be regulated to ensure the system's operational reliability. After passing through Panel 2, before returning to the tank, the HTF flows through a THREE-WAY DIRECTIONAL VALVE, whose position is determined by a temperature signal. When the tank's temperature exceeds the activation temperature for the cooler, the valve opens, allowing the fluid to pass through the radiator. Otherwise, the fluid continues to flow back into the tank.

Once developed, the simulation model can accurately predict the performance of the system under various scenarios and locations. The dynamic model requires weather data, including ambient temperature solar irradiation and incident angle on collector surface, as input variables. The simulation model predictions are based on a standard efficiency formula derived from a standard indoor test conducted under steady-state conditions.

To validate the dynamic simulation model, we chose to numerically reproduce the measurement conditions of a single day of outdoor experimental performance measurements of the MT-Power HVFPCs (7^{th} December 2022) using the Test-Bench located at TRESOL SRL in Contrada Santorelli, as depicted in Figure 3.9 The simulation results were compared with the experimentally obtained results, and a good agreement was observed, as explained in the following sections.

Further details about the experimental set-up will be provided in the subsequent section.

(a)

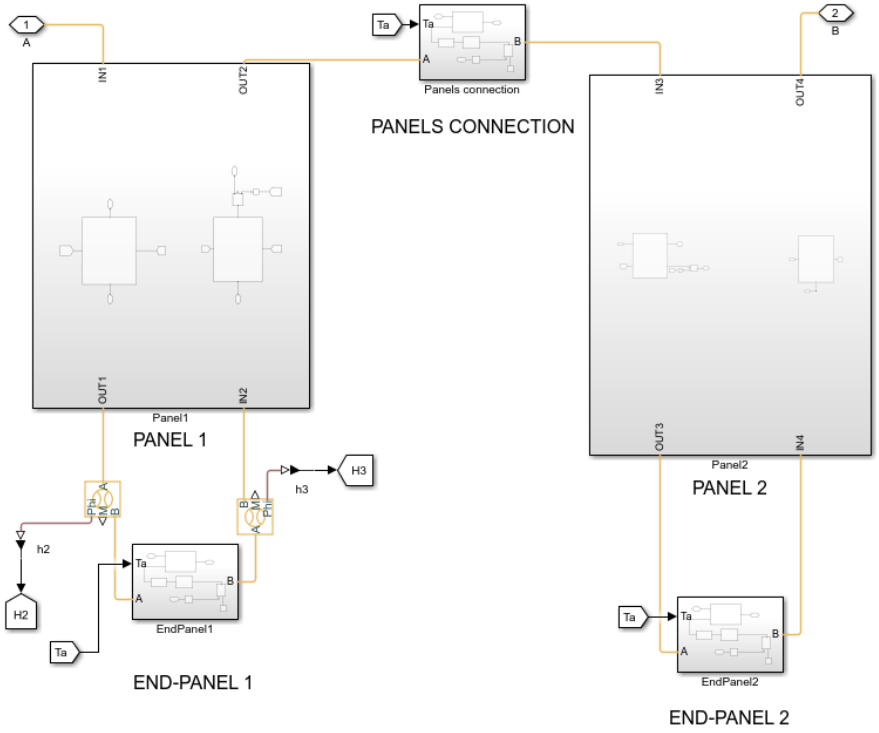

(b)

(c)

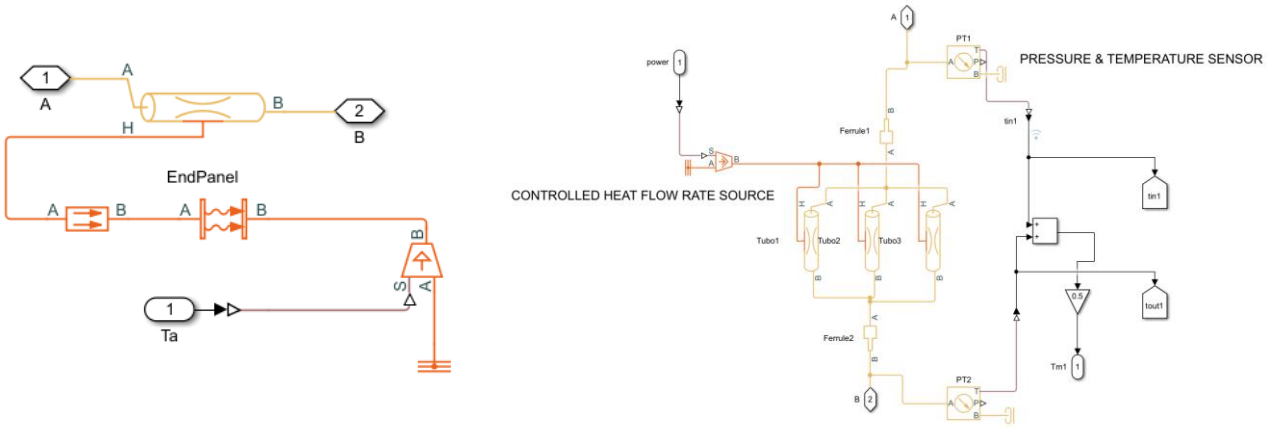

Figure 3.7 HVFPCs Array Subsystem: (a) Elements that composes the subsystems; (b) End Panel subsystem structure; (c) Half Panel HTF circuit subsystem structure

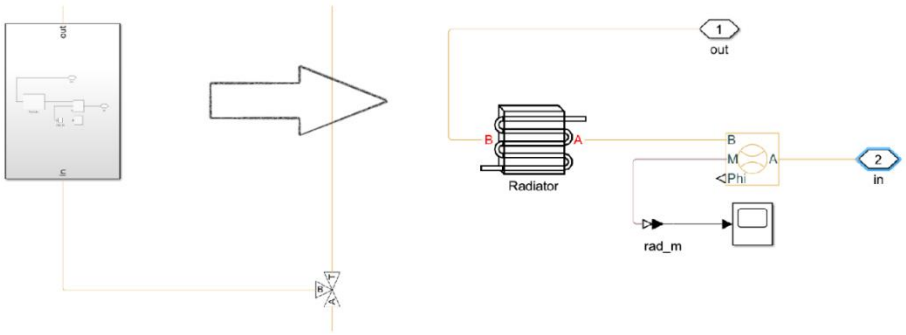

Figure 3.8 Cooling subsystem structure

3.1.3 Daily simulation validation

To validate the dynamic simulation model of the test bench, we conducted a comparative analysis between the simulated results and the daily experimental measurements obtained from the test bench. The experimental measurements were performed on December 7th, 2022, utilizing Therminol 66 [109] as the designated heat transfer fluid, with the tank's setup temperature (or cooler activation temperature) set at 95°C.

(a)

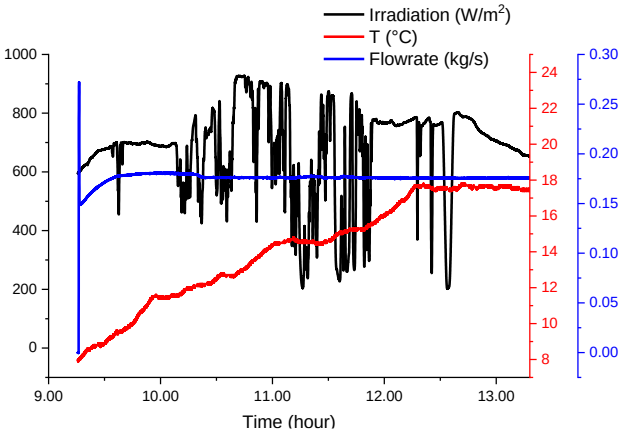

(b)

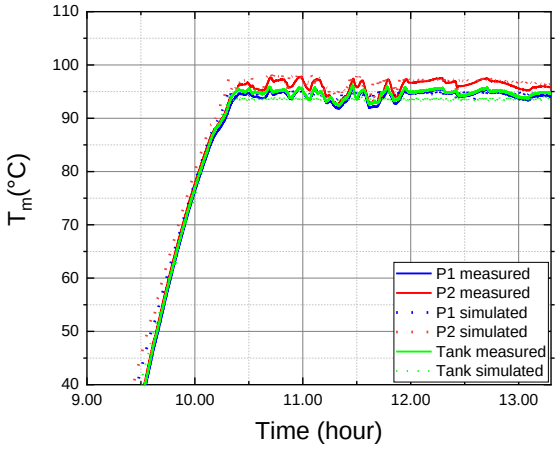

Figure 3.9: (a) 7th December 2022 acquired weather data and HTF flow rate used as inputs of the dynamic simulation; (b) comparison between simulation results (dot lines) and experimentally acquired data (solid lines) of Test-Bench tank and collectors daily temperature measurements made on 7th December 2022

Data acquisition during the experiment was conducted at a sampling rate of 1 second, incorporating environmental variables such as ambient temperature, irradiance, and mass flow rate, captured by the Test-Bench's weather station (Fig. 3.9 (a)), as inputs for the simulation while the solar radiation incidence angle was determined using the SolPos [110] online tool.

In order to validate the model, we compared both the measured and simulated average fluid temperatures (T_m °C)) within panel 1, panel 2, and the tank as showed in Fig. 3.9 (b).
The graph in Fig. 3.9 (b) illustrates the temporal evolution of temperatures, and the simulation results exhibit good agreement with the experimental measurements. During this period, the observation was concluded by closing the shutters of the test bench before solar irradiance reached zero.

3.2 HVFPCs Temperature Frequency Function: calculation procedure and results.

The experimental data and results from the validated dynamic simulation were employed to assess the temperature frequency function of the MT-Power HVFPC absorber. This function is a crucial parameter in calculating the service lifetime of a collector. Before delving into the specifics of the procedure, it is essential to establish the relationship governing the aging process for a thermal collector.

3.2.1 Definition of aging parameters for HVFPCs service lifetime evaluation

For the evaluation of HVFPCs' service lifetime, aging parameters are defined based on the ISO/CD 12592, 2 standard *[111]*, which assumes that the degradation of the absorber follows the Arrhenius law. The Arrhenius law describes the temperature dependence of chemical reaction rates k, with the activation energy per mole of the ageing process (E_T) being a key parameter determining the aging resistance at the operating temperature.

$$k = D_{Arrh} exp\left(\frac{-E_T}{RT}\right) \quad (3.4)$$

where k, D_{Arrh} is the Arrhenius constant, R is the constant of ideal gas and T is the temperature. The absorber temperature changes during the normal working conditions. Such temperature variations can be summarized by a temperature frequency function $f(T)$ that represents how many hours the absorber is at temperature T during one-year operation. By integrating the complex temperature frequency function (f(T)) over a temperature range, an effective constant temperature (T_{eff}) can be derived, which produces the same aging effect as the actual temperature variations.

This allows accelerated aging tests to be conducted at higher temperatures than the operating temperature to estimate the failure time, defined as the point at which the absorber's efficiency is reduced beyond a predefined threshold.

$$\exp\left(\frac{-E_T}{RT_{eff}}\right) = \int_{T_{\min}}^{T_{\max}} \exp\left(\frac{-E_T}{RT}\right) f(T) dt \quad (3.5)$$

Here,T_{max} and $T_{min}$are the maximum and minimum temperature of the solar absorber observed over one year operation.

The standard also introduces a Performance Criterion (PC) to estimate the activation energy (E_T) through aging tests. The PC is calculated based on the change in absorptance (α) and emittance (ε) before and after testing (eq. 3.6).

$$PC = k * t = -\Delta\alpha + 0.5\Delta\bar{\varepsilon} \quad (3.6)$$

$\Delta\alpha = \alpha'_s - \alpha_s$, $\Delta\bar{\varepsilon} = \bar{\varepsilon}'_t - \bar{\varepsilon}_t$, where α'_s and $\bar{\varepsilon}'_t$ represent the absorptance and the emittance after testing, while α_s and ($\bar{\varepsilon}_t$) are the absorptance and the emittance before testing.

Once E_T and T_{eff} are determined, the failure time (t_R) can be calculated in years for a given testing temperature (T_R), using the expected service lifetime of the collector (LT):

$$t_R = LT\exp\left(-\frac{E_T}{R}\left(\frac{1}{T_{eff}} - \frac{1}{T_R}\right)\right) \quad (3.7)$$

The values of t_R and T_R are a compromise between the requirements of a testing time easily accessible (no more than few weeks), easily measurable with a small relative error (at least one hours), and a testing temperature not too higher than the stagnation temperature, to avoid the activation of other degradation mechanisms (with a different activation energy).

Both the temperature frequency function (f(T)) and the Performance Criterion need to be adapted to the specific type of collector under analysis to obtain reliable calculations of the failure time. Unfortunately, there is a lack of specific standards for performance evaluation and absorber qualification regarding HVFPCs. However, a new Performance Criterion suitable for selective solar absorbers for middle-temperature applications has been proposed by [112]. It considers the efficiency difference ($\Delta\eta_{abs}$) before and after testing and can be used to assess the aging of the absorber.

$$PC_\eta(T) = \Delta\eta_{abs}(T) \quad (3.8)$$

$\Delta\eta_{abs}(T) = \eta_{abs}(T) - \eta'_{abs}(T)$, where $\eta_{abs}(T)$ is the efficiency of the absorber before testing and $\eta'_{abs}(T)$the efficiency of the absorber after testing.

The standard presents the temperature frequency function (f(T)) based on averaged measured values from four different flat-plate collectors used for domestic hot water applications. These collectors were exposed for one year in Rapperswill (Switzerland) and operated for 11 months with 30 days under stagnation (fig. 3.10).

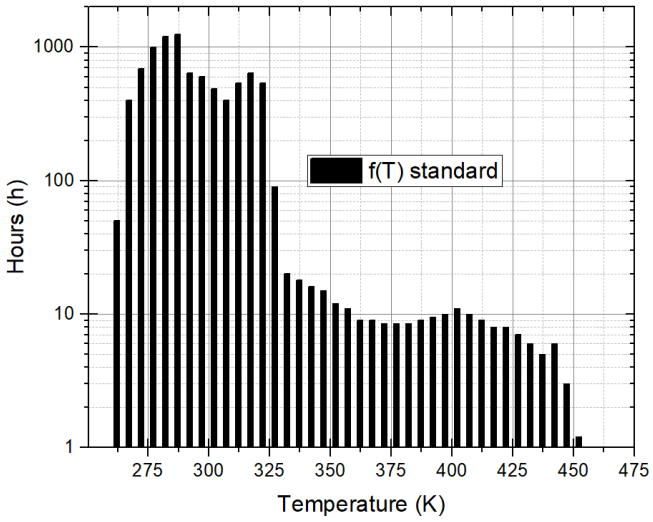

Figure 3.10 Temperature frequency function defined by ISO/CD 12592, 2

In figure 3.10 we can notice that the maximum temperature reached by the absorber of the collectors analyzed is equal to 180 °C. An update procedure, described by [113], enables the adaptation of the standard temperature frequency function (f(T)) to other types of solar collectors by considering variations in stagnation temperature while assuming that the shape of the temperature curve will remain unchanged for different absorber optical properties.

3.2.2 Rescaled f(T) for absorbers with stagnation temperature of 300 °C.

TVP-Solar MT-Power HVFPCs can work at higher operating temperature than conventional flat plate solar collectors thanks to the elimination of convective thermal losses guaranteed by the high vacuum insulation. The SSA adopted in the MT-Power achieve stagnation temperatures higher than 300 °C (302 °C as certified by the Solar keymark [52]. A procedure to re-scale $f(T)$ for absorbers with different stagnation temperature is presented in [113]. The assumption that stagnation conditions occur 30 days in a year remains valid. The temperature histogram for 1 year for the case of a maximum stagnation temperature of 180 °C is presented in fig. 3.11). To calculate the corresponding temperature histograms for cases of other maximum stagnation temperatures (T_{n_max}), simple re-scaling was made according to:

$$T_n = (T_{453\,K} - 288\,K)\left[\frac{T_{n\_max} - 288\,K}{453\,K - 288\,K}\right] + 288\,K \qquad (3.9)$$

where T_n is the rescaled temperature and $T_{473\,K}$ is the corresponding temperature for the case of a maximum stagnation temperature of 453 K (180 °C). When adopting re-scaling, we made the assumptions that the night temperature is 288 K (14 °C).

The Standard and the re-scaled absorber temperature frequency function for collectors with stagnation temperature of 300 °C, are reported in Fig. 3.11 in black and red respectively. Setting a hypothetical value of the activation energy (E_T) of 100 kJ/mol, the T_{eff} obtained from the re-scaled histogram, using eq. (3.5) is equal to 190 °C.

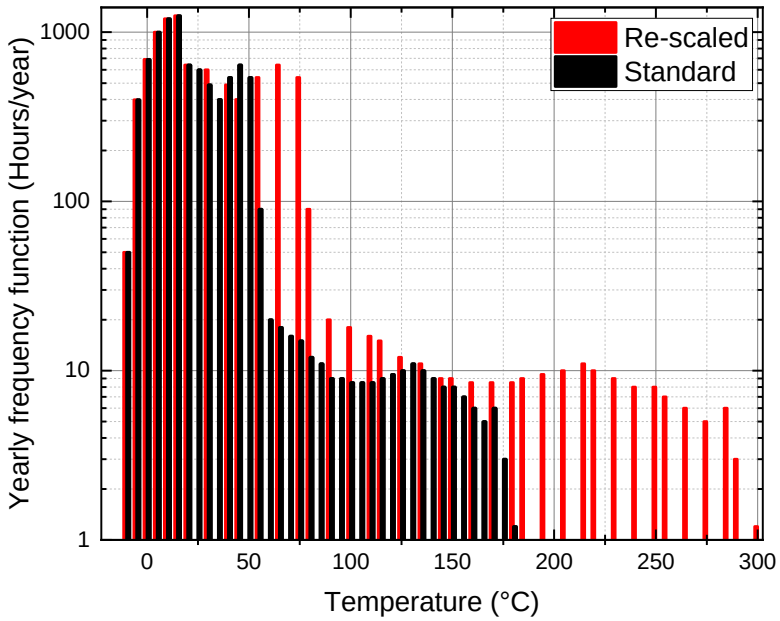

Figure 3.11 Histogram in black: Reference absorber temperature frequency function valid for absorber with stagnation temperature of 180 °C (standard f(T)). Histogram in red: Re-scaled absorber temperature frequency function valid for absorbers with stagnation temperature of 300 °C.

3.2.3 New methodology for HVFPCs f(T) calculation and results.

The novel calculation procedure for f(T) involves the utilization of HVFPC (High Vacuum Flat Plate Collector) dynamic simulation, as described in section 3.1, to construct the absorber temperature history under operating conditions. Conversely, the temperature trend under stagnant conditions is derived from experimental data. In this particular application, MT-Power was chosen as the HVFPC, and we aim to obtain the f(T) for this specific model [114]. The system model was modified to include only one collector, as depicted in figure 3.12.

In the computation of f(T), it is assumed that the instantaneous temperature of the Heat Transfer Fluid (HTF) is equal to the collector absorber temperature, and the absorber optical properties remain constant throughout a year of operation. The dynamic simulation, conducted in a transient manner, provides the instant working fluid medium temperature $T_m(t)$ at each time step, which is a necessary parameter for constructing f(T). By obtaining the average temperature distribution of the HTF over the simulated time, which is considered equivalent to the absorber's average temperature distribution, we can derive the simulated temperature frequency function f(T) for the operating conditions.

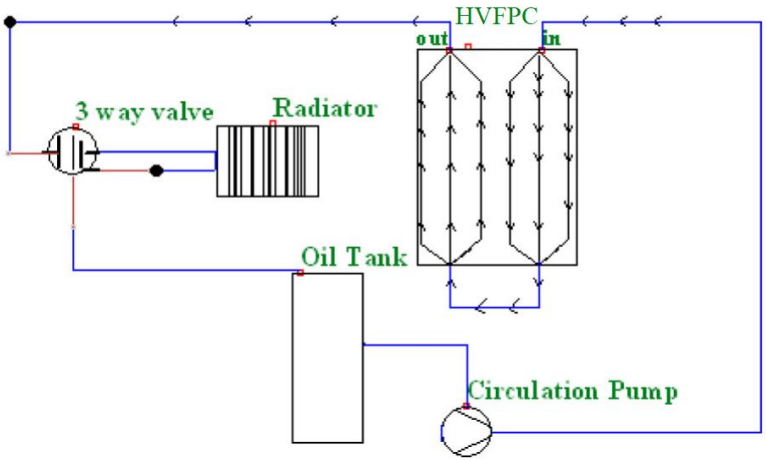

3.12 simplified scheme of the system modelled to obtain HVFPCs f(T)

The dynamic simulation model for the commercial HVFPC calculates the instantaneous power converted by the collector and transferred to the HTF (eq. 3.1), taking into account the standard efficiency (eq 1.15). The standard MT-Power efficiency is valid for a maximum temperature of 200 °C; therefore, the mathematical model presented above is not applicable for higher collector temperatures. For stagnant conditions, the temperature profile of a highly selective absorber (fig. 3.13 (a)) was measured in the MT-Power configured for stagnation measurements and mounted on the TVP-Solar HVFPCs Test-Bench installed in Avellino, Italy (see fig. 3.13 (a)). The profile was recorded on September 28, 2018, with a maximum global radiation of approximately 1000 Wm^{-2} (Fig. 3.13 (b) measured on the collector plane). The stagnation temperature reached 302 °C. The corresponding daily absorber temperature frequency function f(T) represents the sample daily f(T) for HVFPCs under stagnant conditions. By multiplying the daily f(T) by 30, we can derive the f(T) for a month of stagnation (see Fig. 3.14 (a)). A new f(T) suitable for HVFPCs is provided to obtain more reliable results compared to those obtained with the rescaled f(T) (red histogram in Fig. 3.11). The histograms relative to HVFPCs considering four different Operating Temperatures (O.T. = 60 °C, 90 °C, 120 °C, 180 °C), obtained through dynamic simulations and experimental data, are represented.

The minimum O.T. is characteristic of Domestic Hot Water (DHW) applications, while the maximum O.T. serves as a reference value for medium temperature applications.

The dynamic simulation yields the temperature trend of the collector over the simulated time, which is subsequently summarized as a histogram. To ensure a direct comparison, the dynamic simulations use meteorological data from the standard test location (Rapperswill). The hourly meteorological data were downloaded from the Solar Radiation tool of the Joint Research Centre (JRC) website [115],with the desired year, location coordinates, and collector orientation angles set.

The simulation model also requires the characteristics of the HTF, and in this case, XCELTHERM®500 [116] (-60 – 260 °C) was selected, with a mass flow rate during daylight hours set to the nominal value for oil $\dot{m}$ = 516 (kg/h) (as reported in the MT-Power certification [21]). The TVP-Solar HVFPC absorber temperature frequency functions f(T) obtained from simulations at different O.T.s are presented in Fig. 3.14 (b).

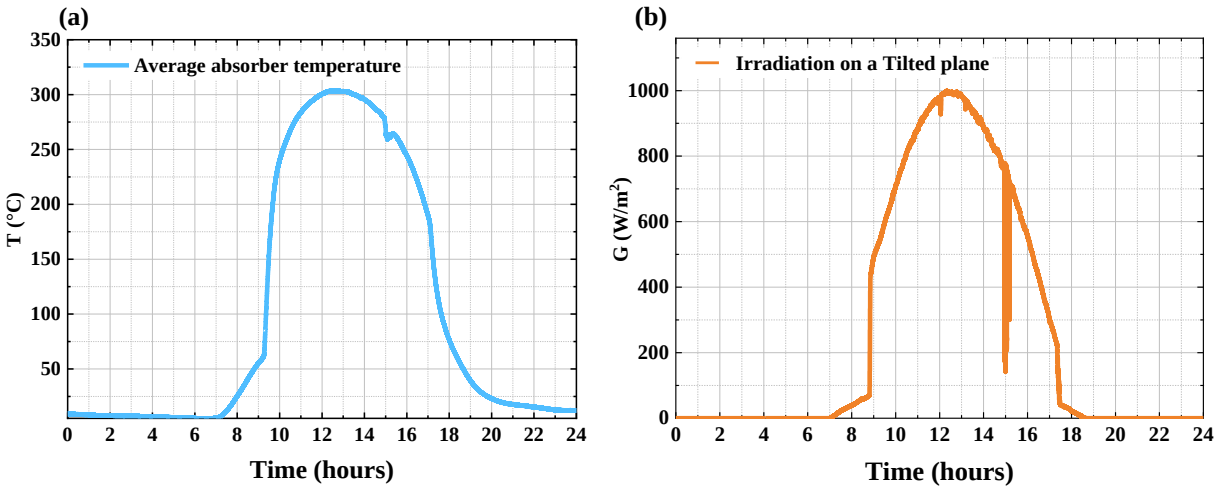

Figure 3.13 (a) Measured temperature of a selective absorber in a High Vacuum Flat Plate Collector during stagnation; (b) Measured solar Irradiation on collector plane

The temperature range for analysis extends from -20 to 305 °C, divided into intervals of 5 °C. In Fig. 3.14 (b) (logarithmic scale), the number of hours in which the collector absorber operates within each interval can be observed. The temperature data for the stagnation period are obtained from the histogram in Figure 3.14 (a). Unlike the rescaled f(T) (Figure 3.11), it is notable in Figure 3.14 (b) that the collector operating temperatures (O.T.s) are easily distinguishable (the temperatures at which the absorber reaches the highest number of hours). Analyzing the case of an O.T. equal to 180 °C, it is evident that the shape of the f(T) is different from the other cases, providing a clear indication that the High Vacuum Flat-Plate Collector (HVFPC) is not able to operate at that temperature for a desirable number of hours under the meteorological conditions of Rapperswil. By utilizing the histograms reported in Figure 3.14 (b) to compute the effective temperature (T_{eff}) (assuming an activation energy of 100 kJ/mol), the results are 242 °C for every considered case (for every O.T.) instead of the 190 °C obtained with respect to the rescaled f(T).

The difference between the analyzed cases is negligible because, due to the strong non-linearity of the Arrhenius-type kinetics (see Equation 3.4), the temperature load under operating conditions affects the calculation much less than the load under stagnation, which does not depend on O.T.

Establishing that the stagnation period plays the main role in the calculation of T_{eff}, it is observable that the assumption made by the Standard of 30 days of stagnation in one year is realistic for conventional flat-plate collectors used to produce domestic hot water (DHW).

However, when considering HVFPCs for industrial applications, 30 days of unproductivity cause unacceptable energy loss. The T_{eff} computed for every considered collector operating temperature (O.T. = 60 °C, 90 °C, 120 °C, 180 °C) by varying the length of the stagnation period (1, 2, 3, 4, 5, 10, 15, 20, 25, 30 days) are reported in Figure 3.16, which shows a logarithmic trend of T_{eff} with increasing stagnation period length. The graph also includes the T_{eff} computed using the rescaled f(T) (30 days of stagnation). As the days of stagnation increase, the influence of the different working temperatures on T_{eff} becomes less significant. In the case of no stagnation (stagnation period length = 0), the T_{eff} for each O.T. is almost equal to the collector O.T. considered.

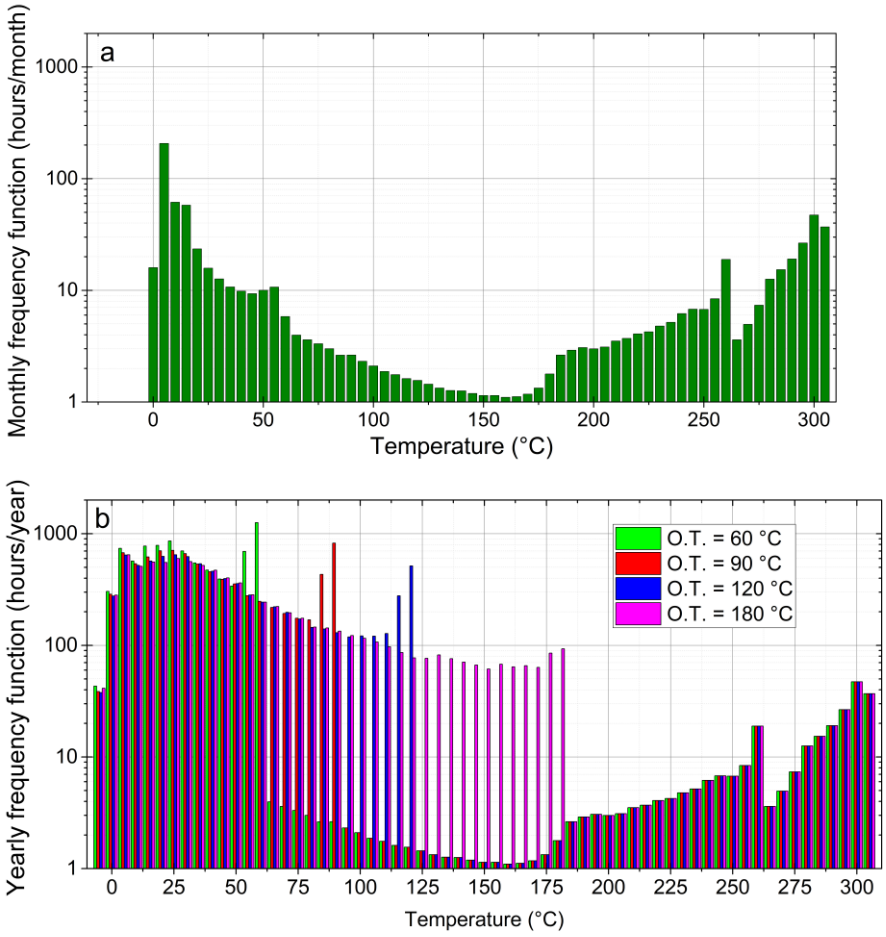

Figure 3.14 (a) HVFPC f(T) relatives to 30 days of stagnation (b) Absorber temperature frequency functions relative to 11 months of operation and 30 days of stagnation valid for HVFPCs considering 4 different operating temperatures (O.T. = 60 °C, 90 °C, 120 °C, 180 °C).

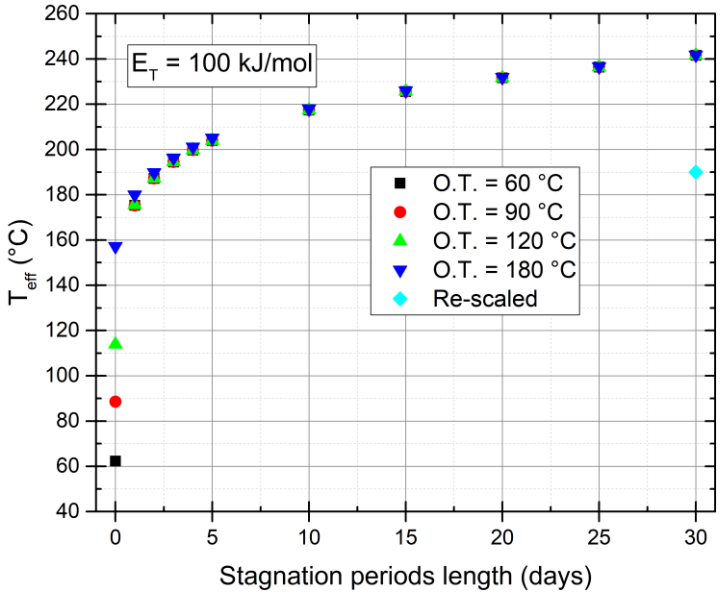

Figure 3.15 Variation of T_{eff} with stagnation periods length for 4 operating temperatures (O.T. = 60 °C, 90 °C, 120 °C, 180 °C).

The difference in terms of T_{eff} obtained at the different operating temperatures of 60 °C, 90 °C, 120 °C is negligible even from the first day of stagnation. After 10 days of stagnation, all the considered operating temperatures become equivalent with respect to the T_{eff} calculation. Therefore, it is important to predict a realistic period of inactivity for the industrial solar plant in order to calculate a reliable effective temperature of the solar collectors.

The results clearly show that there is a difference in the evaluation of the f(T) when following the current standard compared to using the simulation model with any operating temperature considered. This difference leads to a different calculated value of T_{eff} and, consequently, a different failure time. For this reason, the use of the simulation model to predict the f(T) for HVFPCs is more reasonable. Furthermore, based on the data obtained from the HVFPC solar field of TVP Solar, it can be assumed that the field operates without any unproductive days throughout the year, which is justified for industrial applications. Accordingly, the evaluation of the temperature frequency function using the above-presented simulation model is shown in Figure 3.16 for three different locations (Dubai, Naples, Paris), with an operating temperature of 180 °C and considering a stagnation period length of 0 days.

The procedure for evaluating f(T) described in this paragraph can be improved by replacing, in the dynamic simulation, the standard efficiency expression with the new efficiency model specifically designed for HVFPCs, as presented in Chapter 2.

This new efficiency model enables the calculation of f(T) even under stagnant conditions, making it possible to perform the computation solely using the dynamic simulation model.

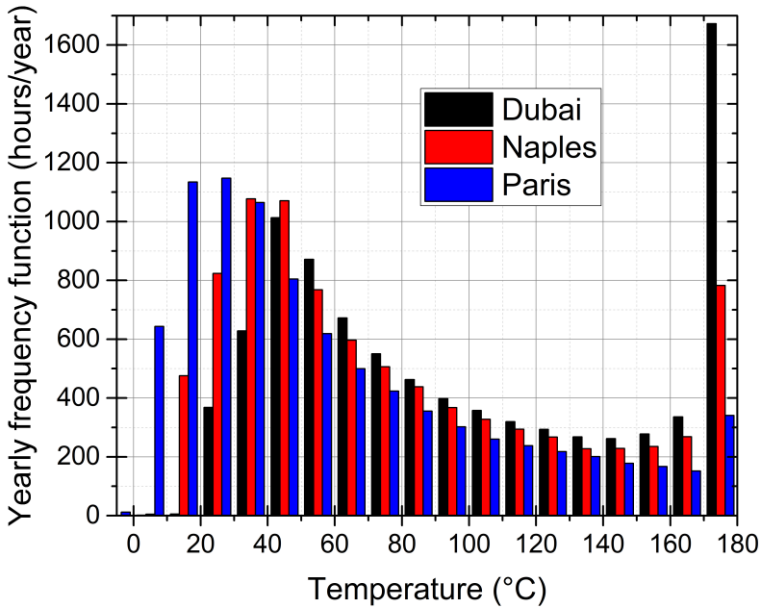

Figure 3.16 Temperature frequency function evaluation for an operating temperature of 180 °C, with 0 days of stagnation period length and for 3 different locations Dubai, Naples, and Paris (black, red, and blue column respectively).

Summarizing, in this chapter a methodology to derive the yearly absorber temperature frequency function valid for High Vacuum Flat Plate Collectors (EFPC), guaranteeing high accuracy, is presented. The methodology prescribes to reconstruct the absorber temperature frequency function during operating conditions using a dynamic simulation based on an efficiency model characteristic for HVFPCs. Using the simulation model for service-time and experimental data for stagnation, if assumed the exact fallowing period for the solar plant, a greater accuracy of HVFPC failure time evaluation is obtained. The flexibility of the simulation model consists in the possibility to obtain the f(T) in every desired location, operating conditions, and for every collector by changing the efficiency formula and input data and, for this reason, it is a very useful instrument not only to make life-conditions prediction for the absorber but even to give energetic and economic forecasts.

4. CASE-STUDY: PERFORMANCE MEASUREMENTS AND SIMULATION OF AN HVFPCS TEST- FIELD

In this thesis we have discussed HVFPC technology, how we have worked over the years to develop optimized components for these solar thermal collectors, and we have developed dedicated procedures and mathematical models for characterizing their performance. In the literature, there is still limited data on the actual production capabilities of fields equipped with HVFPCs, mainly because they are often operated well below their optimal operating temperatures. To conclude this work a Case-Study carried out during my internship period at TVP-Solar company will be explained. This chapter focuses on the measurement and performance analysis of a High Vacuum Flat Collectors (HVFPCs) field. The test facility consists of 25 arrays installed on the roof of the TVP-Solar headquarters, serving as a valuable resource for the company to provide customers with collector information. Due to some issues experienced by the company, the objective of this work was to conduct performance measurements of the test field. The aim was to understand the parameters that need to be considered to improve the regulation of the solar field.

The architectural constraints of the building roof have influenced the structure of the installation. The field is divided into two sections, each forming a 6° angle with the horizontal plane. Each set comprises seven panels: four on the east-facing surface and three on the west-facing surface. The tilt angle of each collector in the arrays is set to 15° to maximize energy gain during the summer, with an azimuth angle of 0°.

Initially, performance measurements were conducted using a single pyranometer positioned between the two sides of the roof to measure solar irradiation. Subsequently, two pyranometers, one on the left side and the other on the right side of the roof (both having the same tilt and azimuth as the collectors), were used to measure irradiation independently. A comparison of these measurements with numerical results obtained through dynamic simulation revealed that a comprehensive evaluation of plant performance should account for the varying orientations of the collectors within the arrays. These findings emphasize the importance of considering the impact of collector orientation on system performance, even in cases where ideal orientations cannot be achieved due to installation constraints. Understanding the influence of collector array orientation on system efficiency can guide the development of improved flow rate regulation strategies, leading to enhanced performance and energy utilization.

In the final section of the chapter, the plant simulation model was modified to incorporate the design of HVFPCs equipped with an absorber optimized for operation at 300 °C (as described in Chapter 2). A comparison was initially made by maintaining the same operating temperature as the real case

presented. Subsequently, new results obtained by considering an operating temperature of 200 °C are presented.

4.1 HVFPCS TEST-FIELD DESCRIPTION

This section provides a description of the analyzed HVFPCs test field and detailed information about the installed components. The solar field consists of two main parts.

4.1.1 Solar field

The first part is the Solar Field that is located on the company building's roof and comprises 175 MT-Power HVFPCs. The field is divided into 25 arrays, each containing 7 panels. Within each array, 4 panels are mounted on the east-facing side of the roof, while the remaining 3 panels are situated on the west-facing side. The roof's two sides form a 6° angle with the horizontal plane, as shown in Fig. 4.1.

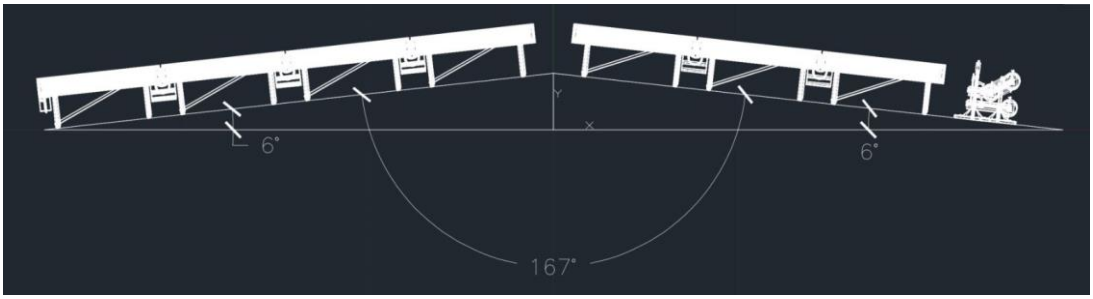

Figure 4.1 Frontal section of one array of collectors of the solar field.

The collectors in the arrays have a tilt angle (β) of 15° and an azimuth angle (γ) of 0°. The collectors of each array are connected in series using hose connectors and are interlinked through supply and return pipelines (Fig. 4.2), while the arrays are connected in parallel. In addition to the supply and return pipes, there is a third pipe that functions as a pressure equalizer. This pipe balances the pressure between the two main pipes to prevent flow reversal in certain rows due to pressure differentials. Furthermore, a vent valve is incorporated into the system to release excess pressure when necessary. The solar field follows a single-side module format, where the pipelines run laterally through the field. The distance between rows of collectors must be chosen by optimizing the available space; usually, the minimum distance is calculated by imposing that there are no shadows at noon on the winter solstice [117] (that is, for a fixed solar altitude: c = (90-23.45-latitude), i.e., at central-southern Italy latitudes, c ≈ 25°), or imposing the absence of shadows at least for solar altitudes higher than a pre-set value (typically 20°):

$$B_{Min} = L * sin(a) * cos(g)/tan(b + c) \quad (4.1)$$

Where B_{min} is the minimum passable distance between two subsequent rows that allows no shadows at noon, c is the solar height, b is the collector's tilt angle, L is the collector's length, g is the azimuth angle of the collectors (fig. 4.3).

Figure 4.2 Solar Field test facility on the roof of TVP-Solar company

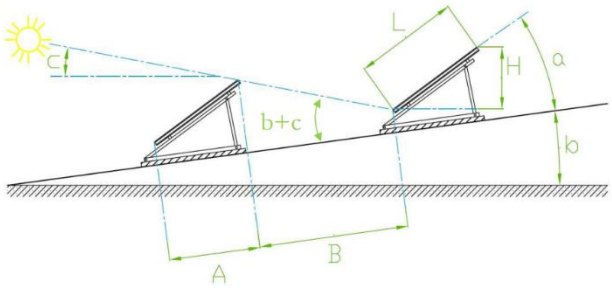

Figure 4.3 schematic representation of two rows of collectors with the characteristic angle indicated.

At ground level, the thermal block consists of two subsystems. Subsystem 1 includes a pressurization pump, an expansion vessel, and a buffer tank. These components work together to maintain the system's pressure within the desired range of 0.6-1.0 MPa, preventing potential evaporation. Subsystem 2 acts as a cooling subsystem for the test facility. As the facility does not have a specific application, the heat transfer fluid (HTF) in this subsystem requires cooling when it reaches the set-point temperature before being recirculated. It comprises an electromagnetic three-way valve and a dry cooler. The purpose of this subsystem is to regulate the field outlet temperature and keep it within pre-set values. When the HTF temperature at the field outlet exceeds the set value, the HTF is directed to the dry cooler for cooling. In the next subsection, a detailed description of the components of the thermal block system will be provided.

4.1.2 Description of the components of the thermal block system

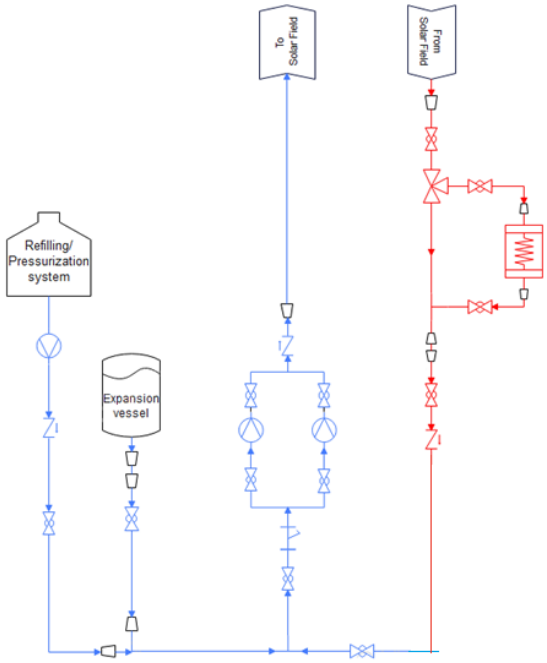

PIPING	
	Process Line
	Line Break
	Ball Valve
	Ball Valve normaly closed
E	Electric Actuated Valve
	Check Valve

	Relief Valve
	3-Ways Valve
	Automatic Air Vent
	Y-Strainer
	Reducer
	Service Outlet
	Pressure Gauge Valve with drain hole

EQUIPMENT	
	Finned Tube
	Dry Cooler
	Pump
	Expansion Vessel

Figure 4.4 P&ID (Piping and Instrumentation Diagram) of the thermal block system of the TVP-Solar HVFPCs test field.

Figure 4.4 depicts the components that compose the thermal block system. In this section, the structure and functionality of each represented component will be explained.

The connections between pipes incorporate various valves:

- Ball valve (Fig. 4.5 (a)): It is a flow control device that utilizes a hollow, perforated, and pivoting ball to regulate the liquid flow. In the solar field, this valve is installed in both the return and supply pipelines of each row. Its main function is to disconnect the row from the circuit during maintenance interventions.
- Check valve (Fig. 4.5 (b)): A check valve, also known as a non-return valve or one-way valve, allows fluid to flow through it in only one direction.
- Pressure relief valve (PRV) (Fig. 4.4 (c)): This safety valve is used to control or limit the pressure in a plant system. Its opening is proportional to the pressure increase in the tank.
- Automatic air vent valves (Fig 4.5 (d)): These valves are employed to eliminate air from heating systems. The presence of air can lead to corrosive phenomena, cavitation, and reduced heating system efficiency. When the air level in the float chamber exceeds a certain threshold, the valve opens, releasing the trapped air and allowing water to replace it.
- Y-strainer (Fig. 4.5 (e)): Its purpose is to remove unwanted particles from steam, gas, or liquid by using a straining element typically made of wire mesh.
- Reducers (Fig. 4.5 (f)): A reducer is a kind of pipe fitting (accessory) that is used in process piping to change the pipe size from a big bore to a smaller bore pipe. Mostly reducer is used for a change in pipe size to meet flow requirements of the process system or connect to existing small or big piping bores as per requirements. The length dimension of the reducer is almost equal to the average of the big bore and smaller bore pipe diameters.
- Line break valves (Fig. 4.5 (g)): These anti-pollution devices prevent backflows and the contamination of water with chemicals or bacteria. Under normal conditions, the valves are open, permitting fluid passage. However, if the upstream pressure drops due to a pipe fault, the negative pressure automatically closes the valves, preventing backflow and opening the discharge valve to empty the intermediate zone. These valves are essential after the pumps as they act as non-return valves.
- Three-way valve (Fig. 4.5 (h)): This valve is a constant flow rate and is a constant flow rate valve used for either mixing or diverting applications. In these valves, the total flow rate remains constant. These valves have three pipe connections and two orifices. When one orifice is open, the other is closed, and vice versa. These valves can be normally closed, normally open, or universal. They come with a T- or L- shaped fluid passageways inside the rotor. The T valve might be used to permit the connection of one inlet to either or both outlets or the

connection of the two outlets. The L valve could be used to permit disconnection or connection of both, but not both of two inlets to one outlet.

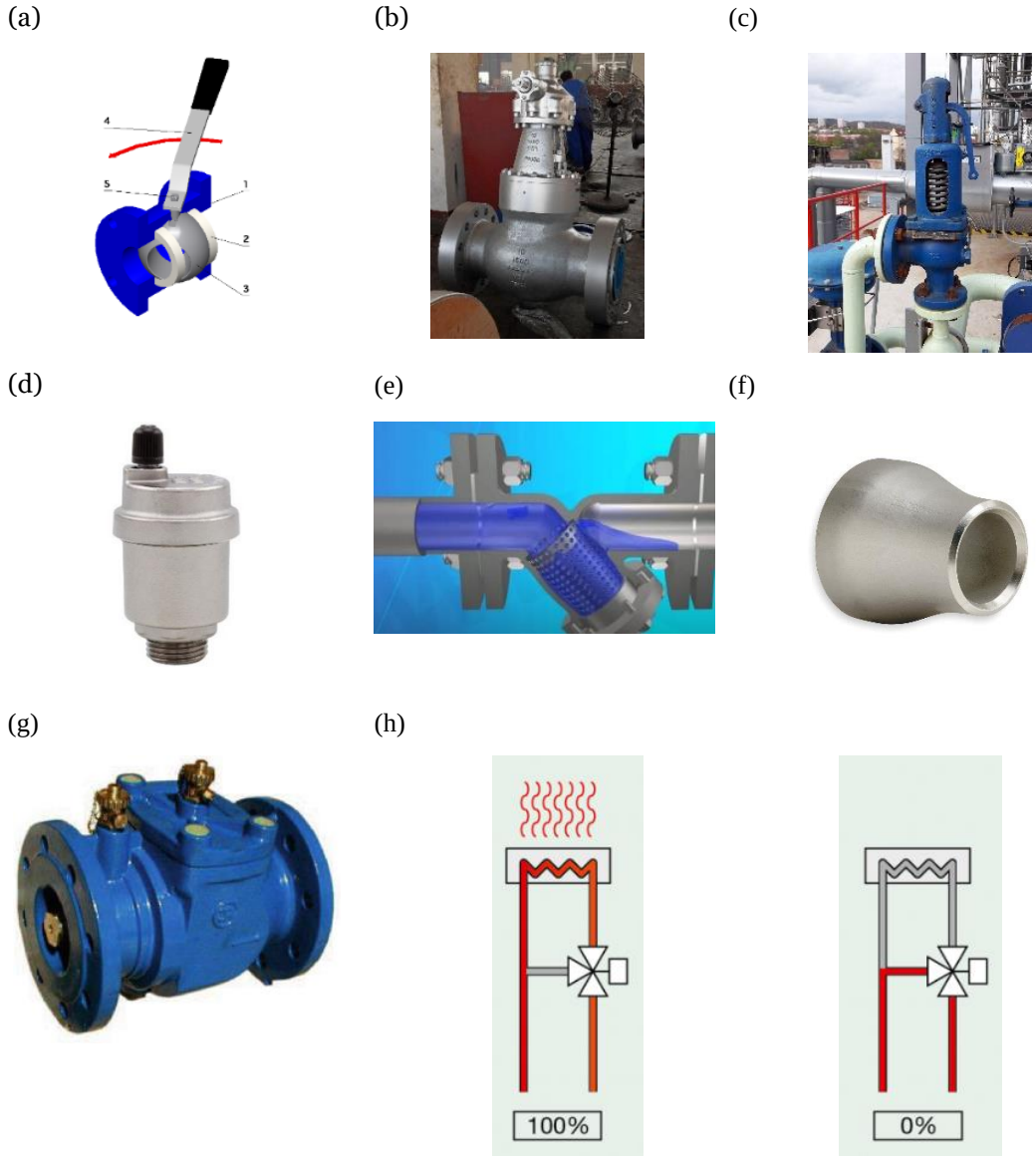

Figure 4.5 Type of valves in the HVFPs Field : (a) ball valve; (b) check valve; (c) Pressure relief valve; (d) automatic air vent valve; (e) Y-strainer; (f) concentric reducer; (g) line break valve; (h) three-way valve

The circulation of the Heat Transfer Fluid (HTF) in the solar field circuit is ensured by the Solar Field Circulation Pump, which is a specialized pump used for circulating gases, liquids, or slurries in a closed circuit. In this case, it is used to circulate the HTF in the plant's hydronic system. Since it only circulates liquid within a closed circuit, its main challenge is to overcome the friction of the piping system and, if necessary, lift the fluid from a lower potential energy point to a higher one (for instance, pumping the fluid to the top of a building if the solar field is installed there). The primary function of the pump is to regulate the flow rate. The system must always operate smoothly, meaning that the

flow temperature, coming from the solar field, should reach the designated operating value. To achieve this, considering the variability of solar thermal availability, the flow rate is adjusted accordingly by controlling the Programmable Logic Controller (PLC) Cabinet.

The gas exerts pressure on the membrane, establishing a pre-charge pressure for the circuit. This ensures that even the highest elements and pipes in the system are maintained at the operating pressure. Without this pressure surplus, the highest parts of the system would be exposed to atmospheric pressure, which could lead to undesired HTF evaporation and the formation of air pockets in the upper sections of the system. It is recommended to install expansion vessels on the pipeline containing the lowest temperature water, which, in this case, should be on the return pipe. This is because the gas permeability of the membrane increases with higher temperatures, potentially causing the presence of gas in the circuit.

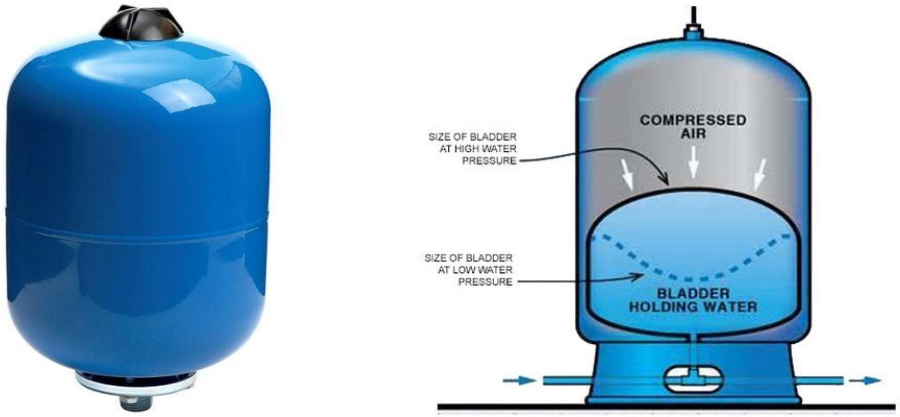

Figure 4.5 Diaphragm membraned expansion vessel

In the thermal block P&ID, there is a system referred to as the Refilling System/Pressurization Pump. This system utilizes a suitable pump to refill the circuit when it has experienced a loss of fluid. The reduction in the liquid level within the circuit can occur due to natural micro-leaks that develop over time, requiring occasional refilling, or it can be a result of pipe ruptures or malfunctioning valves.

Dry coolers are air/water-finned heat exchangers. They are employed in this type of plant to cool the HTF flow using ambient air when the heat level exceeds the required threshold and poses a risk to the circuit's integrity. In particular, when the temperature of the HTF exceeds the system design temperature, the flow is directed through the dry cooler using a three-way valve (Figure 4.6 (b)). When this occurs, the control system typically increases the load on the circulation pump to maximize the flow rate and manage the sensible heat, thereby reducing the fluid temperature. If the fluid temperature remains higher than the maximum operating temperature despite the maximum flow rate, the dry cooler is activated. It is a straightforward and easy-to-install system. The cooling capacity is

enhanced by fans that facilitate the movement of air across the pipes and increase the convective heat transfer coefficient.

(a) (b)

Figure 4.6 Dry cooler of the HVFPCs field thermal block: (a) picture of the dry cooler installed at ground level ; (b) schematic representation of the dry cooler and its circuit.

The size of the dry cooler is determined based on the mass flow rate circulating in the system and the desired return temperature. Generally, when the dry cooler is activated, the fluid is cooled to the return temperature of the solar field. It is a device that is unlikely to become blocked, and although necessary for safety reasons, its activation results in energy wastage. For this reason, the plant should be designed in the most efficient way possible to minimize the frequency of dry cooler activation events. In this particular test field, the Heat Transfer Fluid (HTF) currently does not have a designated application. As a result, the dry cooler serves as a substitute for a potential heat exchanger that is typically utilized on the application side of the solar field circuit.

4.1.3 Field control by PLC (Programmable logic controller)

The PLC Cabinet, also known as a Programmable Logic Controller, plays a crucial role in regulating all operational parameters through an HMI (Human-Machine Interface). This interface serves as a communication dashboard between humans and machines.

The PLC system facilitates control over various components, including electronically actuated valves and pump inverters, allowing for the adjustment of the flow rate and more.

In the context of the HVFPCs field, the PLC receives signals from sensors installed within the system. These sensors provide essential measurements related to the operating conditions of the Heat Transfer Fluid (HTF) and weather data. Table 4.1 presents a comprehensive overview of the signals received by the PLC, excluding those from the electronic valves. Additionally, the table provides details about the respective sensors responsible for generating these measurements.

Tab. 4.1 PLC input signals from the HVFPCs field, description, and sensor details

ID	TYPE	Description	Sensor	Model
TT-001	Temperature	Field return temperature on 3-way field loop valve	Thermometer PT-100	Easy temp TMR35
TT-002	Temperature	Field supply temperature	Thermometer PT-100	Easy temp TMR35
TT-003	Temperature	Dry cooler supply temperature	Thermometer PT-100	Easy temp TMR35
TT-004	Temperature	Dry cooler return temperature	Thermometer PT-100	Easy temp TMR35
TT-005	Temperature	Weather temperature	Air temperature sensor (PT100 trasducer)	MTX FAR039 BA
PT-001	Pressure	Solar field pump inlet pressure	Piezoresistive pressure transmitter	KELLER series 21/21 PRO
PT-002	Pressure	Solar field pump outlet pressure	Piezoresistive pressure transmitter	KELLER series 21/21 PRO
PT-003	Pressure	Expansion vessel liquid side pressure measure	Piezoresistive pressure transmitter	KELLER series 21/21 PRO
FT-001	Flow	Solar field flow measure	Electromagnetic flowmeter	Promag P100
LC-001	Level	Field water storage tank level	Level sensor	Autosen AF903
IT-001	Irradiance	Meteo station Irradiance measure	Pyranometer	MTX PCTRA0xx

The PLC can operate in either "Automatic mode" or "Manual mode." However, due to the absence of a real application, it is challenging to achieve automatic regulation in this test field. Nevertheless, the logical functioning of the system will be explained as follows:

1. Pre-heating Mode: This mode operates in the morning, from sunrise to sunset, when the conditions are suitable for the pump to activate (Irradiation ≥ Threshold value). Once the desired temperature is reached, the system transitions, if activated, to the next mode.
2. De-freezing Mode: This mode prevents the fluid inside the system from freezing. During the night or during the day when the irradiation and system temperature are below the set values, the solar field pump turns on, facilitating fluid movement and preventing liquid solidification. The pump switches off when the system temperature reaches an upper limit.
3. Dry cooler Mode: This mode is activated when the system temperature exceeds the design value. In such cases, the three-way valve (previously described) directs all the fluid to the "dry cooler," which brings the system temperature back below the predefined limit.

4. Automatic Refill: This mode prevents the system from running out of fluid in the event of a leak. If the system pressure falls below a set value due to a hydraulic circuit fault, an electro-actuated valve opens fully, activating the pressurization pump to refill the system until it reaches the normal operating pressure. It is advisable to perform system maintenance when the reintroduced fluid quantity reaches a critical value.

Due to some issues experienced by the company, the objective of this work was to conduct performance measurements of the test field in manual mode under controlled conditions. The aim was to understand the parameters that need to be considered to improve the regulation of the solar field.

4.2 PERFORMANCE MEASUREMENTS OF TVPSOLAR HVFPCS FIELD

The objective of the performance measurements conducted on the solar field was to monitor its daily productivity and field efficiency. Water was chosen as the Heat Transfer Fluid (HTF), and the set-point temperature for each measurement day was determined accordingly. To assess the field's performance, several quantities were measured, including HTF temperatures at the inlet and outlet of the solar field and dry cooler, HTF flow rates at the inlet of the solar field and dry cooler, solar irradiation, and ambient temperature.

Initially, the measurement campaign focused on monitoring solar irradiation using a single pyranometer installed in the middle of the roof. A fixed HTF flow rate of 8 m^3/h was maintained, and the measurement results were compared with numerical results obtained from a simulation model implemented in Simulink. However, discrepancies between the measured and simulated results led to a repeat of the measurement campaign.

In the subsequent measurements campaign, solar irradiation was monitored separately on each side of the building roof using two pyranometers (Fig. 4.7). This arrangement aimed to capture localized variations in solar irradiation across the roof. The flow rate regulation took into account the average value of irradiation measured by the two pyranometers. The measurements were conducted when the solar irradiation (G) was greater than or equal to 150 W/m^2 to cover the full range of solar illumination.

By measuring throughout the entire daylight period, the differences in solar radiation received by the collectors due to their different orientations (east-facing and west-facing sides of the roof) could be accurately assessed. The results obtained from both measurement configurations, along with the analysis derived from them, will be presented subsequently.

The flow rate regulation aimed to maintain the set-point temperature while incorporating the localized variations in solar irradiation across the roof. The measurement results included weather conditions such as solar irradiation (G) measured by the pyranometers and ambient temperature (T_{amb}).

Figure 4.7 Arrangement of the two pyranometers for the second measurements campaign.

4.2.1 Results of experimental measurements conducted with single pyranometer configuration.

Figure 4.8 presents the measurement results obtained during a single day of the measurement campaign, where solar irradiation was monitored using a single pyranometer positioned in the middle of the building roof. The selected day for presenting the results is March 18th, 2023, with a set-point temperature (field outlet) of 95 °C, which is a typical application temperature for a solar thermal field. In Figure 4.8(a), the recorded weather conditions are depicted, including the solar irradiation (G) measured by the single pyranometer and the ambient temperature (T_{amb}).

In Figure 4.8(b), the performance parameters of the solar field are presented. The temperature difference (ΔT) represents the increase in HTF temperature achieved by the solar field. The observed oscillations in ΔT are attributed to incorrect flow rate and dry cooler power regulation.

P_{inc} (W) represents the solar power incident on the surface of the collectors comprising the solar field. It is calculated using the formula (1):

$$P_{inc} = G * A_c * N_c \quad (4.1)$$

Where A_c represents the collector surface, N_c is the number of panels of the solar field, and P_{conv} (W) represents the amount of power converted by the solar field while maintaining the set-point temperature. It is computed using the formula (4.2):

$$P_{conv} = \dot{m} * c_p * \Delta T \quad (4.2)$$

(a) (b)

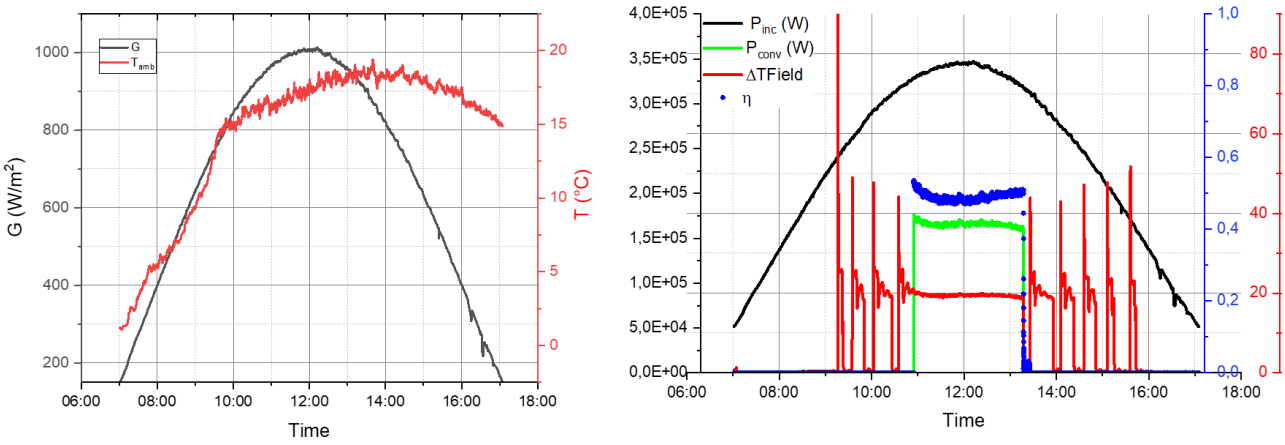

Figure 4.8 (a) 18/03/2023 acquired weather data, solar irradiation (black line, left scale), and ambient temperature (red line right scale) ;(b) Measured field performance parameters with a set point temperature equal to 95 °C: incident power, produced power, ΔT and efficiency.

η is the field efficiency and in the graph is represented for a set point operating temperature of 95 °C and (T_{avg}-T_{amb}) of approximately 70 °C. It is computed using the formula:

$$\eta = \frac{P_{conv}}{P_{inc}} \tag{4.3}$$

The measurements conducted with the single pyranometer configuration resulted in a conversion efficiency of η = 0.5. However, it was observed that the collectors mounted on the east side of the roof received better illumination in the morning compared to those on the west side. These variations in collector exposure throughout the day introduce discrepancies in the heating and cooling of the HTF, emphasizing the need for separate monitoring of solar irradiation on each side of the roof.

4.2.2 Results of experimental measurements conducted with double pyranometer configuration.

Regarding the results of the experimental measurements conducted with a double pyranometer configuration, Figure 4.9 displays the results obtained on a specific day (July 9, 2023). Solar irradiation was monitored using the double pyranometer configuration. The set-point temperature was maintained at 100 °C. The solar irradiation measurements were recorded from the east-facing pyranometer (Gest) and the west-facing pyranometer (G_{west}). In this case, the HTF flow rate (depicted in Figure 4.9 (a)) is regulated to maintain the set-point temperature while providing a specific cooling power for the dry cooler. In Figure 4.9 (b), P_{inc} represents the sum of solar power incident on the collectors positioned on the east-facing side of the roof (G_{est} * A_c * N_{c_est}) and the solar power incident

on the collectors mounted on the west-facing side of the roof ($G_{west} * A_c * N_{c\_west}$), where $Nc_{\_est}$ and N_{c_west} are the number of collectors mounted on the east and west facing side of the roof respectively.

(a) (b)

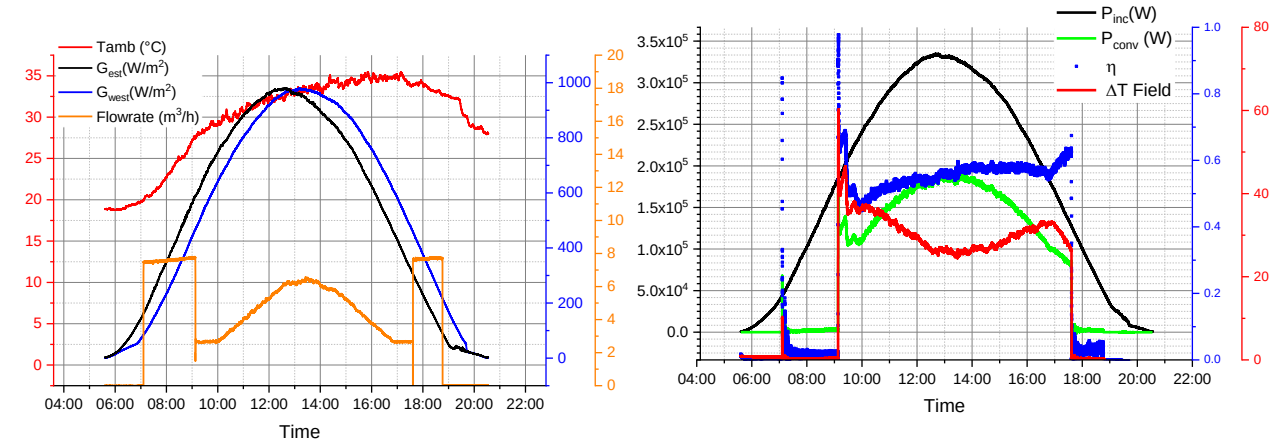

Figure 4.9 (a) 9/07/2023 acquired weather data, and flow rate (b) Measured field performance parameters with a set point temperature equal to 100 °C.

In the analyzed HVFPC field operating at 100 °C, the measurements revealed a daily average conversion efficiency of 56% under an average irradiation of G_{avg} =650 W/m^2. These results are considered, especially when compared to the findings in reference [118]. In that study, an 800 m^2 solar thermal plant coupled to a District Heating system in Geneva was monitored for over a year. The solar field comprised 400 MT-Power collectors and achieved a yearly efficiency of 46.4% with an average operating temperature above 80°C.

These findings indicate that the HVFPCs in the analyzed field are highly efficient and capable of generating significant thermal energy output even under varying irradiation conditions.

4.3 HVFPCs Field performances: comparison between numerical and experimental results.

Similar to the dynamic model developed for the individual HVFPC performance assessment in Chapter 3, a dynamic model of the TVPSolar HVFPC field test facility was implemented in Simulink. The simulation model was validated using the daily experimental measurements reported earlier.

The solar field installed at TVPSolar Seath will soon be used to test new versions of HVFPCs equipped with SSAs that have improved optical properties. A daily dynamic simulation was implemented and executed to assess the performance of the solar field with these new HVFPCs.

Similar to the test bench simulation, the dynamic model treats the collector as a box, with its behavior mathematically described by an efficiency expression. To simulate the behavior of MT-Power field, the standard efficiency expression (eq. 1.15) was used and, by utilizing the efficiency model formulation presented in Chapter 2, it is possible to reconstruct the efficiency expression of the new version of HVFPC equipped with an optimized SSAs but with the same architecture as MT-Power.
The last section of this chapter will present the results of a dynamic simulation illustrating the daily production of a solar field operating at a temperature of 200 °C, equipped with SSAs optimized to operate at 300 °C, as discussed in Chapter 2.

4.3.1 TVPSolar HVFPCs field dynamic simulation model description.

In order to simulate the solar field, Simulink with the Simscape library was chosen as the simulation model, enabling the modeling and simulation of physical systems in a multidomain environment. Similar to the Test-Bench model (Chapter 3), the solar field was divided into multiple subsystems, mirroring the subsystems described in Section 4.1.
The "Solar Field" subsystem (Fig. 4.10(a)) represents the 25 collector strings, with each string depicted as a single block. The number of collectors within each string is provided as input. The strings are connected in parallel (Fig. 4.10(b)), as indicated by the connection to the supply and return pipes at the input and output of each block (Fig. 4.10(c)). The required inputs for this subsystem are solar irradiation and ambient temperature. Additionally, there is a block that models the connecting pipes for fluid circulation.
The "Thermal Block" system is represented in Fig. 4.11. In the simulation model, the dry cooler and the expansion vessel are modeled as separate subsystems. In the thermal block, elements that regulate the heat transfer fluid (HTF) circulation, such as the circulating pump and two 3-valves, are included (Fig. 4.11(b)). The valve switch temperatures can be manually adjusted in the block interface, while the flow rate must be provided as a vector input to the pump block.
In addition to the "solar field" subsystem, the "Thermal Block" is connected to the "expansion vessel" (Fig. 4.12(a)) and "dry cooler" (Fig. 4.12(b)) subsystems. The "expansion vessel" is modeled using the Simscape library's "gas-charged accumulator" element. It consists of a precharged gas chamber, and a liquid chamber connected to a thermal liquid network. The chambers are separated by a bladder, piston, or diaphragm. To design the element, the volume of the accumulator and the pre-charge pressure must be provided. The "dry cooler" is modeled as a heat exchanger between the thermal liquid network and the moist air network. The block's dimensions correspond to the actual dry cooler installed in the solar field, and the cooling power is adjusted by controlling the cooling air velocity, which is used as an input to the block.

The simulation model contains also blocks in which the signals are elaborated to provide in output the numerical physical quantities required.

(a) (b)

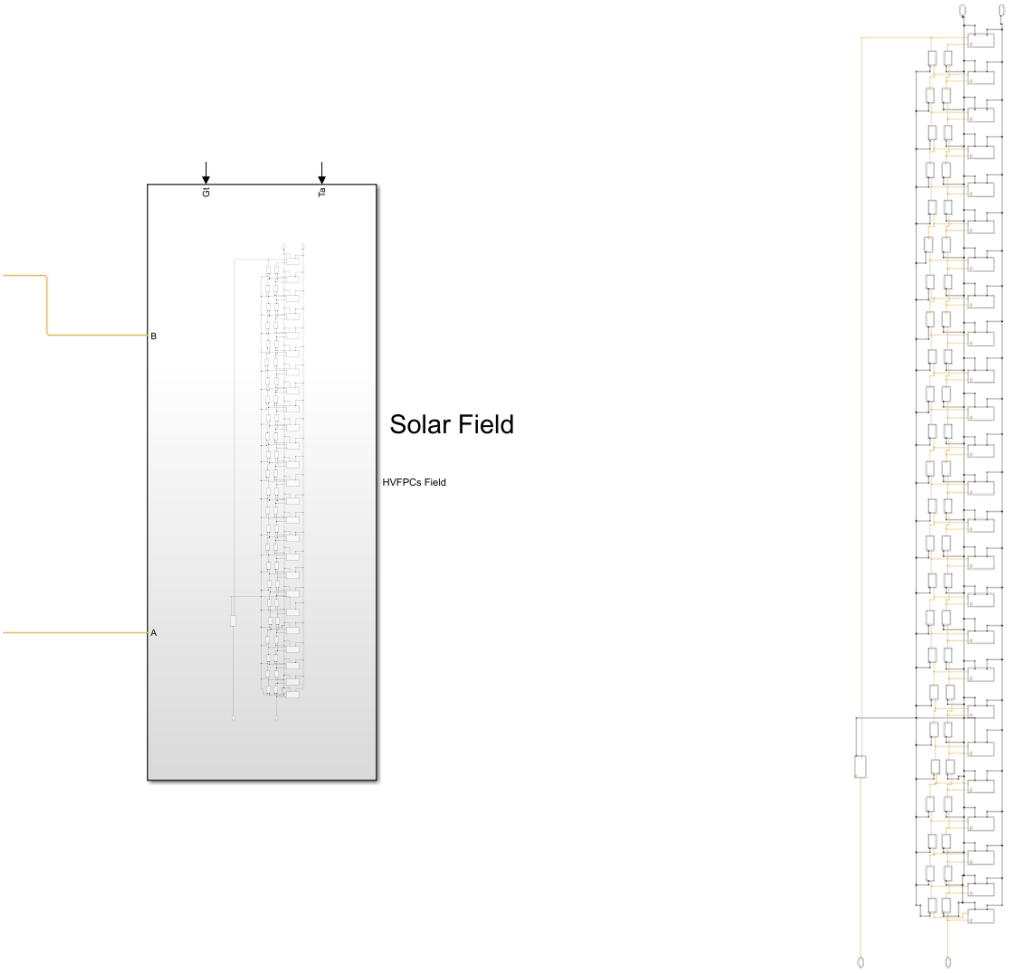

(c)

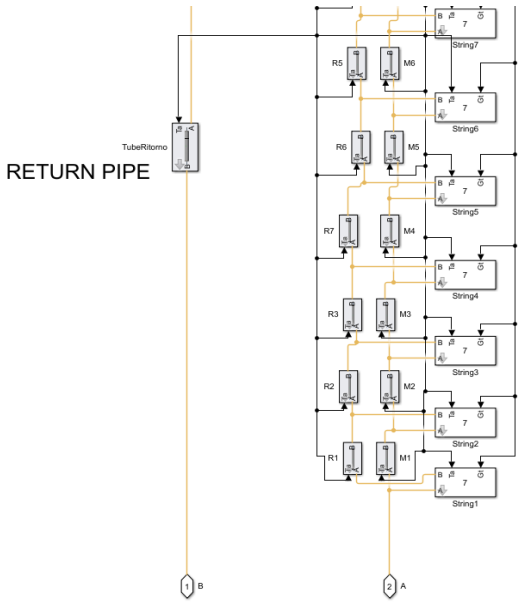

Fig. 4.10 Solar Field subsystem: (a) simulation model of the solar field subsystem; (b) structure of the block with the 25 arrays connected in parallel; (c) zoomed-in view of Fig. (b) showing the solar field return pipe block.

(a)

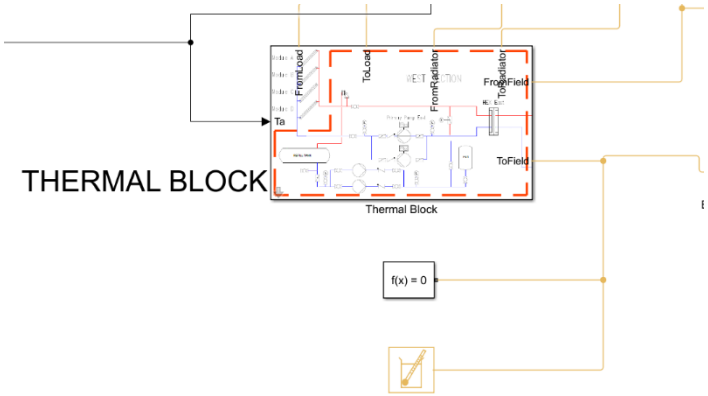

(b)

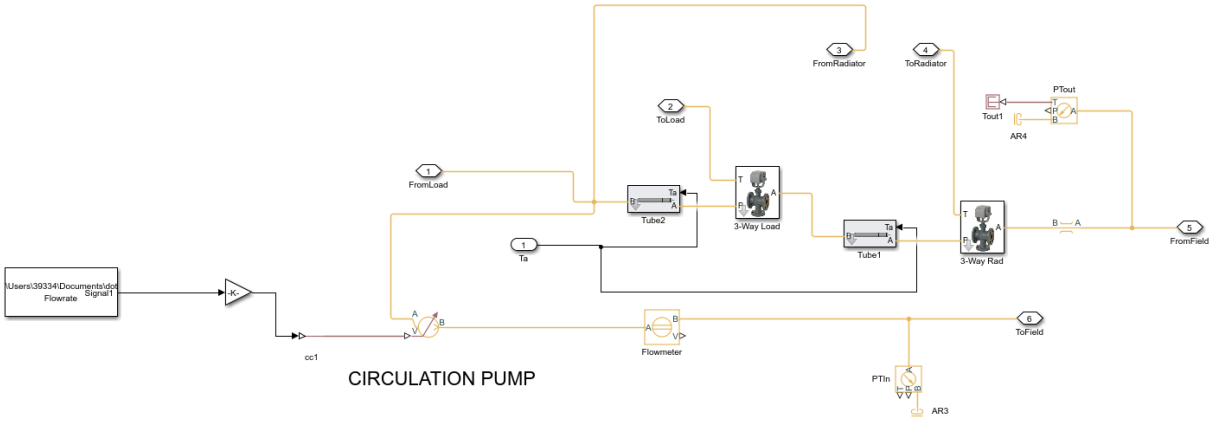

Fig 4.11 "Thermal Block" subsystem: (a) user-defined block; (b) structure of the subsystem with the circulating pump, the flowmeter connected to the pump, the two 3-way valves and the connection with the circuit with the pressure & temperature sensor block at the outlet.

(a)

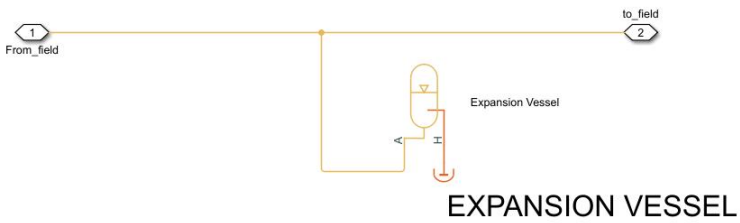

(b)

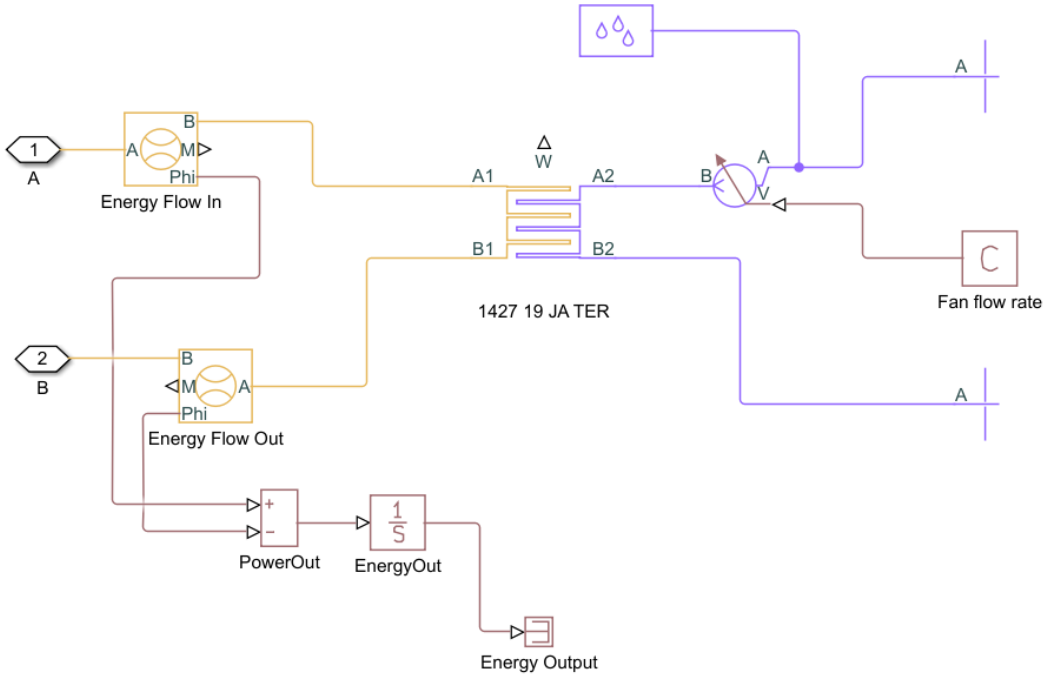

Fig 4.12: (a) “Expansion vessel” susbsystem; (b) structure of the “dry cooler” subsystem

4.3.2 HVFPCs test-field performance daily simulation: comparison between numerical and experimental results.

The measurements campaign presented in Section 4.2 was compared to the numerical results obtained from the simulation model of the solar field implemented in Simulink. The simulation takes into account various input parameters, including the HTF mass flow rate, solar irradiation, ambient temperature, set-point temperature, and dry cooler air flow rate for controlling the cooling power. To maintain consistency with the actual case, water was used as the circulating HTF with the same flow rate.

Therefore, the comparison between the numerical and experimental results focused on the comprehensive performance parameter, ΔT, achieved by the solar field.

Figure 4.13 (a) depicts the comparison between the measurements taken with the single pyranometer configuration on the 18th of March and the numerical results. Specifically, it shows the average HTF temperature, T_{avg}, which is obtained by taking measurements between the inlet and outlet of the field, and the ΔT achieved by the field. The numerical results tend to overestimate both the ΔT and T_{avg} provided by the solar field. Moreover, when examining the trend of T_{avg}, significant differences are observed, particularly at the beginning and end of the day during the field's warming up phase.

(a) (b)

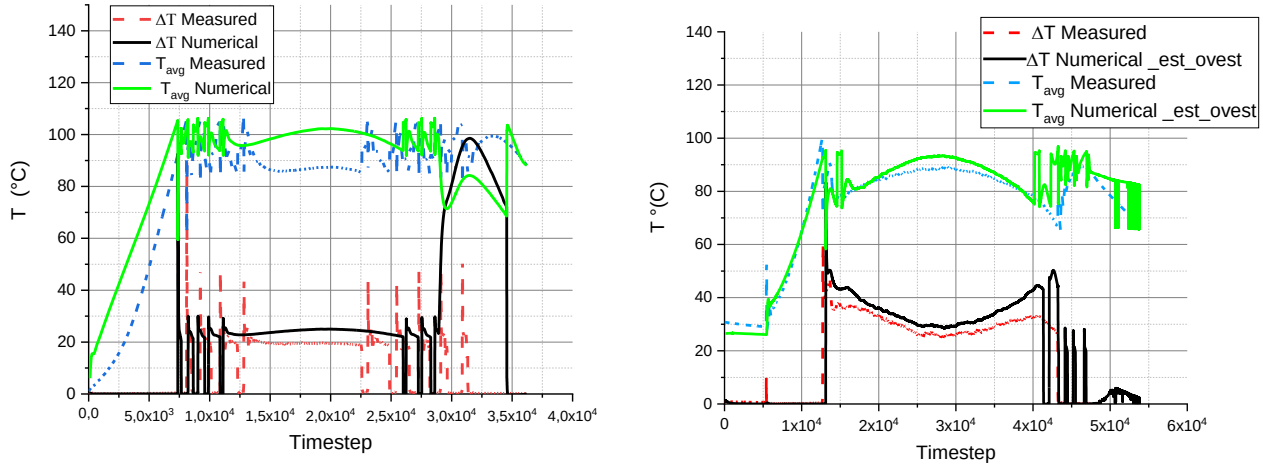

Fig. 4.19 Comparison between experimental & numerical results: (a) Measured ΔT (red dashed line) and the T_{avg} (blue dashed line) of the first experimental campaign carried out with single pyranometer configuration (18 March 2023) and comparison with simulation results (black and green solid lines respectively); (b) Measured ΔT and the T_{avg} of the second experimental campaign carried out with double pyranometer configuration (9 July 2023) and comparison with simulation results

These discrepancies can be attributed to variations in collector exposure within each array. For example, collectors mounted on the east side of the roof receive better illumination in the morning compared to those on the west side. These variations in collector exposure throughout the day introduce differences in the heating and cooling of the HTF, emphasizing the need for separate monitoring of solar irradiation on each side of the roof. In Figure 4.13(b), the comparison between the measurements and numerical results of the double pyranometer experimental campaign on the 9th of July is illustrated. In this case, the simulation results differ from the experimental measurements by approximately 5%, compared to the 25% difference observed in the previous experimental configuration. When observing the trend of T_{avg} in Figure 4.13 (b), it is noticeable that the numerical T_{avg}, calculated using the incident power data from Figure 4.9 (a), closely reproduces the experimentally measured HTF heating curve. Furthermore, the oscillations observed after the solar field reaches its operating temperature are significantly reduced, highlighting the importance of considering the different illuminations of collectors for flow rate regulation. The graphs are presented based on the simulation timestep, and each timestep corresponds to the sampling interval of the measurements acquisition.

4.3.3 Daily performance forecasts of HVFPCs equipped with optimized SSA field.

The comparison between experimental and numerical results presented in the previous section highlighted how the behavior of the analyzed solar field can be accurately reproduced numerically only by considering the differential illumination received, especially during the early and late hours of the day, by the collectors mounted on the east side compared to those mounted on the west side.

To conclude the discussion initiated in this thesis work and summarize the acquired and presented tools, it was chosen to simulate the behavior of the same test field as if it were equipped with HVFPCs fitted with the optimized OPT_{300} absorbers presented in Chapter 2 and having the same architecture as the MT power (thus, the same conductive losses). It has been demonstrated how it was possible to derive the efficiency formula for HVFPCs potentially equipped with optimized SSAs. In this case, since the panels are mathematically described by their efficiency in the simulation model, the newly formulated model was used to obtain numerical results by inputting the meteorological data acquired during the measurement conducted with the configuration that includes the two pyranometers. First, the simulation was conducted by replicating the same conditions as the case of the field composed of MT-Power HVFPCs. Subsequently, the behavior of HVFPCs equipped with the optimized version of the absorber was simulated, imposing a set point temperature of 200°C. In this case, the diathermic oil Therminoil 66 was selected as the HTF. In both cases, the mass flow rate was set equal to the real case. The power of the radiator was adjusted to maintain the operating temperature without significant fluctuations for most of the day.

Figure 4.20 displays the simulation results for the operating day of July 9th, considering two cases: panels with a commercial absorber and panels with the OPT300 absorber, with a set-point outlet temperature of 100°C. In this case, the results are very similar. The, ΔT realized, so the output energy provided by the solar field, in the case of HVFPCs equipped with optimized SSA, is lower that the energy produced by the HVFPCs equipped with commercial absorber at the selected set- point outlet temperature. This is because, at 100°C, the efficiency of the panel with the optimized absorber is slightly lower than that of the panel with the commercial absorber.

Figure 4.21 presents the results of the daily simulation (July 9, 2023) of the HVFPC field, considering the version equipped with optimized absorbers but setting a set-point outlet temperature of 200°C. To avoid operating the field at excessively high pressures, which would require modifications to some system components, the simulation was conducted using Therminol 66 diathermic oil as the heat transfer fluid.

In Figure 4.21 (a), the plot shows the variation of the provided temperature difference (DT) and the average fluid temperature during the simulation. In Figure 4.21 (b), the graph displays the total daily energy generated by the field. Despite 200°C being a relatively high operating temperature for a flat plate collector, the field performs well even at these temperatures (958 kWh produced in the selected day), achieving a conversion efficiency of approximately 40%. Having a simulation model of the field that allows for evaluating its performance even in the case of HVFPCs with optimized absorbers will be beneficial for future developments.

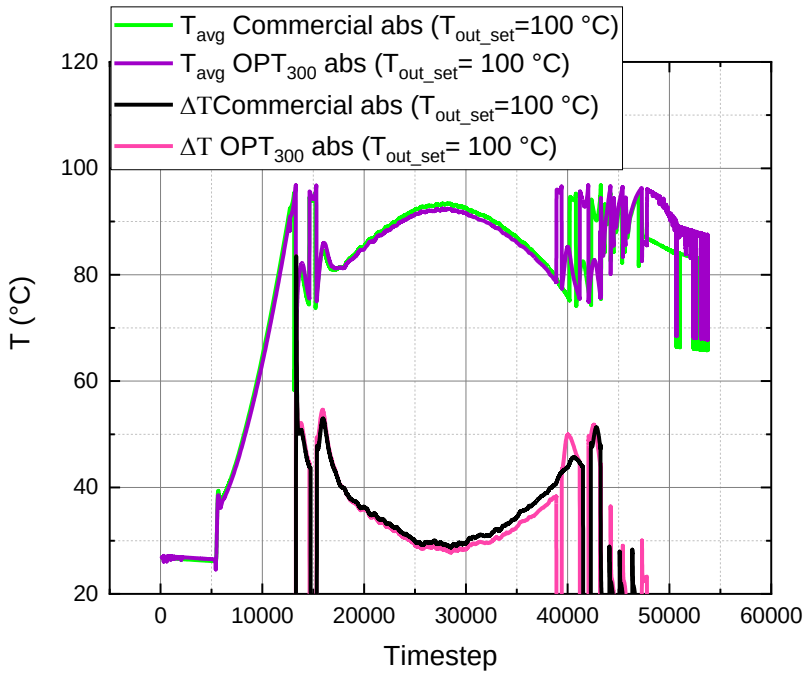

Fig. 4.20 Numerical results of daily simulation for the operating day of July 9th: ΔT realized by the solar field of HVFPCs equipped with commercial (black line) and OPT_{300} (pink line) SSAs; HTF field average temperature T_{avg} trend during operation in the case of HVFPCs equipped with commercial (green line) and OPT_{300} (violet line) SSAs;

(a) (b)

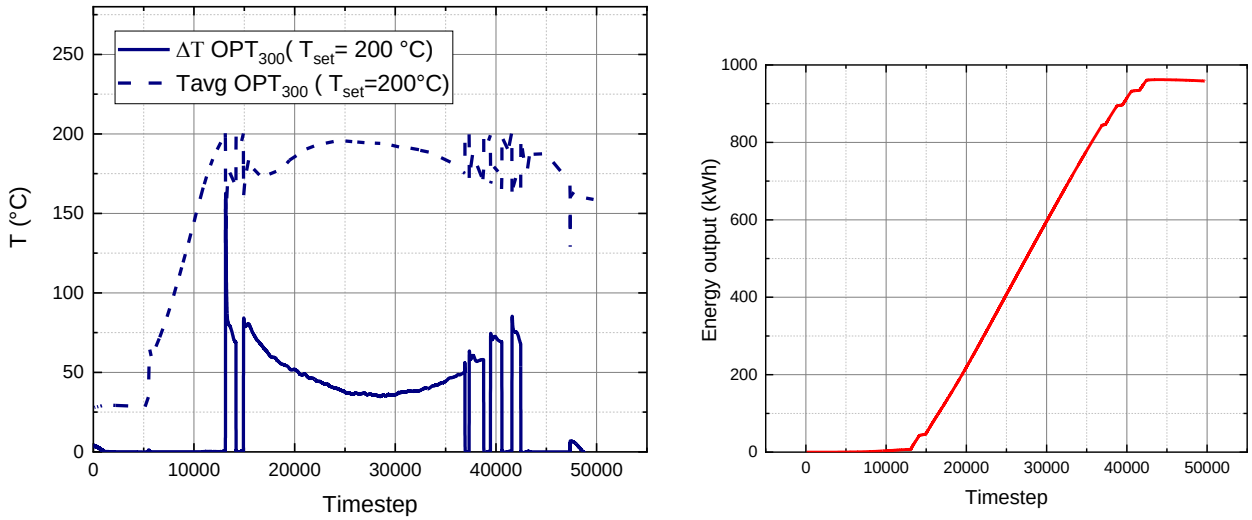

Fig 21 results of the daily simulation (July 9, 2023) of the HVFPC field, considering the version equipped with OPT_{300} SSA with a set-point outlet temperature of 200°C. (a) ΔT and T_{avg} ;(b) output energy produced by the HVFPCs field

The company plans to replace the current HVFPCs installed in the test field with the optimized version and configure the system to reach even higher temperatures. The simulation model will support the design of a control strategy for adjusting operational parameters to maximize energy output. Additionally, a stratified tank will be added to the field in the future to connect it to a practical application. We are currently designing the model for this tank in collaboration with our research group.

5. CONCLUSIONS

In conclusion, this thesis has comprehensively addressed the key aspects of HVFPC (High Vacuum Flat Plate Collector) technology and its optimization for enhanced performance. Through rigorous research and experimentation, valuable insights have been gained into the design, fabrication, and characterization of selective solar absorbers (SSAs) specifically tailored for HVFPCs. The optimization of SSAs has been a primary focus of our research group's work in recent years, resulting in significant advancements in improving their optical properties and efficiency within HVFPC systems. These advancements contribute to the overall enhancement of HVFPC performance, enabling more effective and efficient utilization of solar energy. In particular, the investigation of novel SSAs with substrates coated with low emissive materials has been pursued, and the corresponding optical characterization procedures have been updated to cater to this specific objective.

A crucial objective of this research was to establish a performance forecasting framework specific to this optimized HVFPC technology, thereby creating a standardized approach distinct from the one adopted for conventional flat collectors and bridging the literature gap. As such, a new efficiency model for HVFPCs has been formulated and validated. This model enables precise performance characterization of HVFPCs while considering variations in the optical properties of the absorber. Unlike the standard efficiency formulation used for flat collectors, the new model explicitly accounts for radiative losses, the primary source of efficiency reduction in HVFPCs, thereby facilitating efficiency evaluation even at stagnation temperatures.

Another significant objective of this work was to evaluate the temperature frequency function of the HVFPC absorber, a critical parameter in determining the collector's service lifetime. Through the utilization of experimental data and a validated dynamic simulation model, the performance of the MT-Power HVFPC absorber and its aging characteristics were successfully assessed. This information plays a crucial role in accurately estimating the longevity and reliability of thermal collectors in practical applications.

The experimental apparatus and simulation model developed throughout this research have played a pivotal role in supporting our investigations. These tools have enabled precise analysis and evaluation of HVFPCs, providing valuable insights into their behavior under varying operating conditions. The knowledge gained from these experiments and simulations paves the way for further advancements in HVFPC technology.

In summary, the results achieved throughout this doctoral journey contribute to the culmination of a project initiated in preceding years, aimed at establishing High Vacuum Flat Plate Collectors as one of the most competitive technologies for sustainable heat production in medium-temperature

applications. The optimization process for this technology has been continually pursued, resulting in the provision of effective evaluation and energy forecasting tools applicable to diverse conditions and locations. Mathematical models and dedicated procedures have been developed and formulated, and the acquired knowledge has been practically applied during a case study conducted during the internship period at TVPsolar company.

6. BIBLIOGRAPHY

[1] A. Sayigh, «Renewable energy — the way forward», *Applied Energy*, vol. 64, fasc. 1–4, pp. 15–30, set. 1999, doi: 10.1016/S0306-2619(99)00117-8.

[2] W. Puntoon, P. Tarkhamtham, e R. Tansuchat, «The impacts of economic growth, industrial production, and energy consumption on CO2 emissions: A case study of leading CO2 emitting countries», *Energy Reports*, vol. 8, pp. 414–419, dic. 2022, doi: 10.1016/j.egyr.2022.10.219.

[3] «IEA (2020), World Energy Statistics and Balances 2020 (database)».

[4] «United States Environmental Protection Agency».

[5] G. P. Thiel e A. K. Stark, «To decarbonize industry, we must decarbonize heat», *Joule*, vol. 5, fasc. 3, pp. 531–550, mar. 2021, doi: 10.1016/j.joule.2020.12.007.

[6] G. K. Singh, «Solar power generation by PV (photovoltaic) technology: A review», *Energy*, vol. 53, pp. 1–13, mag. 2013, doi: 10.1016/j.energy.2013.02.057.

[7] L. Kumar, M. Hasanuzzaman, e N. A. Rahim, «Global advancement of solar thermal energy technologies for industrial process heat and its future prospects: A review», *Energy Conversion and Management*, vol. 195, pp. 885–908, set. 2019, doi: 10.1016/j.enconman.2019.05.081.

[8] S. Sadhishkumar e T. Balusamy, «Performance improvement in solar water heating systems—A review», *Renewable and Sustainable Energy Reviews*, vol. 37, pp. 191–198, set. 2014, doi: 10.1016/j.rser.2014.04.072.

[9] J. Huang, J. Fan, S. Furbo, e Q. Li, «A policy study on the mandatory installation of solar water heating systems – Lessons from the experience in China», *Solar Energy*, vol. 206, pp. 614–627, ago. 2020, doi: 10.1016/j.solener.2020.06.049.

[10] N. Monghasemi e A. Vadiee, «A review of solar chimney integrated systems for space heating and cooling application», *Renewable and Sustainable Energy Reviews*, vol. 81, pp. 2714–2730, gen. 2018, doi: 10.1016/j.rser.2017.06.078.

[11] J. Zheng, T. Yu, B. Lei, e R. Lv, «Study on the influencing factors of thermal performance of radiant heating floor with the intensive solar irradiation», *Applied Thermal Engineering*, vol. 232, p. 121077, set. 2023, doi: 10.1016/j.applthermaleng.2023.121077.

[12] A. Lingayat, R. Balijepalli, e V. P. Chandramohan, «Applications of solar energy based drying technologies in various industries – A review», *Solar Energy*, vol. 229, pp. 52–68, nov. 2021, doi: 10.1016/j.solener.2021.05.058.

[13] S. K. Verma, N. K. Gupta, e D. Rakshit, «A comprehensive analysis on advances in application of solar collectors considering design, process and working fluid parameters for solar to thermal conversion», *Solar Energy*, vol. 208, pp. 1114–1150, set. 2020, doi: 10.1016/j.solener.2020.08.042.

[14] S. C. Bhatia, A c. di, *Advanced Renewable Energy Systems, (Part 1 and 2)*, 0 ed. WPI Publishing, 2014. doi: 10.1201/b18242.

[15] R. Eismann, «Accurate analytical modeling of flat plate solar collectors: Extended correlation for convective heat loss across the air gap between absorber and cover plate», *Solar Energy*, vol. 122, pp. 1214–1224, dic. 2015, doi: 10.1016/j.solener.2015.10.037.

[16] H. Herwig, «What Exactly is the Nusselt Number in Convective Heat Transfer Problems and are There Alternatives?», *Entropy*, vol. 18, fasc. 5, p. 198, mag. 2016, doi: 10.3390/e18050198.

[17] C. B. Eaton e H. A. Blum, «The use of moderate vacuum environments as a means of increasing the collection efficiencies and operating temperatures of flat-plate solar collectors», *Solar Energy*, vol. 17, fasc. 3, pp. 151–158, lug. 1975, doi: 10.1016/0038-092X(75)90053-5.

[18] «99/03262 High efficiency evacuated flat-plate solar collector for process steam production», *Fuel and Energy Abstracts*, vol. 40, fasc. 5, p. 342, set. 1999, doi: 10.1016/S0140-6701(99)91217-1.

[19] R. W. Moss, P. Henshall, F. Arya, G. S. F. Shire, T. Hyde, e P. C. Eames, «Performance and operational effectiveness of evacuated flat plate solar collectors compared with conventional thermal, PVT and PV panels», *Applied Energy*, vol. 216, pp. 588–601, apr. 2018, doi: 10.1016/j.apenergy.2018.01.001.

[20] C. Benvenuti, «The SRB solar thermal panel», *Europhysics News*, vol. 44, fasc. 3, pp. 16–18, mag. 2013, doi: 10.1051/epn/2013301.

[21] «TVP Solar, MT-30 datasheet <http://www.tvpsolar.com/files/pagine/1464011780_MTPower%20Datasheet%20(v4.2x)(ver5).pdf> ».
[22] D. Gao *et al.*, «Experimental and numerical analysis of an efficiently optimized evacuated flat plate solar collector under medium temperature», *Applied Energy*, vol. 269, p. 115129, lug. 2020, doi: 10.1016/j.apenergy.2020.115129.
[23] «Alanod, 'Alanod Surfaces - Mirotherm', www.alanod.com, 2021. https://alanod.com/en/products/our-surfaces (accessed Jan. 02, 2023).»
[24] W. Dai, S. Pupeschi, D. Hanaor, e Y. Gan, «Influence of gas pressure on the effective thermal conductivity of ceramic breeder pebble beds», *Fusion Engineering and Design*, vol. 118, pp. 45–51, mag. 2017, doi: 10.1016/j.fusengdes.2017.03.073.
[25] N. Benz e T. Beikircher, «HIGH EFFICIENCY EVACUATED FLAT-PLATE SOLAR COLLECTOR FOR PROCESS STEAM PRODUCTION1Paper presented at the ISES Solar World Congress, Taejon, South Korea, 24–29 August 1997.1», *Solar Energy*, vol. 65, fasc. 2, pp. 111–118, feb. 1999, doi: 10.1016/S0038-092X(98)00122-4.
[26] T. Sokhansefat, A. Kasaeian, K. Rahmani, A. H. Heidari, F. Aghakhani, e O. Mahian, «Thermoeconomic and environmental analysis of solar flat plate and evacuated tube collectors in cold climatic conditions», *Renewable Energy*, vol. 115, pp. 501–508, gen. 2018, doi: 10.1016/j.renene.2017.08.057.
[27] V. G. Belessiotis e E. Papanicolaou, «History of Solar Energy», in *Comprehensive Renewable Energy*, Elsevier, 2012, pp. 85–102. doi: 10.1016/B978-0-08-087872-0.00303-6.
[28] B. A. A. Yousef, A. Radwan, A. G. Olabi, e M. A. Abdelkareem, «Development of solar thermal energy systems», in *Renewable Energy - Volume 1 : Solar, Wind, and Hydropower*, Elsevier, 2023, pp. 23–43. doi: 10.1016/B978-0-323-99568-9.00022-4.
[29] K. Hudon, «Solar Energy – Water Heating», in *Future Energy*, Elsevier, 2014, pp. 433–451. doi: 10.1016/B978-0-08-099424-6.00020-X.
[30] I. Sarbu e C. Sebarchievici, «Solar Collectors», in *Solar Heating and Cooling Systems*, Elsevier, 2017, pp. 29–97. doi: 10.1016/B978-0-12-811662-3.00003-7.
[31] H. N. S. Al-Joboory, «Comparative experimental investigation of two evacuated tube solar water heaters of different configurations for domestic application of Baghdad- Iraq», *Energy and Buildings*, vol. 203, p. 109437, nov. 2019, doi: 10.1016/j.enbuild.2019.109437.
[32] S. M. Tabarhoseini, M. Sheikholeslami, e Z. Said, «Recent advances on the evacuated tube solar collector scrutinizing latest innovations in thermal performance improvement involving economic and environmental analysis», *Solar Energy Materials and Solar Cells*, vol. 241, p. 111733, lug. 2022, doi: 10.1016/j.solmat.2022.111733.
[33] *ISO 9806:2017. Solar energy – Solar thermal collectors – Test methods International Organization for Standardization. Geneva, Switzerland.*
[34] R. W. Moss, P. Henshall, F. Arya, G. S. F. Shire, P. C. Eames, e T. Hyde, «Simulator testing of evacuated flat plate solar collectors for industrial heat and building integration», *Solar Energy*, vol. 164, pp. 109–118, apr. 2018, doi: 10.1016/j.solener.2018.02.004.
[35] «V. Palmieri, 'Vacuum Solar Thermal Panel', USOO81 6 1965B2, 2012»
[36] D. De Maio *et al.*, «A Selective Solar Absorber for Unconcentrated Solar Thermal Panels», *Energies*, vol. 14, fasc. 4, p. 900, feb. 2021, doi: 10.3390/en14040900.
[37] A. M. Shariah, A. Rousan, Kh. K. Rousan, e A. A. Ahmad, «Effect of thermal conductivity of absorber plate on the performance of a solar water heater», *Applied Thermal Engineering*, vol. 19, fasc. 7, pp. 733–741, lug. 1999, doi: 10.1016/S1359-4311(98)00086-6.
[38] S. A. Sakhaei e M. S. Valipour, «Performance enhancement analysis of The flat plate collectors: A comprehensive review», *Renewable and Sustainable Energy Reviews*, vol. 102, pp. 186–204, mar. 2019, doi: 10.1016/j.rser.2018.11.014.
[39] R. Abdallah *et al.*, «Estimation of solar irradiation and optimum tilt angles for south-facing surfaces in the United Arab Emirates: a case study using PVGIS and PVWatts», in *Recent Advances in Renewable Energy Technologies*, Elsevier, 2022, pp. 3–39. doi: 10.1016/B978-0-12-823532-4.00004-5.

[40] L. Wang e J. Yu, «Principles of photocatalysis», in *Interface Science and Technology*, vol. 35, Elsevier, 2023, pp. 1–52. doi: 10.1016/B978-0-443-18786-5.00002-0.
[41] F. Cao, K. McEnaney, G. Chen, e Z. Ren, «A review of cermet-based spectrally selective solar absorbers», *Energy Environ. Sci.*, vol. 7, fasc. 5, p. 1615, 2014, doi: 10.1039/c3ee43825b.
[42] N. P. Sergeant, O. Pincon, M. Agrawal, e P. Peumans, «Design of wide-angle solar-selective absorbers using aperiodic metal-dielectric stacks», *Opt. Express*, vol. 17, fasc. 25, p. 22800, dic. 2009, doi: 10.1364/OE.17.022800.
[43] A. B. Khelifa *et al.*, «Growth and characterization of spectrally selective Cr2O3/Cr/Cr2O3 multilayered solar absorber by e-beam evaporation», *Journal of Alloys and Compounds*, vol. 734, pp. 204–209, feb. 2018, doi: 10.1016/j.jallcom.2017.11.036.
[44] A. B. Khelifa *et al.*, «Optical simulation, characterization and thermal stability of Cr2O3/Cr/Cr2O3multilayer solar selective absorber coatings», *Journal of Alloys and Compounds*, vol. 783, pp. 533–544, apr. 2019, doi: 10.1016/j.jallcom.2018.12.286.
[45] M. A. Rosen, «Energy efficiency and sustainable development», *IEEE Technol. Soc. Mag.*, vol. 15, fasc. 4, pp. 21–26, 1996, doi: 10.1109/44.546454.
[46] D. E. Prapas, B. Norton, e S. D. Probert, «Optics of parabolic-trough, solar-energy collectors, possessing small concentration ratios», *Solar Energy*, vol. 39, fasc. 6, pp. 541–550, 1987, doi: 10.1016/0038-092X(87)90061-2.
[47] C. C. Smith e T. A. Weiss, «Design application of the Hottel-Whillier-Bliss equation», *Solar Energy*, vol. 19, fasc. 2, pp. 109–113, 1977, doi: 10.1016/0038-092X(77)90047-0.
[48] S. A. Kalogirou, «Solar thermal collectors and applications», *Progress in Energy and Combustion Science*, vol. 30, fasc. 3, pp. 231–295, 2004, doi: 10.1016/j.pecs.2004.02.001.
[49] W. J. Platzer, D. Mills, e W. Gardner, «Linear Fresnel Collector (LFC) solar thermal technology», in *Concentrating Solar Power Technology*, Elsevier, 2021, pp. 165–217. doi: 10.1016/B978-0-12-819970-1.00006-2.
[50] S. Hess e V. I. Hanby, «Collector Simulation Model with Dynamic Incidence Angle Modifier for Anisotropic Diffuse Irradiance», *Energy Procedia*, vol. 48, pp. 87–96, 2014, doi: 10.1016/j.egypro.2014.02.011.
[51] W. R. McIntire, «Factored approximations for biaxial incident angle modifiers», *Solar Energy*, vol. 29, fasc. 4, pp. 315–322, 1982, doi: 10.1016/0038-092X(82)90246-8.
[52] «Database https://solarkeymark.eu/database/ (accessed Oct 31, 2023).»
[53] S. Fortuin, G. Stryi-Hipp, W. Kramer, e K. Kramer, «Solar Collectors, Non-concentrating», in *Encyclopedia of Sustainability Science and Technology*, R. A. Meyers, A c. di, New York, NY: Springer New York, 2020, pp. 1–21. doi: 10.1007/978-1-4939-2493-6_681-3.
[54] «ALMECO GROUP - Alluminio - ALMECO GROUP, (n.d.). https://www.almecogroup.com/it.»
[55] *Handbook of Physical Vapor Deposition (PVD) Processing*. Elsevier, 2010. doi: 10.1016/C2009-0-18800-1.
[56] D. R. Baer e S. Thevuthasan, «Characterization of Thin Films and Coatings», in *Handbook of Deposition Technologies for Films and Coatings*, Elsevier, 2010, pp. 749–864. doi: 10.1016/B978-0-8155-2031-3.00016-8.
[57] «TVP Solar, (2023). https://www.tvpsolar.com/.»
[58] «ISASI – SciencesApp | Eduardo Caianiello, (n.d.). https://www.isasi.cnr.it/.»
[59] H. Adachi e K. Wasa, «Thin Films and Nanomaterials», in *Handbook of Sputtering Technology*, Elsevier, 2012, pp. 3–39. doi: 10.1016/B978-1-4377-3483-6.00001-2.
[60] A. Bashir, T. I. Awan, A. Tehseen, M. B. Tahir, e M. Ijaz, «Interfaces and surfaces», in *Chemistry of Nanomaterials*, Elsevier, 2020, pp. 51–87. doi: 10.1016/B978-0-12-818908-5.00003-2.
[61] C. D'Alessandro *et al.*, «Calorimetric testing of solar thermal absorbers for high vacuum flat panels», *Solar Energy*, vol. 243, pp. 81–90, set. 2022, doi: 10.1016/j.solener.2022.07.039.
[62] C. D'Alessandro *et al.*, «Low cost high intensity LED illumination device for high uniformity solar testing», *Solar Energy*, vol. 221, pp. 140–147, giu. 2021, doi: 10.1016/j.solener.2021.04.017.
[63] C. D. Alessandro *et al.*, «Measurements of Spectrally Averaged Absorptivity and Emissivity for a Selective Solar Absorber in High Vacuum Under Direct Solar Illumination», *J. Phys.: Conf. Ser.*, vol. 1599, fasc. 1, p. 012027, ago. 2020, doi: 10.1088/1742-6596/1599/1/012027.

[64] R. Russo, M. Monti, F. Di Giamberardino, e V. G. Palmieri, «Characterization of selective solar absorber under high vacuum», *Opt. Express*, vol. 26, fasc. 10, p. A480, mag. 2018, doi: 10.1364/OE.26.00A480.

[65] R. Russo *et al.*, «The Absorptance of Selective Solar Absorber Working in High Vacuum», in *20th Italian National Conference on Photonic Technologies (Fotonica 2018)*, Lecce, Italy: Institution of Engineering and Technology, 2018, p. 56 (4 pp.)-56 (4 pp.). doi: 10.1049/cp.2018.1665.

[66] D. De Maio *et al.*, «Thermal Efficiency of a Concentrating Solar Collector Under High-Vacuum», *J. Phys.: Conf. Ser.*, vol. 1599, fasc. 1, p. 012029, ago. 2020, doi: 10.1088/1742-6596/1599/1/012029.

[67] «Spectroscopic Ellipsometry - HORIBA, (n.d.). https://www.horiba.com/en_en/products/scientific/surface-characterization/spectroscopic-ellipsometry/.»

[68] D.-H. Lee e N.-G. Cho, «Assessment of surface profile data acquired by a stylus profilometer», *Meas. Sci. Technol.*, vol. 23, fasc. 10, p. 105601, ott. 2012, doi: 10.1088/0957-0233/23/10/105601.

[69] «Alanod». [Online]. Disponibile su: https://alanod.com/

[70] R. Russo, M. Monti, F. di Giamberardino, e V. G. Palmieri, «Characterization of selective solar absorber under high vacuum», *Optics Express*, vol. 26, fasc. 10, p. A480, mag. 2018, doi: 10.1364/OE.26.00A480.

[71] R. Russo *et al.*, «The Absorptance of Selective Solar Absorber Working in High Vacuum», in *20th Italian National Conference on Photonic Technologies (Fotonica 2018)*, Institution of Engineering and Technology, 2018, p. 56 (4 pp.)-56 (4 pp.). doi: 10.1049/cp.2018.1665.

[72] X.-F. Li *et al.*, «High solar absorption of a multilayered thin film structure», *Opt. Express*, vol. 15, fasc. 4, p. 1907, feb. 2007, doi: 10.1364/OE.15.001907.

[73] P. Bermel, J. Lee, J. D. Joannopoulos, I. Celanovic, e M. Soljacie, «SELECTIVE SOLAR ABSORBERS», *Annual Review of Heat Transfer*, vol. 15, fasc. 15, pp. 231–254, 2012, doi: 10.1615/AnnualRevHeatTransfer.2012004119.

[74] J. M. Bennett e E. J. Ashley, «Infrared Reflectance and Emittance of Silver and Gold Evaporated in Ultrahigh Vacuum», *Appl. Opt.*, vol. 4, fasc. 2, p. 221, feb. 1965, doi: 10.1364/AO.4.000221.

[75] P. Sahoo, S. K. Das, e J. Paulo Davim, «3.3 Surface Finish Coatings», in *Comprehensive Materials Finishing*, Elsevier, 2017, pp. 38–55. doi: 10.1016/B978-0-12-803581-8.09167-0.

[76] J.-K. Sim, S.-K. Lee, J.-S. Kim, K.-U. Jeong, H.-K. Ahn, e C.-R. Lee, «Efficiency enhancement of CIGS compound solar cell fabricated using homomorphic thin Cr2O3 diffusion barrier formed on stainless steel substrate», *Applied Surface Science*, vol. 389, pp. 645–650, dic. 2016, doi: 10.1016/j.apsusc.2016.06.194.

[77] R. Keçili, S. Büyüktiryaki, e C. M. Hussain, «Engineered Nanosensors Based on Molecular Imprinting Technology», in *Handbook of Nanomaterials for Industrial Applications*, Elsevier, 2018, pp. 1031–1046. doi: 10.1016/B978-0-12-813351-4.00059-6.

[78] F. Cverna e ASM International, A c. di, *ASM ready reference. Thermal properties of metals*. in ASM materials data series. Materials Park, Ohio: ASM International, 2002.

[79] D. De Maio *et al.*, «Multilayers for efficient thermal energy conversion in high vacuum flat solar thermal panels», *Thin Solid Films*, vol. 735, p. 138869, ott. 2021, doi: 10.1016/j.tsf.2021.138869.

[80] A. R. Forouhi e I. Bloomer, «Optical dispersion relations for amorphous semiconductors and amorphous dielectrics», *Phys. Rev. B*, vol. 34, fasc. 10, pp. 7018–7026, nov. 1986, doi: 10.1103/PhysRevB.34.7018.

[81] A. R. Forouhi e I. Bloomer, «Optical properties of crystalline semiconductors and dielectrics», *Phys. Rev. B*, vol. 38, fasc. 3, pp. 1865–1874, lug. 1988, doi: 10.1103/PhysRevB.38.1865.

[82] D. Barchiesi e T. Grosges, «Fitting the optical constants of gold, silver, chromium, titanium, and aluminum in the visible bandwidth», *J. Nanophoton*, vol. 8, fasc. 1, p. 083097, gen. 2014, doi: 10.1117/1.JNP.8.083097.

[83] A. D. Rakić, A. B. Djurišić, J. M. Elazar, e M. L. Majewski, «Optical properties of metallic films for vertical-cavity optoelectronic devices», *Appl. Opt.*, vol. 37, fasc. 22, p. 5271, ago. 1998, doi: 10.1364/AO.37.005271.

[84] H. C. Barshilia, N. Selvakumar, K. S. Rajam, e A. Biswas, «Structure and optical properties of pulsed sputter deposited CrxOy/Cr/Cr2O3 solar selective coatings», *Journal of Applied Physics*, vol. 103, fasc. 2, p. 023507, gen. 2008, doi: 10.1063/1.2831364.

[85] M. F. Al-Kuhaili e S. M. A. Durrani, «Optical properties of chromium oxide thin films deposited by electron-beam evaporation», *Optical Materials*, vol. 29, fasc. 6, pp. 709–713, feb. 2007, doi: 10.1016/j.optmat.2005.11.020.

[86] R. Boidin, T. Halenkovič, V. Nazabal, L. Beneš, e P. Němec, «Pulsed laser deposited alumina thin films», *Ceramics International*, vol. 42, fasc. 1, pp. 1177–1182, gen. 2016, doi: 10.1016/j.ceramint.2015.09.048.

[87] M. A. Muriel e A. Carballar, «Internal field distributions in fiber Bragg gratings», *IEEE Photon. Technol. Lett.*, vol. 9, fasc. 7, pp. 955–957, lug. 1997, doi: 10.1109/68.593364.

[88] C.-D. Wen e I. Mudawar, «Modeling the effects of surface roughness on the emissivity of aluminum alloys», *International Journal of Heat and Mass Transfer*, vol. 49, fasc. 23–24, pp. 4279–4289, nov. 2006, doi: 10.1016/j.ijheatmasstransfer.2006.04.037.

[89] S.-T. Mi, Y.-C. Zhang, X.-B. Fu, Q. Li, e T. Kong, «Study on infrared emissivity model based on perturbation method and Kirchhoff approximation and its application in aluminum alloy welding», *Optik*, vol. 290, p. 171347, ott. 2023, doi: 10.1016/j.ijleo.2023.171347.

[90] W. J. Zhang, J. Qiu, e L. H. Liu, «Deviation characteristics of specular reflectivity of micro-rough surface from Fresnel's equation», *Journal of Quantitative Spectroscopy and Radiative Transfer*, vol. 160, pp. 50–62, lug. 2015, doi: 10.1016/j.jqsrt.2015.03.023.

[91] J. Xu, J. Wang, L. Lu, e M. Gao, «Study on the infrared emissivity of nonstoichiometric titanium chromium nitride films», *Thin Solid Films*, vol. 754, p. 139303, lug. 2022, doi: 10.1016/j.tsf.2022.139303.

[92] K. Xu *et al.*, «Thermal emittance of Ag films deposited by magnetron sputtering», *Vacuum*, vol. 174, p. 109200, apr. 2020, doi: 10.1016/j.vacuum.2020.109200.

[93] K. Zhang, Y. Zhao, K. Yu, e Y. Liu, «Development of experimental apparatus for precise emissivity determination based on the improved method compensating disturbances by background radiation», *Infrared Physics & Technology*, vol. 92, pp. 350–357, ago. 2018, doi: 10.1016/j.infrared.2018.06.031.

[94] K. Yu, G. Wang, L. Li, K. Zhang, e Y. Liu, «A new experimental apparatus for polarized spectral emissivity measurement in a controlled environment», *Infrared Physics & Technology*, vol. 111, p. 103572, dic. 2020, doi: 10.1016/j.infrared.2020.103572.

[95] K. Zhang, Y. Xu, X. Wu, K. Yu, e Y. Liu, «A new approach for accurately measuring the spectral emissivity via modulating the surrounding radiation», *Journal of Quantitative Spectroscopy and Radiative Transfer*, vol. 288, p. 108277, set. 2022, doi: 10.1016/j.jqsrt.2022.108277.

[96] P. A. Van Nijnatten *et al.*, «Uncertainties in the determination of thermal emissivity by measurement of reflectance using Fourier transform spectrometers», *Thin Solid Films*, vol. 502, fasc. 1–2, pp. 164–169, apr. 2006, doi: 10.1016/j.tsf.2005.07.262.

[97] S. X. Cheng, «Total hemispherical emissivities of cobalt and nickel in the range 350–1000 K», *Experimental Thermal and Fluid Science*, vol. 2, fasc. 2, pp. 165–172, apr. 1989, doi: 10.1016/0894-1777(89)90030-7.

[98] P. Ablewski, M. Bober, e M. Zawada, «Emissivities of vacuum compatible materials: towards minimising blackbody radiation shift uncertainty in optical atomic clocks at room temperatures», *Metrologia*, vol. 57, fasc. 3, p. 035004, giu. 2020, doi: 10.1088/1681-7575/ab63ae.

[99] C. Monte, B. Gutschwager, S. P. Morozova, e J. Hollandt, «Radiation Thermometry and Emissivity Measurements Under Vacuum at the PTB», *Int J Thermophys*, vol. 30, fasc. 1, pp. 203–219, feb. 2009, doi: 10.1007/s10765-008-0442-9.

[100] L. Granados, S. Huang, D. R. McKenzie, e A. W. Y. Ho-Baillie, «The importance of total hemispherical emittance in evaluating performance of building-integrated silicon and perovskite solar cells in insulated glazings», *Applied Energy*, vol. 276, p. 115490, ott. 2020, doi: 10.1016/j.apenergy.2020.115490.

[101] J. L. King, H. Jo, S. K. Loyalka, R. V. Tompson, e K. Sridharan, «Computation of total hemispherical emissivity from directional spectral models», *International Journal of Heat and Mass Transfer*, vol. 109, pp. 894–906, giu. 2017, doi: 10.1016/j.ijheatmasstransfer.2017.01.120.
[102] B. Window e G. Harding, «Thermal emissivity of copper», *J. Opt. Soc. Am.*, vol. 71, fasc. 3, p. 354, mar. 1981, doi: 10.1364/JOSA.71.000354.
[103] D. De Luca, D. Kortge, E. Di Gennaro, R. Russo, e P. Bermel, «Ultra-thin sputter-deposited infrared rugate mirror for enhancing solar-to-thermal energy conversion», *Opt. Lett.*, vol. 47, fasc. 2, p. 230, gen. 2022, doi: 10.1364/OL.442839.
[104] D. De Maio, C. D'Alessandro, A. Caldarelli, M. Musto, e R. Russo, «Solar selective coatings for evacuated flat plate collectors: Optimisation and efficiency robustness analysis», *Solar Energy Materials and Solar Cells*, vol. 242, p. 111749, ago. 2022, doi: 10.1016/j.solmat.2022.111749.
[105] E. Gaudino, A. Caldarelli, R. Russo, e M. Musto, «Formulation of an Efficiency Model Valid for High Vacuum Flat Plate Collectors», *Energies*, vol. 16, fasc. 22. 2023. doi: 10.3390/en16227650.
[106] A. Olivares, J. Rekstad, M. Meir, S. Kahlen, e G. Wallner, «Degradation model for an extruded polymeric solar thermal absorber», *Solar Energy Materials and Solar Cells*, vol. 94, fasc. 6, pp. 1031–1037, giu. 2010, doi: 10.1016/j.solmat.2010.02.001.
[107] S. Karatasou, M. Santamouris, e V. Geros, «On the calculation of solar utilizability for south oriented flat plate collectors tilted to an angle equal to the local latitude», *Solar Energy*, vol. 80, fasc. 12, pp. 1600–1610, dic. 2006, doi: 10.1016/j.solener.2005.12.003.
[108] B. A. A. Yousef, A. Radwan, A. G. Olabi, e M. A. Abdelkareem, «Sun composition, solar angles, and estimation of solar radiation», in *Renewable Energy - Volume 1 : Solar, Wind, and Hydropower*, Elsevier, 2023, pp. 3–22. doi: 10.1016/B978-0-323-99568-9.00023-6.
[109] «Simulink MathWorks, Inc. (1194-2022).» Consultato: 9 gennaio 2022. [Online]. Disponibile su: https://ch.mathworks.com/products/simulink.html
[110] «https://www.therminol.com/product/71093438?pn=Therminol-66-Heat-Transfer-Fluid».
[111] «NREL SOLPOS TOOL». Consultato: 10 gennaio 2024. [Online]. Disponibile su: https://midcdmz.nrel.gov/solpos/solpos.html
[112] B. Carlsson, K. Möller, M. Köhl, U. Frei, e S. Brunold, «Qualification test procedure for solar absorber surface durability», *Solar Energy Materials and Solar Cells*, vol. 61, fasc. 3, pp. 255–275, mar. 2000, doi: 10.1016/S0927-0248(99)00111-7.
[113] A. Caldarelli *et al.*, «Characterization and thermal aging tests of Cr based multilayer for unconcentrated solar thermal applications», *Thin Solid Films*, vol. 735, p. 138870, ott. 2021, doi: 10.1016/j.tsf.2021.138870.
[114] M. Köhl, M. Heck, S. Brunold, U. Frei, B. Carlsson, e K. Möller, «Advanced procedure for the assessment of the lifetime of solar absorber coatings», *Solar Energy Materials and Solar Cells*, vol. 84, fasc. 1–4, pp. 275–289, ott. 2004, doi: 10.1016/j.solmat.2004.01.041.
[115] E. Gaudino, M. Musto, A. Caldarelli, D. D. Luca, E. D. Gennaro, e R. Russo, «Evaluation of the absorber temperature frequency function valid for evacuated flat plate collectors», *Energy Reports*, vol. 8, pp. 1071–1080, 2022, doi: https://doi.org/10.1016/j.egyr.2022.05.275.
[116] «Solar radiation tool of the Joint Research Centre (JRC), (n.d.). https://re.jrc.ec.europa.eu/pvg_tools/it/#MR.»
[117] «XCELTHERM 500 https://www.radcoind.com/fluid/xceltherm-500/».
[118] S. Sánchez-Carbajal e P. M. Rodrigo, «Optimum Array Spacing in Grid-Connected Photovoltaic Systems considering Technical and Economic Factors», *International Journal of Photoenergy*, vol. 2019, pp. 1–14, gen. 2019, doi: 10.1155/2019/1486749.
[119] A. Duret, X. Jobard, G. Demonchy, e S. Pauletta, «Performance Monitoring of an 800m2 Solar Thermal Plant with Evacuated Flat Plate Collectors Coupled to a DHN», *Eurosun 2022 Proceedings*, 2022.